NTNU

Norwegian University of
Science and Technology

Upscaling, analysis, and design of a floating vertical axis wind turbine

Oppskalering, analyse, og design av en
flytende vindturbin med vertikal aksle

Gaspar Gohin

Marine Technology
Submission date: June 2018
Supervisor: Erin Bachynski, IMT

Norwegian University of Science and Technology
Department of Marine Technology

MASTER THESIS
IN MARINE TECHNOLOGY

Upscaling, Analysis, and Design of a Floating Vertical Axis Wind Turbine

Spring 2018 - Gaspar Gohin

Supervisor: Erin Bachynski (NTNU)
Co-supervisor: Chittiappa Muthanna (SINTEF Ocean)

Department of Marine Technology (IMT)

NTNU SINTEF

Project Outline

Background

Although less developed than their counterparts with a horizontal axis, vertical axis wind turbines (VAWTs) present some potential advantages for the floating offshore wind industry: they have a lower center of gravity and fewer components. The conceptual 5 MW Deepwind spar-type floating VAWT has been studied extensively, but further development of the concept has not been pursued. The present master's thesis aims to develop an upscaled 10 MW version of the Deepwind concept, and to study its behavior in wind and waves. In order to carry out aero-hydro-servo-elastic simulations with the floating VAWT, the SIMA software will be used, but further developments may be needed.

Assignment

The following tasks should be addressed in the thesis work:

1. Literature review regarding vertical axis floating offshore wind turbines, upscaling of VAWT, Deepwind turbine, optimization.
2. Preliminary upscaling of the platform in order to support the 10 MW VAWT, also considering stability and natural frequencies.
3. Model and carry out preliminary analyses of the 5MW (for verification against published results) and 10 MW VAWT. If needed, improvements to the software may be pursued.
4. Carry out a design optimization of the hull form for the 10 MW floater, and analyse the performance of the resulting design in wind and wave conditions.
5. Report and conclude on the investigation.

The work scope could be larger than anticipated. Subject to approval from the supervisor, topics may be deleted from the list above or reduced in extent.

In the project, the candidate shall present his personal contribution to the resolution of problem within the scope of the project work.

Theories and conclusions should be based on mathematical derivations and/or logic reasoning identifying the various steps in the deduction.

The candidate should utilize the existing possibilities for obtaining relevant literature.

The project report should be organized in a rational manner to give a clear exposition of results, assessments, and conclusions. The text should be brief and to the point, with a clear language. Telegraphic language should be avoided.

The project report shall contain the following elements: A text defining the scope, preface, list of contents, main body of the project report, conclusions with recommendations for further work, list of symbols and acronyms, reference and (optional) appendices. All figures, tables and equations shall be numerated.

The supervisor may require that the candidate, in an early stage of the work, present a written plan for the completion of the work. The plan should include a budget for the use of computer and laboratory resources that will be charged to the department. Overruns shall be reported to the supervisor.

The original contribution of the candidate and material taken from other sources shall be clearly defined. Work from other sources shall be properly referenced using an acknowledged referencing system.

The project report shall be submitted in two copies: - Signed by the candidate
- The text defining the scope included
- In bound volume(s)
- Drawings and/or computer prints which cannot be bound should be organized in a separate folder.

Deadline: 04.06.2018

Supervisor: Erin Bachynski

Student: Gaspar Gohin

Abstract

There are currently two main trends governing research and development in the offshore wind industry. The first one is upscaling, i.e. manufacturing larger and more powerful wind turbines; the second one is platform innovation, with floating wind turbines giving access to intermediate and deep water depths. Most of these efforts are focused on horizontal axis wind turbines (HAWT), and the first floating wind farm was commissioned in 2017 using spar-floating HAWTs (Hywind Scotland). Meanwhile, vertical axis wind turbines (VAWT) might be good candidates for upscaling and deep water deployment, as they have a potential for cost reduction due to their lower center of gravity and reduced machinery (no blade pitch system, and no yaw rotor positioning system).

The DeepWind project developed a spar-floating 5 MW VAWT concept, with focus on spar optimization. A control strategy has also been developed for VAWTs, using the generator torque as a control input. However, some difficulties have been faced in the INNWIND project when attempting to upscale the DeepWind VAWT from 5 to 10 MW. Also some numerical integrated analysis of VAWTs have been conducted successfully, combining various fields of research: aerodynamics, hydrodynamics, structural analysis, and control theory. The VAWT module currently available in the numerical analysis tool SIMO presents some technical issues.

In order to investigate the potential advantages of VAWTs for upscaling and spar installation, two tasks were completed: (i) numerical tool verification and improvement (SIMO) and (ii) design and analysis of 5 & 10 MW spar-floating VAWTs. The debugging of SIMO was done in FORTRAN, until a good agreement with the 5 MW DeepWind published results was reached. The design part was conducted with MATLAB for the spar optimization, and with SIMO for the control system optimization, based on a preliminary analysis of the aerodynamic power. The upscaling was made using dimensional analysis, and the resulting models were tested in wind and wave conditions using SIMO. The available models used in SIMO were the Double Multiple Streamtube (DMS) theory for the aerodynamics, Morison's equation for the hydrodynamics, a PI control law and notch filters for the control theory, and rigid bodies and linear stiffnesses for the structural part.

Overall the numerical integrated analysis of the designed models gave satisfying results. Both 5 & 10 MW VAWTs showed (i) increased power output efficiency and stability, and (ii) dynamic stability in wind and wave conditions. Additionally, the spar drafts were minimized to 50m (90m) for the 5 MW (10 MW) VAWT, giving access to intermediate water depths for VAWTs, and a stabilizing gyroscopic effect was identified in floating operating conditions. Finally the upgraded version of SIMO was uploaded, enabling further investigations on VAWTs using SIMA in the future.

Acknowledgements

This master thesis from the NTNU Department of Marine Technology (IMT) has the specificity that it was conducted as a four-month research internship at SINTEF Ocean.

Associate Professor Dr. Erin Elizabeth Bachynski was the NTNU supervisor of this thesis. I am grateful for her constant support throughout the semester, her guidance with the choice of research subject, and overall for her flexibility with the organization of the master thesis as an internship. Her dedication to offshore wind turbines research was very inspiring, both as a professor and a supervisor.

This research internship was made possible thanks to Dr. Bård Wathne Tveiten, research director at SINTEF Ocean, and to Dr. Chittiappa Muthanna, research manager and supervisor of the internship. To them I am grateful, as I really appreciated having the chance to conduct the master thesis in such a professional and stimulating environment as SINTEF Ocean.

From the SINTEF Ocean community, I am thankful to Dr. Petter Andreas Berthelsen for his experienced advice about spar optimization, to the SIMA room employees for their help with SIMO debugging, especially Pål Levold and Neil Luxcey, and to Dr. Thomas Michel Sauder for interesting exchanges about control of wind turbines.

From the NTNU community, I would like to thank PhD candidate Yuna Zhao for her precise advice with SIMA implementation and post-treatment. I am also thankful to the NTNU first to third year students for their interest and questions at the thesis presentation, and to my fifth year office mates, internationals and Norwegians, all incredible.

Finally I would like to thank my family and friends, for their support and encouragement to study marine technology and offshore wind turbines in Norway.

Nomenclature

Abbreviations

AC	Actuator Cylinder
BEM	Blade Element Momentum
CG	Center of Gravity
CoE	Cost of Energy
DA	Dynamic Analysis
DMS	Double Multiple Streamtube
DOF	Degree of Freedom
FHAWT	Floating Horizontal Axis Wind Turbine
FVAWT	Floating Vertical Axis Wind Turbine
HAWT	Horizontal Axis Wind Turbine
O&M	Operations and Maintenance
PI	Proportional Integral
PID	Proportional Integral Derivative
STD	Standard Deviation
TSR	Tip Speed Ratio
VAWT	Vertical Axis Wind Turbine

List of Symbols

α	Angle of attack
$\bar{X}$	Mean value of the physical variable X
λ	Tip speed ratio

$\mathcal{P}$	Aerodynamic power
$\mathcal{P}_e$	Electrical power, also named generator power
ω	Rotational rotor speed
ω_f	Filtered rotor speed
ω_r	Rated rotor speed
ρ_a	Air density
ρ_{blade}	Blade linear density
ρ_w	Water density
θ, ψ	Azimutal position of the rotor
A_d	Area of a square of the damping system
A_{ii}	Added mass of the degree of freedom i
Ai	2D added mass coefficient of the spar element i
B_{ii}	Damping coefficient of the degree of freedom i
BF	Ballast fraction
c	Chord of a VAWT blade
C_L	Lift coefficient
C_P	Power coefficient
C_P^*	Optimal power coefficient
$C_{D,d}$	Drag coefficient of a square plate
C_D	2D drag coefficient of a cylinder
C_{ii}	Stiffness of the degree of freedom i
Cx, i	2D quadratic damping coefficient of the spar element i
d	Draft of the spar
D_i	Diameter of the spar element i
H	Height of a VAWT blade
h_i	Height of the spar element i
I_X	Rotational inertia of the element X

K_I	Integral gain
K_P	Proportional gain
L_{blade}	Length of one blade
M_X	Mass of the element X
Q, M_z	Aerodynamic torque
Q_{notch}	Notch filter band width coefficient
R	Radius of a VAWT blade
R_d	Radius of an element of the damping system
T	Generator torque
T_i	Eigenperiod of the degree of freedom i
T_{2P}	2P period (one half of a rotor revolution)
T_{4P}	4P period (one quarter of a rotor revolution)
TSR	Tip-speed ratio
TSR^*	Optimal tip-speed ratio
U	Wind speed
U_r	Rated wind speed
V_i	Induced velocity
V_r	Relative velocity
Z_B	Center of buoyancy of the FVAWT
Z_G	Center of gravity of the FVAWT
Z_{rot}	Center of gravity of the rotor

List of Tables

List of Figures

Contents

Chapter 1: Introduction

1.1 Motivations, Objectives and Contributions

1.1.1 Motivations & Objectives

Offshore Wind Challenges: Upscaling & Deep Water

The offshore wind industry is moving towards deeper waters, as the fist floating wind park was commissioned in 2017 (Hywind, [1]). Moreover, the mean rated power capacity of each newly installed wind turbine is also increasing, reaching 5.9 MW in 2017 [2]. In this context, vertical axis wind turbines (VAWT) might be interesting alternatives to horizontal axis wind turbines (HAWT) for upscaling and deep water deployment. Indeed VAWTs have a potential for 20 % CoE (Cost of Energy) reduction due to their lower center of gravity and reduced machinery, compared to HAWTs [3]. While a 5 MW floating vertical axis wind turbine (FVAWT) concept has already been designed and studied thoroughly with the DeepWind project ([4], [5]), upscaling to 10 MW has been problematic for FVAWTs, in particular with stabilizing the power output fluctuations [6].

Simulation Challenge: VAWT Numerical Analysis in SIMO

The integrated analysis using SIMA (specifically SIMO) enables numerical investigation of the combined effects of aerodynamics, hydrodynamics, structural response and control of a VAWT. However the SIMO VAWT module has shown some odd results, which did not match with the published results ([4],[7]). While numerical analysis of VAWT was done by [7] using different coupled scripts (external Java controller, Double Multiple Streamtube (DMS) or Actuator Cylinder (AC) aerodynamic code, and SIMO-Riflex), integrated analysis of VAWT seems to be problematic with SIMO.

Objectives

This thesis had two main objectives, which tried to address the challenges mentioned above: (i) verify and improve the SIMO VAWT module, and (ii) design and test a 10 MW FVAWT in wind and wave conditions. In particular, the scope was narrowed down to spar floating VAWTs, and a preliminary literature review listed some reference models. The SIMO debugging was done until the 5 MW VAWT land-based model gave satisfying results. The design of a spar was done for the 5 & 10 MW FVAWT models, while the rotor and the control system were upscaled from 5 to 10 MW. A simplified numerical integrated analysis was led

using SIMA, and various simulations were run: decay tests, regular wave tests, constant wind tests, and wind and wave tests.

1.1.2 Main Contributions

In order to reach the objectives of the thesis, several contributions were worked upon, using various softwares:

1. SIMO VAWT aerodynamics and control module verification and debugging (FORTRAN). Moreover, some parts of the source code were tested using MATLAB.
2. Control system optimization, based on the stand-alone aerodynamic study (SIMO). The 5 MW VAWT aerodynamic dimensionless parameters were plotted (MATLAB).
3. Spar design optimization, with choice of a smaller draft than in the literature for the 5 & 10 MW FVAWTs (MATLAB).
4. Upscaling of the VAWT from 5 to 10 MW (MATLAB), using geometrical upscaling at constant tip-speed ratio (TSR).
5. Optimized designs validation (SIMO).Both 5 & 10 MW FVAWTs were tested in wind and wave conditions, as shown in Fig. 1.1.

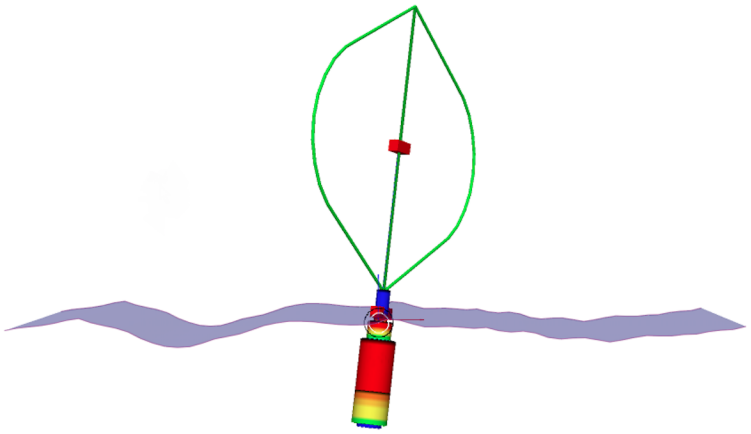

Figure 1.1: Visualization of the 5MW FVAWT modeled in SIMA

1.2 Comparative Literature Review

1.2.1 Offshore Wind Industry

Overview

Over the last ten years in Europe, the cumulative installed capacity of offshore wind installations has drastically increased by a factor 10, reaching 16 GW in 2017, as seen in Fig. 1.2 [2]. The three first European markets are the UK (6.8 GW), Germany (5.4 GW), Denmark (1.3 GW), and over 70% of the offshore wind capacity in Europe is concentrated in the North sea. The major offshore wind industry companies can be divided in two types: (i) the wind farm owners, such as Ørsted, E.ON, Innogy, and (ii) the wind turbine manufacturers, such as Siemens Gamesa, MHI Vestas, or Senvion. To understand the rapid growth of the offshore market, one can first compare the pros and cons of offshore and onshore wind turbines. At first sight, the offshore option seems more costly, as for instance the offshore foundations are three times as expensive as the onshore ones [8]. However this is compensated by a large increase in productivity, as the full charge time per year is about two times higher for offshore facilities, since the wind resource is stronger on sea than on land. Despite the fact that environmental conditions are usually harsher on sea (which can complicate installation and maintenance operations), there is more space to build wind farms offshore than onshore, with less visual and acoustic impact. Another pre-existing advantage for offshore wind is that the marine technological expertise from the oil & gas industry is often transferable, in particular when it comes to floating platforms.

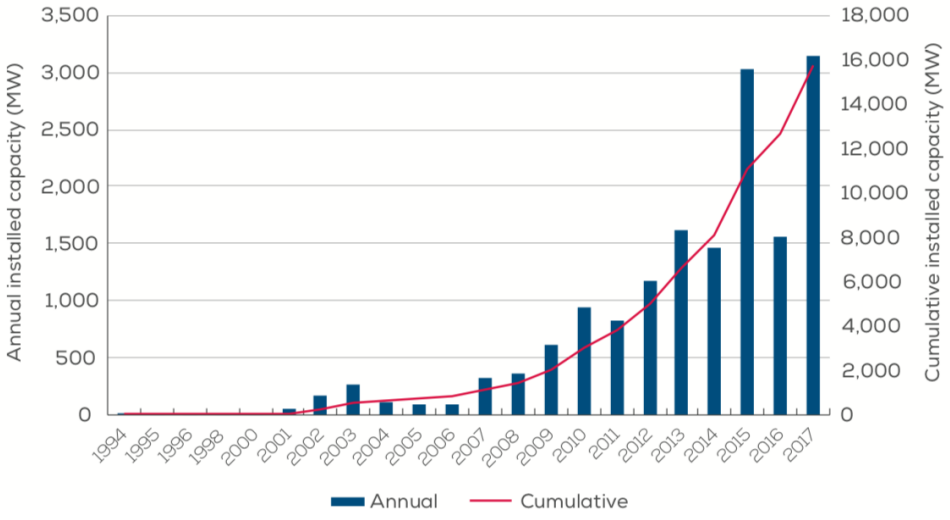

Figure 1.2: Cumulative and annual offshore wind installations (MW) [2]

Industry Examples

Generally, most existing offshore wind projects are located in shallow water areas that are relatively close to the shore, as the average water depth in 2017 was 27.5 meters and the average distance to shore was 41 km [2]. This can be connected to the fact that offshore wind turbines are most commonly mounted on bottom-fixed foundations, which imposes a 50 m depth limit on the site location [12]. Indeed, more than 80 % of today's installed offshore turbines have monopile foundations, while the rest are mostly using gravity bases and jacket foundations. These solutions seem to be the most economically advantageous so far, although the monopile technology still has a potential for cost reduction of about 10-25% [9]. In particular, costs of monopiles can be decreased by limiting the amount of steel used for the foundation, and by optimizing the site location and the structural design. Moreover, in 2017 the offshore wind industry has seen the emergence of new floating technologies, which seem promising but more expensive than bottom fixed solutions. Equinor's Hywind Scotland project was commissioned in 2017, a wind farm made of five 6 MW HAWTs mounted on floating spar buoys of 78 m draft, on a water depth larger than 100 meters. In 2018, the Floatgen demonstrator from Ideol was installed in France on a 33 meters water depth, using a floating barge prototype made of concrete. Additionally, the Windfloat project was decommissioned in 2016 after five years of operation in Portugal, and was using a semi-submersible platform as a floating foundation. Figure 1.3 depicts the various types of offshore structures that can be used to support wind turbines, with their corresponding depth ranges. In particular tension-leg-platform (TLP) wind turbines are still in research phase, mainly for economical reasons [10]. Figure 1.3 also shows that floating wind turbines tend to operate in deeper waters than bottom fixed turbines. This is confirmed by Equinor's public statement that the Hywind concept can be used until a water depth of 800 meters [1]. Generally, it seems that the offshore wind industry is moving towards deeper water [2],[11].

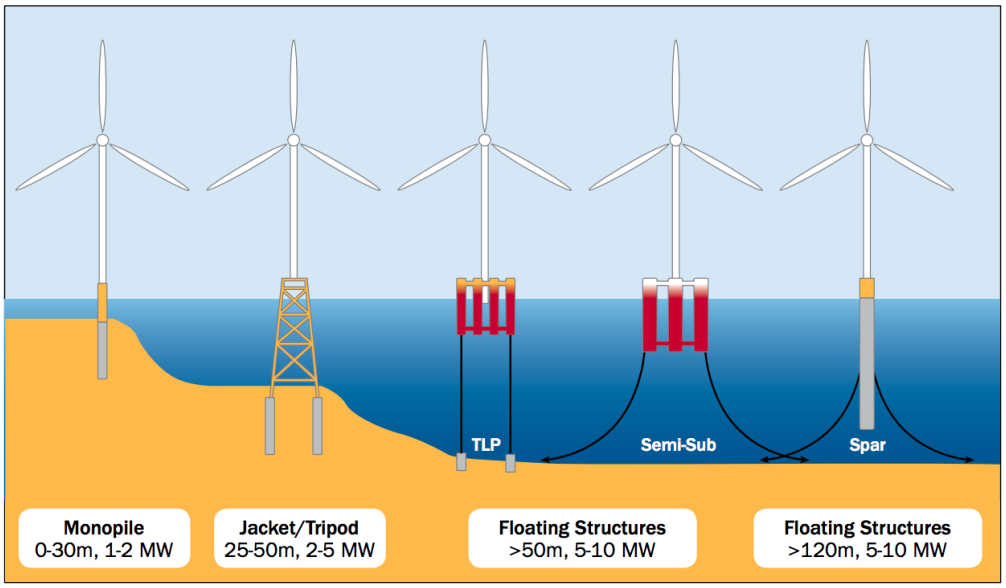

Figure 1.3: Classification of offshore wind turbines [12]

Key Trends

Another important aspect of the recent evolution of offshore wind is the size factor, as both wind turbines and wind farms tend to be larger nowadays, especially in terms of newly-built power capacity. Indeed, on the global scale the average rated capacity of new turbines has increased by 23% between 2016 and 2017, reaching 5.9 MW [2]. This trend will probably continue in the future, as Ørsted announced that it will use Siemens Gamesa's 8 MW offshore wind turbine at Borssele 1&2, a 752MW Dutch offshore wind project that should be operational in 2020. Moreover, MHI Vestas now produces the most powerful turbine in the world (9.5 MW), the V164-9.5 MW turbine which has a 164 m rotor diameter. After the success of Hywind Scotland, Equinor plans to build a 1 GW floating wind park using 10-15 MW FHAWTs, which could power a million New York homes [13]. Generally, a method called geometrical upscaling is used in the wind industry, which consists in increasing the various turbine dimensions in order to extract more wind power. These main turbine dimension parameters are essentially the rotor diameter, the hub height, and the blade chord length. In comparison, the V117-4.2 MW turbine from MHI Vestas has a smaller rotor diameter 117 m and a smaller rated power than the V164-9.5 MW model. Moreover, the increase of the turbines power capacity in the offshore wind industry is accompanied by an increase of the wind farms capacity. The average size of wind farms in construction has increased by 34% from 2016 to 2017, reaching 493 MW in 2017. The wind farm capacity growth ratio (34%) is higher than the turbine capacity growth ratio over the same period of time (23%), which means that the number of wind turbines per wind farm is also increasing (approximately equal to 83 is 2017). As a consequence, wind farms will most probably become larger in the future, as the number of turbines per farm is increasing. For instance, the Hornsea One project will start the installation phase in 2018 with 174 turbines of 7 MW each, generating a total power of more than 1.2 GW, which will make it the largest offshore wind farm so far. Moreover, there is a significant potential for deep water wind turbine deployment in Europe, as shown in Fig. 1.4 (a), and projects currently under construction already tend to be in deeper water areas and further from the coast, as depicted in Fig. 1.4 (b).

To summarize this overview of the offshore wind industry in 2018, three main distinct trends stand out from the literature, showing a probable evolution of the sector in the future:

- *Upscaling*: offshore wind turbines are becoming larger and more powerful, delivering a higher rated power capacity per turbine.
- *Large farms*: offshore wind farms are growing larger, as they tend to have a higher power capacity along with a higher number of wind turbines per farm.
- *Deep water*: floating wind turbines are now a commercial alternative to bottom-fixed wind turbines, making deep water deployment possible.

(a)

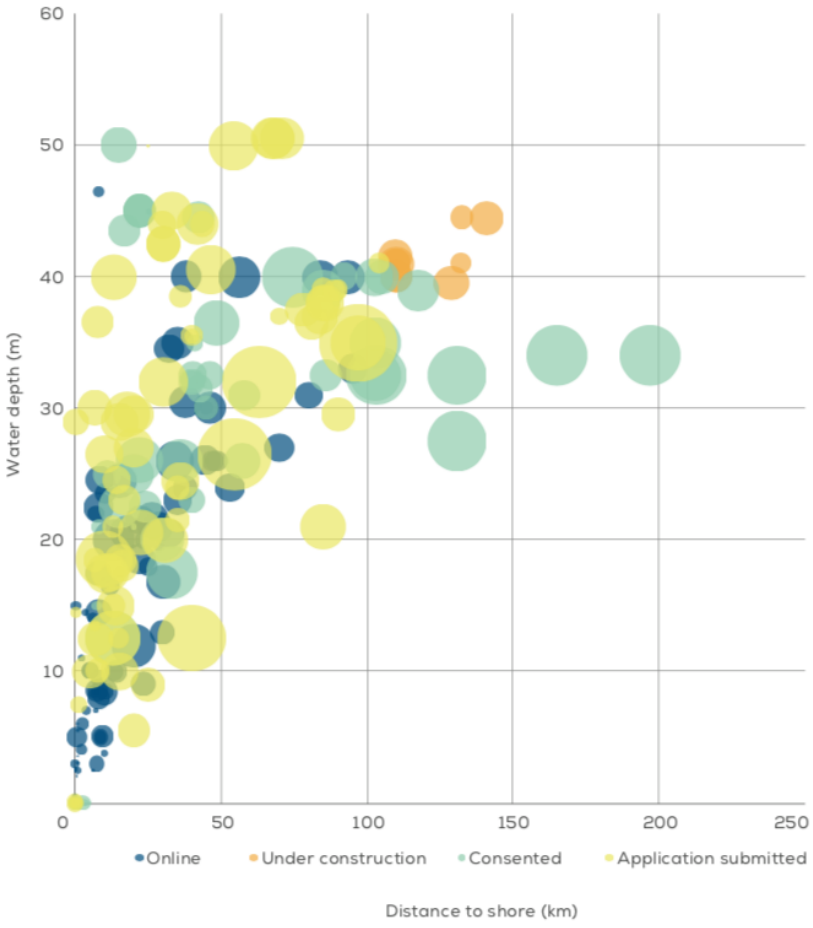

(b)

Figure 1.4: (a) Bathymetry in Europe, showing coastline and 50m depth contours [8] (b) Average water depth and distance to shore of bottom-fixed offshore wind farms, organized by development status (*blue: online, orange: under construction, green: consented, yellow: application submitted*). The size of the bubble indicates the overall capacity of the site [2].

1.2.2 Potential for Vertical Axis Wind Turbines

History

The Darrieus VAWT concept was patented in 1926 by French engineer Georges Darrieus. It generally has two curved blades, and uses lift forces to generate an aerodynamic torque around its vertical axis. Historically, VAWTs have encountered several difficulties limiting their onshore deployment at an industrial scale, mainly due to fatigue damage [14]. The FloWind Corporation installed 500 VAWTs in California in 1985, but the commercial wind farm had to be shut down in 1997 because of fatigue damage of the components. Meanwhile, HAWT wind farms were successfully developed, and the wind industry naturally preferred HAWTs to VAWTs. However new design and control techniques could limit the effect of fatigue damage on VAWTs [14].

Economy

According to [3], VAWTs have a significant potential for CoE (Cost of Energy) reduction, and global costs of offshore wind projects could be decreased by 20% using VAWTs. As shown in Fig. 1.5, VAWTs could decrease costs in the following areas: O&M (Operations and Maintenance), electrical infrastructure, logisitcs and installation, and support structure. This constitute a strategic advantage for VAWTs compared with HAWTs, in particular for deep water deployment and upscaling to 10-20 MW [3]. Moreover, upscaling and deep water installation are two innovative topics that can be combined together, as bigger turbines may require more space and larger floaters. Overall VAWTs might be good alternatives to HAWTs for large-scale offshore installation, because of the significant cost reductions in the different offshore wind project development phases.

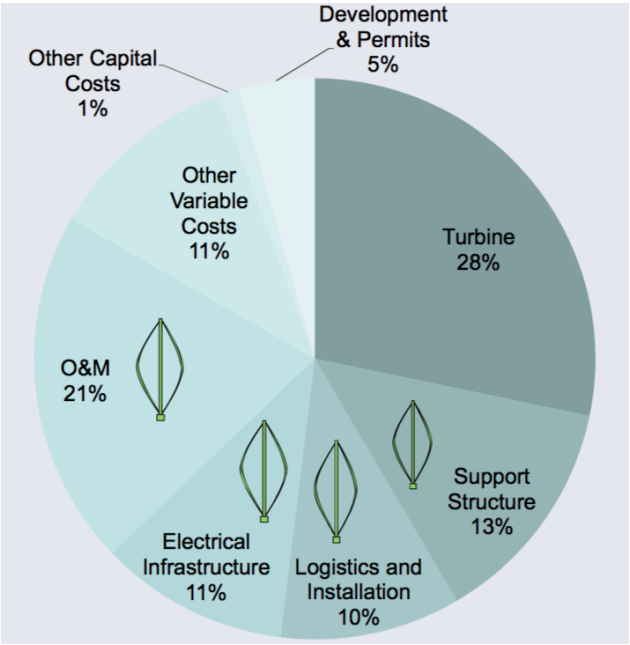

Figure 1.5: Cost analysis of an offshore wind project, with areas improved by VAWT [3]

Technology

The potential economical advantages of VAWTs can be simply explained by their technical differences with HAWTs. According to [15], having a lower drivetrain decreases both O&M and foundations costs for VAWTs. Indeed as shown in Fig. 1.6, the gearbox is more accessible for VAWTs than for HAWTs. Moreover, the same figure summarizes that VAWTs have a lower center of gravity (CG) and fewer components than HAWTs, and are insensitive to wind direction. These technical advantages of VAWTs have also been reported by [16] and [11], along with some other characteristics:

- VAWTs have a *lower center of gravity*, as their drivetrain is placed at the tower base (and not at the tower top as for HAWTs), which can decrease the platform cost.
- VAWTs have *fewer components*, as they have no yaw and blade pitch control systems. As result, VAWTs have a reduced machinery, which decreases their 0&M costs.
- VAWTs capture wind energy *independently of the wind direction*, which is why they do not require a yaw rotor positioning system.
- VAWTs seem to be more *adapted for wind farms* than HAWTs , as they are less affected by wake effects.
- VAWTs are not affected by cyclical gravity loads as HAWTs resulting in fatigue damage, which removes a structural constraint for *upscaling*.
- VAWTs are dynamically stabilized by *gyroscopic effect* when operating [17].

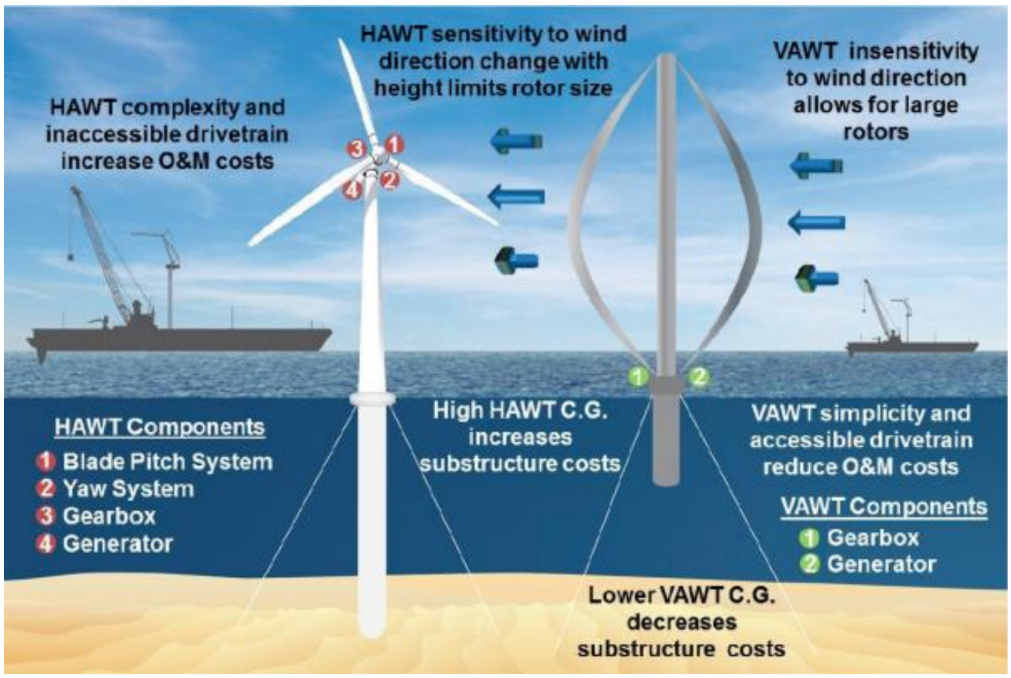

Figure 1.6: Comparison of VAWT and HAWT advantages [3]

1.2.3 Floating Wind Turbines Designs

FHAWT vs. FVAWT

While FHAWTs have been studied extensively using various types of floaters, FVAWTs constitute a relatively new research area. Two PhDs have been conducted at NTNU on this topic from an integrated dynamic analysis point of view, following the success of the DeepWind project [4]. First Wang studied a FVAWT mounted on a semi-submersible [22], then Cheng studied a FVAWT mounted on a spar [23]. Wang implemented a Double Multiple Streamtube (DMS) aerodynamic code, while Cheng implemented an Actuator Cylinder (AC) aerodynamic code. However, both PhD candidates studied the effect of harsh environmental conditions on fatigue damage, and implemented the control strategy from [19] using an external Java controller. Meanwhile, some researchers from DTU used HAWC2 to run numerical simulations using the FVAWT DeepWind concept [4].

Wang and Cheng compared the response in wind and waves of a HAWT and a VAWT mounted on the OC3 spar, after adjusting the ballast of the FVAWT [7]. They found a higher fatigue damage value at the tower bottom of the FVAWT, confirming the previous observations from the wind turbine industry. However, Cheng also found that the fatigue damage due to the fore-aft bending moment was reduced by increased the number of blades from 2 to 3 or 4 [24]. These are encouraging for FVAWTs, and show that the design of FVAWT can significantly impact the long-term structural performances. Figure 1.7 depicts the current main concepts encountered in the literature: the 5 MW NREL FHAWT, the 5 MW FVAWT DeepWind, and 6 MW Hywind for the industry. In particular, some technology transfers are possible between the HAWT and VAWT research areas, such as floating techniques.

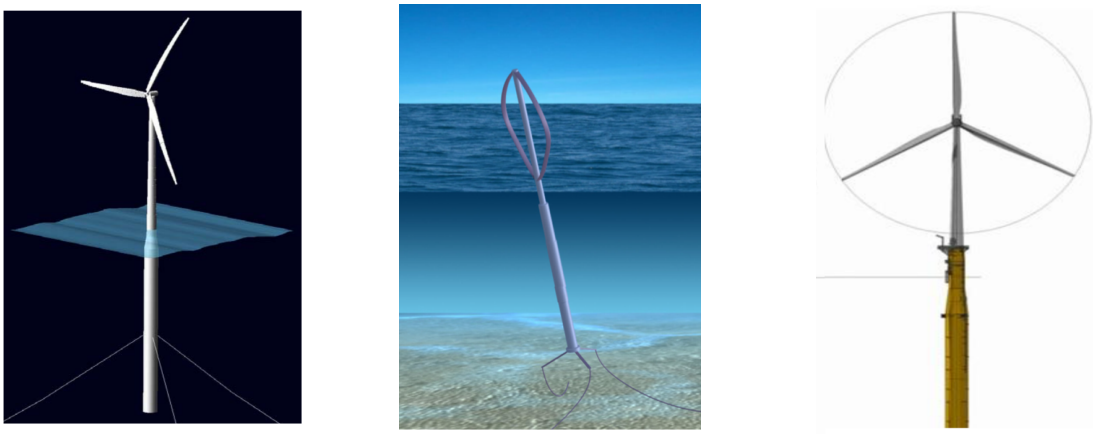

(a) NREL (b) DeepWind (c) Hywind

Figure 1.7: Visualizations of the NREL concept [18], DeepWind [5] and Hywind [1]

Control and Optimization of FVAWT

VAWTs have only one control input, unlike HAWTs which have two control inputs. A control strategy specific for land-based VAWTs has been developed by [19], using a filters and a Proportional Integral Derivative (PID) controller. The main idea was to filter the 2P fluctuations of the electrical torque, generated by the aerodynamic loads of the rotor with two blades. The control strategy implemented seemed to be successful, as the standard deviation of the electrical power was well reduced compared with the standard deviation of the aerodynamic power. The simplicity of the control system also seemed promising for upscaling of VAWTs.

Meanwhile, a PhD from DTU developed a first design of the DeepWind concept [4]. A stall regulated control system was used, making the reference signal easier to implement. However, this control set-up was not optimal, and the authors encouraged future research for optimization of the reference system. Following these recommendations, Wang & Cheng developed an improved control system [7], leading to an increase power production over rated wind speed, but not changing the value of the rated wind speed (U_r =14 m/s).

Moreover, Wang & Cheng used the NREL OC3 spar to support the DeepWind rotor, adapting the ballast of the OC3 spar [7]. This approach gave satisfying results in wind & wave conditions, but did not take advantage of the VAWT design characteristics, such as lower center of gravity. However, an optimized spar was designed for the DeepWind project [5], placing the generator of the turbine at the bottom of the spar, as shown in Fig. 1.8. An optimization algorithm was implemented, minimizing a cost function under a set of design constraints. This lead to a draft decrease from 120 m to 110 m and a diameter decrease from 9.4 m to 8.2 m compared with the original OC3 NREL spar. These results were encouraging for VAWTs, because less steel was needed for the spar design after optimization.

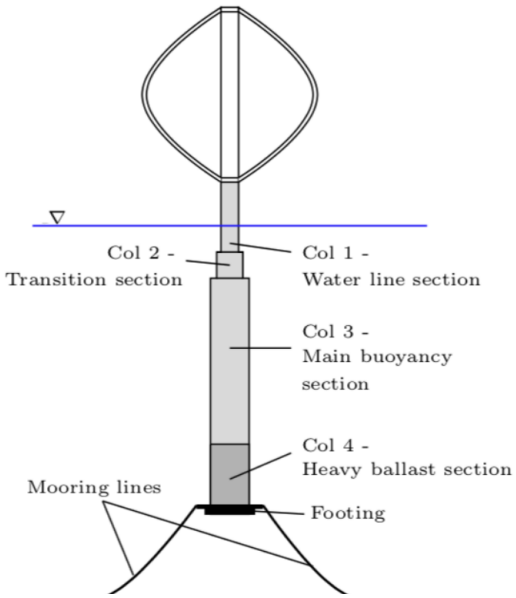

Figure 1.8: Spar design parameters for FVAWT optimization [5]

1.2.4 Upscaling of Wind Turbines

HAWT Upscaling

As presented in Fig. 1.9, there is a correlation between the increase of the diameter and the increase of the rated power of wind turbines with time. As collecting more wind power per turbine would certainly be an advantage for the future, research on upscaling is an active subject. Although structural considerations can be limiting factors, the 5 MW NREL HAWT concept [18] has been successfully upscaled to 10 MW DTU HAWT concept [20]. Both wind turbines have three blades and a rated wind speed of 11.4 m/s, but the DTU concept has larger dimensions. Indeed, the DTU diameter is 178.3 m against 126 m for the NREL, which makes sense as 126 times $\sqrt{2}$ gives 178.2, which means that the swept surface S and the theoretical available wind power $\mathcal{P}_o$ are doubled for the DTU HAWT ($\mathcal{P}_o = \frac{1}{2}\rho S U_o^3$).

Upscaling of offshore wind turbines is also of interest, and require some suitable floating structures. For instance, the OC3-Hywind spar platform has been adapted by [20] to support the 10 MW DTU HAWT, by increasing the spar diameter and keeping the same draft, and by checking the buoyancy and the hydrodynamic stability. Similarly, the WindFloat semi-submersible has been adapted by [21] to support the 10 MW DTU HAWT, with focus on dynamic analysis.

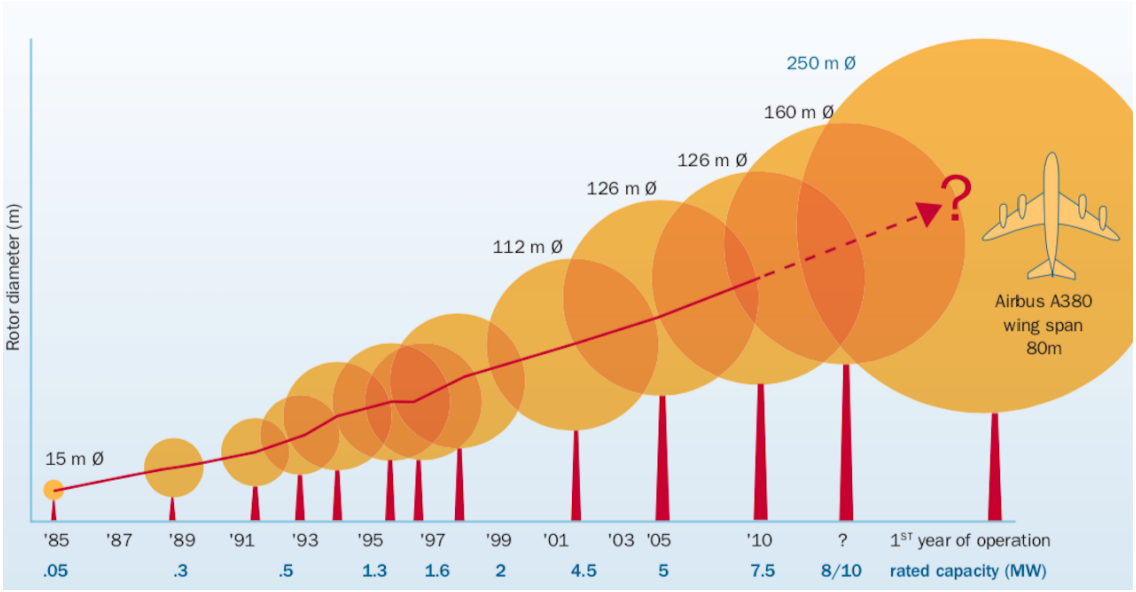

Figure 1.9: Upscaling trends for HAWT: rotor diameter versus rated capacity [25]

VAWT Upscaling

The 5 MW FVAWT DeepWind concept [5] has been upscaled to 10 MW with the INNWIND project [6]. The same physical principle was used as for HAWT upscaling, as the swept area of the Darrieus rotor was doubled in order to double the rated power. Fig. 1.10 depicts a representation of the 5 & 10 MW rotors in the vertical place, where the height and radius have been increased. This technique is called geometrical upscaling at constant tip-speed ratio (TSR), as the rated wind speed was kept the same (14 m/s).

As the mass of the rotor is also increased when upscaling, the spar had to be re-designed in order to support the 10 MW FVAWT. A spreadsheet calculation gave a stable solution for the spar design, with dimensions significantly higher than the DeepWind concept (184 m againt 110 m for the spar draft, 10.1 m against 8.2 m for the spar diameter). However some issues were encountered when upscaling the control system, as a very high standard deviation of the power output was observed for INNWIND, compared with the DeepWind published results.

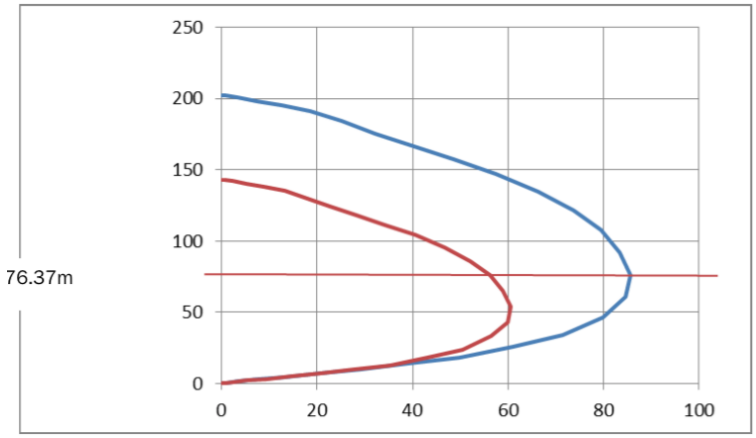

Figure 1.10: Rotor size comparison from DeepWind (5 MW) to INNWIND (10 MW) [6]

1.2.5 Design Summary

Table 1.1 summarizes the various FVAWT and FHAWT concepts developed so far, with focus on spar floating wind turbines. The corresponding drafts and diameters are reported, and both 5 & 10 MW wind turbines are compared. The concepts regrouped in Table [?] can serve as references for this thesis, from the academic research field and the offshore wind industry.

The published reference models from the research field include FHAWTs and FVAWTs, 5 and 10 MW. For FHAWTs, the 5 MW NREL [18] concept has been studied extensively, and the 10 MW DTU concept was mounted on a spar by [20] (simply noted "DTU" in this thesis). Similarly for FVAWTs, the 5 MW DeepWind [5] concept was developed and upscaled to design the 10 MW INNWIND [6] concept.

Two examples from the industry can be used as references for this thesis: Hywind (6 MW FHAWT, [1]) and Empire Wind (10-15 MW FHAWT, [13]). However, the dimensions of the Empire Wind are not known yet, although it will probably be an upscaled version of Hywind, as it is also a project of Equinor, and as Hywind Scotland was a pilot park.

From the Table [?], it can be observed that the 5 MW FVAWT DeepWind has a smaller draft than the NREL FHAWT, but a larger draft than the Hywind FHAWT. Although this shows some differences between FVAWTs and FHAWTs, it is not really conclusive on the advantages of VAWT. Moreover, the 10 MW FVAWT INNWIND has a very large draft compared with the DTU model. This shows that the some progress has still to be done when it comes to spar upscaling for FVAWTs, as the lower center of gravity of FVAWTs should enable to design smaller drafts.

Category	Power	5 MW	10 MW
Research: FHAWT	Concept	NREL	DTU
	Draft [m]	120	120
	Diameter [m]	9.4	12
Research: FVAWT	Concept	DeepWind	INNWIND
	Draft [m]	110	184
	Diameter [m]	8.2	10.1
Industry: FHAWT	Project	Hywind	Empire Wind
	Draft [m]	78	-
	Diameter [m]	14.4	-

Table 1.1: Current research and industry designs of FHAWT and FVAWT using spars, with the corresponding spar main dimensions [5], [6], [18],[20], [1], [13]

1.3 VAWTs Analysis in SIMO

1.3.1 Module Architecture

Fig. 1.11 presents the VAWT module implemented in SIMO, with its main code blocks: aerodynamics (blue), control (yellow), rotor (green). The code architecture is described as it reflects the physics and engineering of VAWTs, however the details of the code implementation are not included here. The aerodynamic block implements the Double Multiple Streamtube (DMS) theory, and computes the aerodynamic loads (such as the aerodynamic torque Q) from the wind speed U, the rotor speed ω and the rotor azimutal position ψ.

The control block computes the electrical torque T (also called generator torque), which is the only control input of the system. First, the reference speed ω_{ref} is determined by the reference block, which contains a look-up table (U,ω_{ref}) where U is the mean wind speed. The filter block originally had a 2P-notch filter and a low pass filter, and gives the filtered rotor rotational speed $\hat{\omega}$. Then, a PI (Proportional Integral) computes the electrical torque T, trying to minimize the error $\omega_{ref} - \hat{\omega}$. This control procedure was successfully developed and teste by [19], in constant wind and turbulent wind conditions. In particular, the filtering step makes the electrical torque more smooth, and limits the electrical power fluctuations.

The rotor block models the rotor dynamics, which is basically a vertical axis rotational motion, with an inertia excited by the aerodynamic torque Q and the electrical torque T. In the start-up phase, the electrical torque helps the rotor to reach its desired rotational speed ω_{ref} from the start value 0 rad/s. In the stationary phase, the electrical torque acts in the opposite direction of the aerodynamic torque, and the mean value of the aerodynamic power is transferred to the grid as electrical power, such as $\bar{\mathcal{P}}_{aero} = \bar{\mathcal{P}}_{elec}$. This can be interpreted physically as the energy conversion of the system.

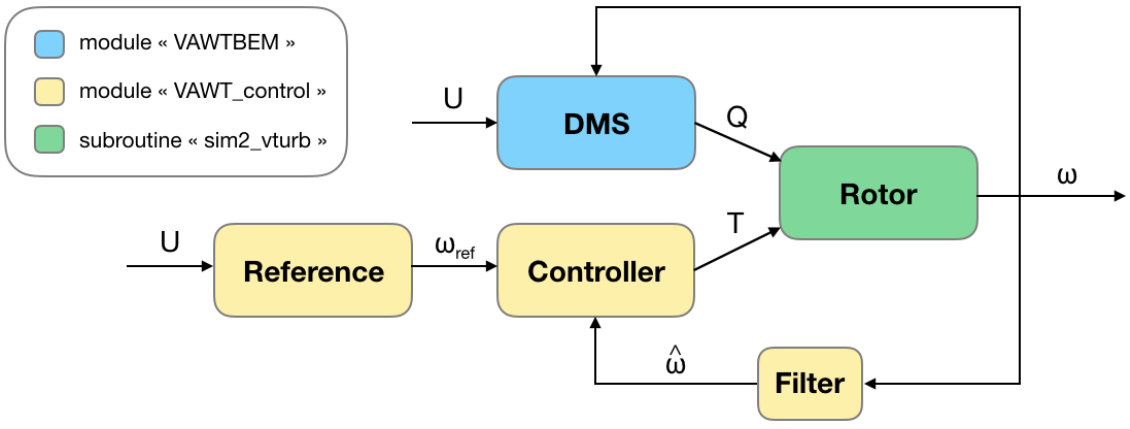

Figure 1.11: Architecture of SIMO aerodynamic and control VAWT module

1.3.2 Current Issues

For a well-functioning control system, one could expect that a stationary state should be reached after convergence of the controller, i.e. when $\omega \sim \omega_{ref}$. In that case, the mean powers should be equal, whic entails that the mean values of the torques should also be equal $\bar{Q} = \bar{T}$, as by definition of the aerodynamic and electrical powers, $\mathcal{P}_{aero} = Q\omega$ and $\mathcal{P}_{elec} = T\omega$.

To investigate the present version of SIMO, the VAWT module was tuned and run for the 5 MW example, under the rated conditions from [7]: $U = 14$ m/s and $\omega_{ref} = 0.544$ rad/s. The preliminary results are presented in Fig. 1.12, which depicts the time series of the power signals, torques and rotor speeds. From this preliminary analysis, some issues can be observed and listed below, where the stationary state was considered reached after 400s. These observations motivated the further debugging of the SIMO VAWT code.

- The mean aerodynamic power is smaller than expected [7]: $\bar{\mathcal{P}} \sim 4.55$ MW < 5 MW.
- The mean electrical torque converges to only half the value of the mean aerodynamic torque, which does not satisfies the conservation of energy: $\bar{Q} \neq \bar{T}$.
- The filtered rotational speed does not converge towards the rotor speed, and tuning does not affect this observation: $\hat{\omega} \neq \omega$.

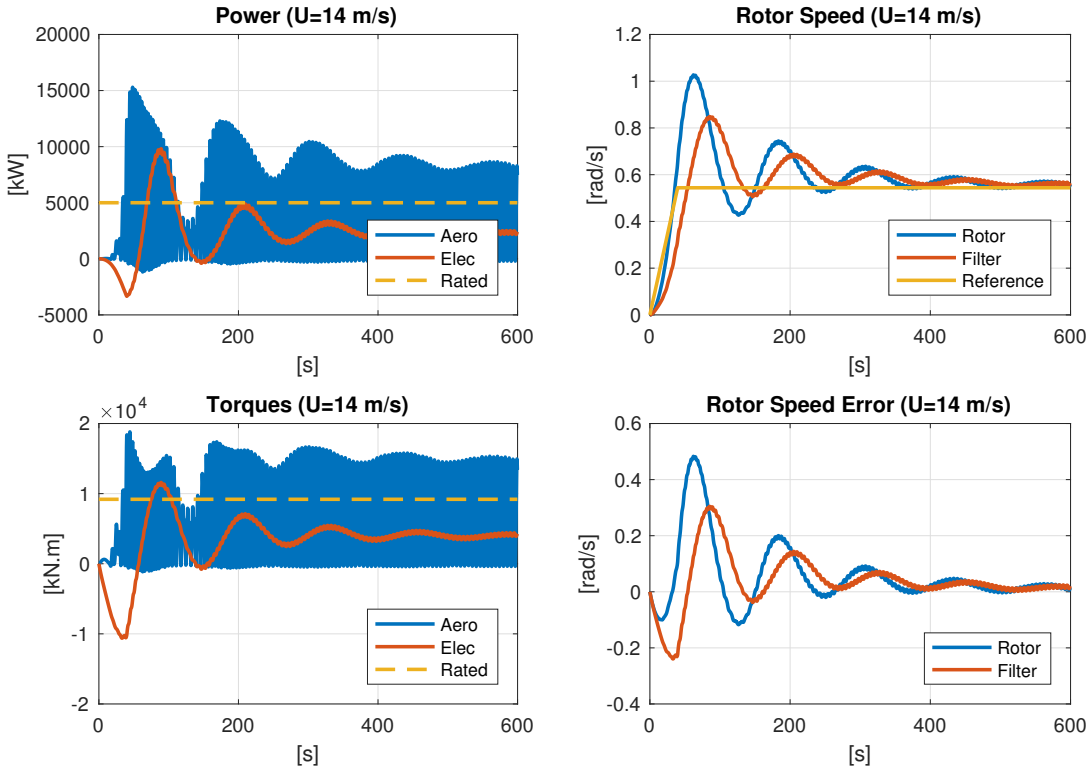

Figure 1.12: Example of VAWT time series obtained with the current version of SIMO

Chapter 2: Methods

This chapter presents the various methods used to design the 5 & 10 FVAWTs, with focus on aerodynamics, control system optimization, upscaling, and spar design optimization. The final design parameters values are summarized in the design summary section. The first section briefly presents some control upgrades, along with some updated results obtained from the debugged SIMO version.

2.1 SIMO Debugging

The main issues mentioned in the introduction chapter related to SIMO were investigated closely. In particular, the notch and low pass filters were tested with MATLAB, and the PI controller was tested with SIMULINK. Moreover, the DMS theory as described by [19] was briefly implemented in MATLAB, in the simplified case of zero induced velocity and no dynamic stall or inflow delay. By comparing the recreated results with the SIMO results, some errors were identified in the source code and corrected, leading to some updated outputs more in agreement with the published values [22]. Some other upgrades were brought to the code, as a 4P-notch filter was added to the existing 2P-notch filter, and a more simple first order low pass filter was implemented for the wind speed filtering:

$$\frac{d\bar{U}}{dt} = \frac{1}{\tau_u}(U - \bar{U}) \tag{2.1}$$

Some time series of the upgraded results are presented in Fig. 1.1, for ω_{ref}=0.544 rad/s and U =14 m/s, defined as the rated conditions by [22]. When comparing the time series from Fig. 1.1 and Fig [?] from the introduction, some major differences can be observed, especially regarding the convergence of the various variables. In particular for the new results, the electrical power converges towards the rated power, and the rotor rotational speed converges towards its rated value (assigned to the reference rotational speed), which was expected. Also the mean electrical power converges towards the mean aerodynamic power, which satifies the conservation energy in stationary state, which was checked by comparing their mean values of the time series from 100 s, i.e. after the transient regime.

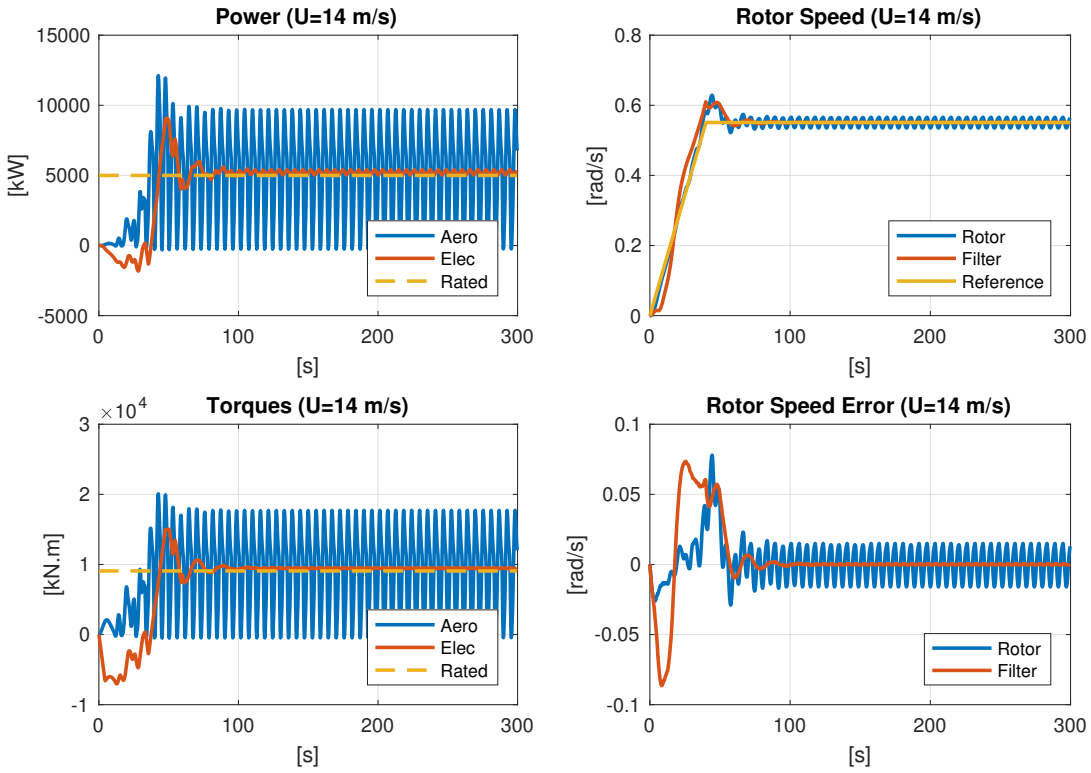

Figure 2.1: Example of time series obtained with the debugged version of SIMO

2.2 Aerodynamics of VAWTs

2.2.1 Double Multiple Streamtube Theory

DMS in SIMO

The aerodynamic code implemented in SIMO is based on the Double Multiple Streamtube (DMS) theory. The aerodynamic loads on the rotor are computed at a given time, depending on the wind speed U, the rotor azimutal position ψ, and the rotational speed ω. The parameters of the blades are given to SIMO as inputs, such as the lift coefficient C_L as a function of the angle of attack α, known for the NACA blade profile chosen by [4].

The DMS theory can be compared with the BEM (Blade Element Momentum Theory) for HAWTs, as it is also divided in three steps: (i) computation of the lift and drag forces on the blades for the given relative wind velocity V_r, (ii) computation of the induced velocity based on the conservation of momentum, and (iii) iteration at each time step to find the correct induction factors. Some model refinements such as dynamic stall and inflow delay are also implemented in the aerodynamic code. For simplicity, the DMS theory presented in this report is for zero tilt angle, which means that the rotation axis is the vertical axis.

Local Aerodynamic Forces

Fig. 2.2 (a) shows the kinematics of a rotating blade of a VAWT. Please note that the azimutal angle is noted θ in this subsection, and not ψ as usual. In particular, the relative velocity V_r is assumed to be known, such that the angle of attach α is known too. Then the lift and drag forces that act on the rotating blades generate a tangential force and a normal force in the local coordinate system, and the local tangential force generates an aerodynamic torque. In particular, the magnitude of the relative velocity can be found as [27]:

$$V_r = V_\infty \sqrt{((1-a)sin\theta)^2 + ((1-a)cos\theta)^2 + \lambda} \tag{2.2}$$

with the TSR $\lambda = \frac{\omega R}{V_\infty}$, the induction factor $a = 1 - \frac{V_a}{V_\infty}$, the rotor radius R and the rotational speed of the turbine ω. Moreover, some geometrical considerations give $tan(\alpha) = \frac{V_a sin\theta}{V_a cos\theta + \omega R}$, which can be inverted as follows:

$$\alpha = tan^{-1}\Big(\frac{(1-a)sin\theta}{(1-a)cos\theta + \lambda}\Big) \tag{2.3}$$

From the airfoil data, one can deduce (C_L,C_D), and the aerodynamic forces in the rotating coordinate system. A transformation matrix is used to obtain the forces in the global coordinate system.

Momentum Balance

The relative velocity used in the kinematic part can be obtained from the equation [26]:

$$V_r = V_o + V_i - V_b \tag{2.4}$$

taking into account the blade velocity V_b and the induced velocity V_i. The induced velocity is computed from the momentum ballance for a given streamtube [26], as shown in Fig. 2.2 (b):

$$F = -2\rho A_e f \mid (V_o + fV_i).n \mid V_i \tag{2.5}$$

with f the Prandtl factor, approximated as $f = 1$ for a Darrieus rotor (tip loss effects negligible, as the tips of the blades are connected to the tower). Physically speaking, the induced velocity that appears in the momentum conservation accounts for the energy loss of the air flow given to the rotor. After a few iterations, the induction factor can be evaluated at each time step, and ghost blades are introduced in SIMO to simplify the numerical resolution of the problem.

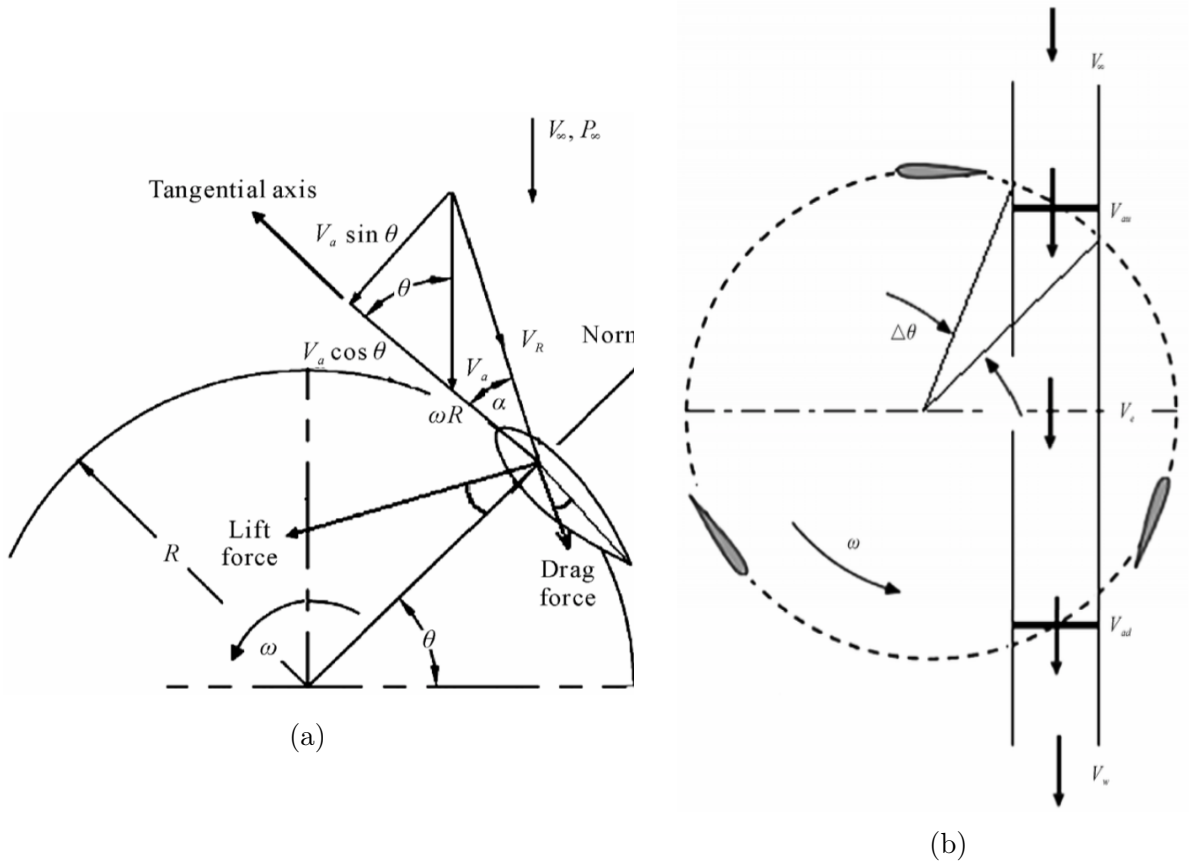

Figure 2.2: (a) Kinematics of a VAWT [27] (b) Visualization of a streamtube [27]

2.2.2 Dynamic Stall

A dynamic stall (DS) model is also implemented in SIMO, based on the Øye method [26]. As shown in Fig. 2.3, the dimensionless position of the separation point s is introduced, which takes values between -1 and 1 depending on which side of the blade it is located. It is a dynamic variable, to be differentiated from s_q, which is the quasi-steady position of the separation point, function of the angle of attack α. The evolution of the separation point dynamic position is governed by the first order linear differential equation:

$$\frac{ds}{dt} = \frac{s_q - s}{\tau} \tag{2.6}$$

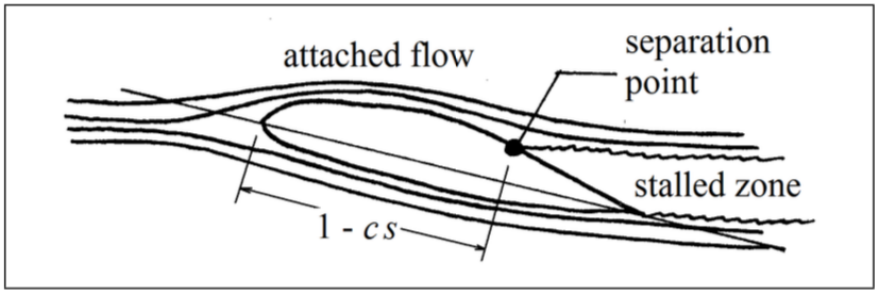

Figure 2.3: Separation point parametrization [26]

The values of the lift coefficient are updated in SIMO using the Kirchhoff formula as follows, valid for $\mid s \mid < 1$:

$$C_L = \frac{1}{4}\Big(\frac{dC_L}{d\alpha}\Big)_a (\alpha - \alpha_o)\big(1 + \sqrt{1 - \mid s \mid}\big)^2 \tag{2.7}$$

with α_o the angle of attack at zero lift, and:

$$\Big(\frac{dC_L}{d\alpha}\Big)_a = max_{\alpha_q}\Big[\frac{C_{L,q}}{\alpha_q - \alpha_o}\Big] \tag{2.8}$$

Additionally, if the stall model predicts an evolution such as $\mid s \mid > 1$, it means the separation point is beyond the edge of the blade, which is not realistic. Therefore in that case, the quasi-steady coefficient curve is used to estimate C_L. The combined use of DMS and DS gives quite accurate results compared with experimental data [26].

2.2.3 Stand-Alone DMS in SIMO

The stand-alone results were obtained in SIMO by deactivating the aerodynamic forces on the rotor, in order to give a constant rotational speed to the rotor with the PI controller only. Fig. 2.4 presents plots of the mean aerodynamic power obtained from the stand-alone DMS, for various wind speeds and various rotational speeds. From Fig. 2.4, the power coefficient was computed and plotted in Fig. 2.5 as a function of the TSR, using the following formula:

$$C_p(\omega, U) = \frac{\mathcal{P}(\omega, U)}{\frac{1}{2}\rho A U^3} \tag{2.9}$$

where A is the area of a vertical cross section of the swept volume of the rotor. In particular, the various curves overlap in Fig. 2.5, and the maximum power coefficient was found as $C_P^* = 0.455$ for $TSR^* = 4.1$. These values define the optimal aerodynamic conditions of the studied VAWT, i.e. the values for which the mean aerodynamic power is maximal. This 45% efficiency value is quite close to the value of a HAWT, and below the Betz limit (theoretical upper limit of 59% efficiency for any type of turbine). Therefore, the optimal mean power plotted in Fig. 2.4 can be expressed as a function of the wind speed U:

$$\mathcal{P}^*(U) = \frac{1}{2} C_p^* \rho A U^3 \tag{2.10}$$

Additionally, the optimal rated wind speed can be expressed theoretically inverting Eq. (2.10):

$$\begin{cases} \mathcal{P}_r = 5 \text{ or } 10 \text{ MW} \\ U_r = \mathcal{P}^{*-1}(\mathcal{P}_r) \end{cases} \tag{2.11}$$

For the 5 MW VAWT, the resulting rated wind speed value 11.85 m/s was rounded up to 12 m/s, for peak shaving purpose of the reference speed signal. This value is smaller than the 14 m/s value from [4], which should lead to an increase of the VAWT power output at 12 m/s.

Fig. 2.6 presents plots of the thrust, torque and separation point variable as functions of the azimutal angle of the rotor. In particular, it appears that the aerodynamic thrust is 2P periodical, as it varies periodically twice between 0 and 360 degrees. Moreover, the aerodynamic torques also seems to be 2P periodical, or even 4P periodical for the 25 m/s case. Finally, the dynamic stall effect is more accentuated at higher wind speeds (25 m/s), as the separation point variable takes more extreme values in that case. This might explain why the 4P effect seems more important for the aerodynamic torque in the 25 m/s case.

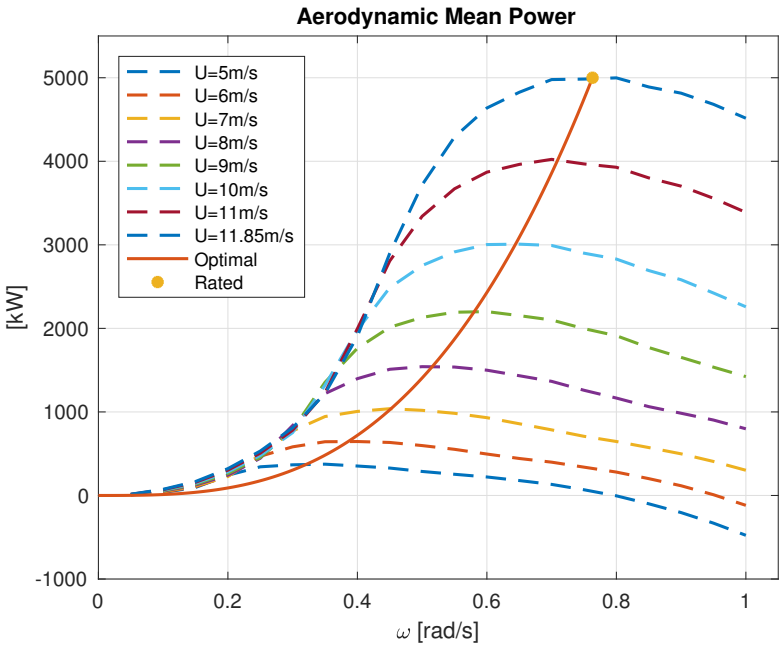

Figure 2.4: Aerodynamics mean power diagram obtained for the 5MW VAWT in SIMO

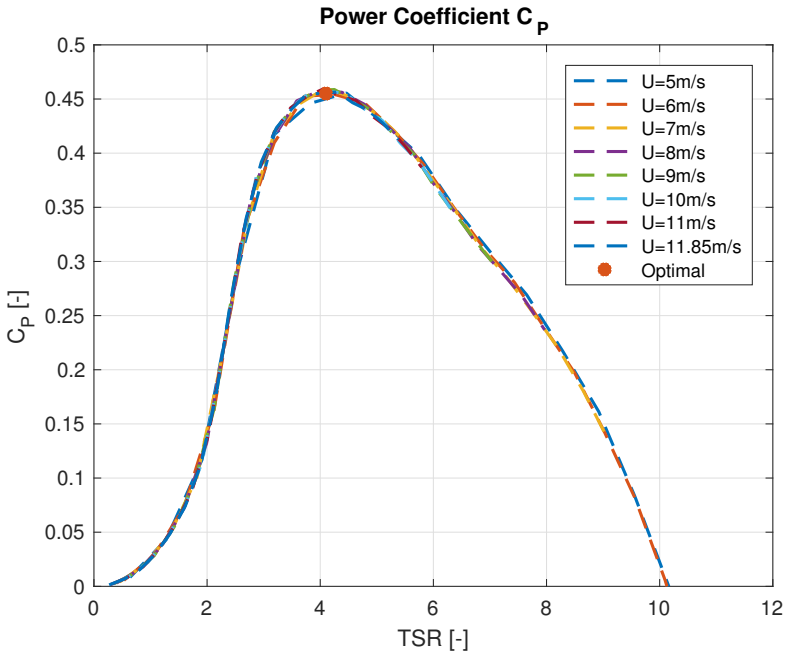

Figure 2.5: Aerodynamics power coefficient curves, for various wind speeds

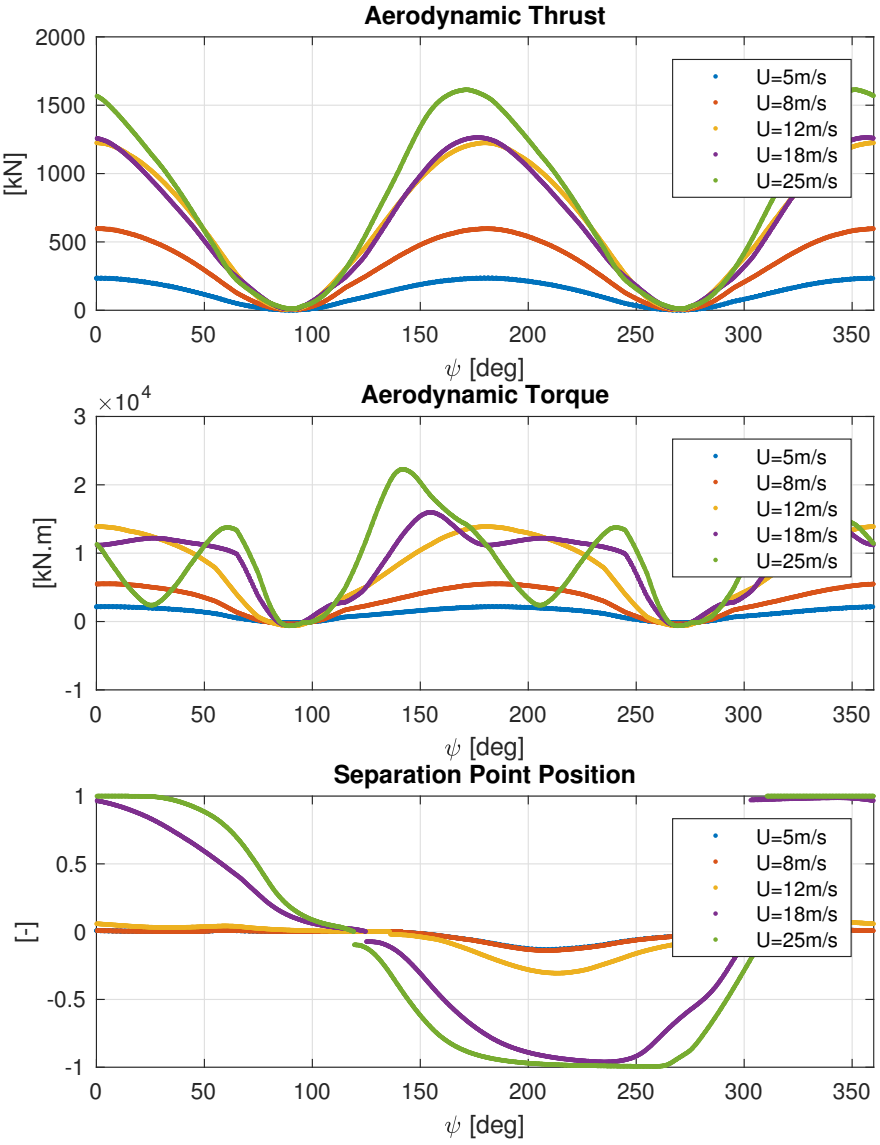

Figure 2.6: Aerodynamics thrust, torque and separation point as functions of the rotor azimutal position ψ

2.3 Control System Optimization

The VAWT converts the wind kinetic energy in rotational kinetic energy of the rotor. Then, the generator converts the rotor kinetic energy in electrical energy transferred to the grid. In order to deliver a steady generator power, the control law that computes the generator torque includes a filter, as shown in Fig. 1.11. Moreover, VAWTs only have one control input, the generator torque T. In SIMO, T is computed using a PI controller, whose objective is to keep the filtered rotor rotational speed $\hat{\omega}$ close to a reference signal ω_{ref} [19]:

$$T = -K_P \Delta\omega - K_I \int_0^t \Delta\omega dt \tag{2.12}$$

with

$$\Delta\omega = \hat{\omega} - \omega_{ref} \tag{2.13}$$

and with $\hat{\omega}$ obtained after filtering of ω.

The reference rotor speed signal ω_{ref} was chosen in order to optimize the power production of the VAWT. In particular, the mean aerodynamic power should be maximized below rated, and kept constant above rated. The control optimization objective can be stated as follows: *find the reference rotor speed function $\omega_{ref}(U)$, such as the mean aerodynamic power $\mathcal{P}$ verifies:*

$$\mathcal{P}(U, \omega_{ref}) = \begin{cases} \mathcal{P}^*(U) & \text{if } U \leq U_r \\ \mathcal{P}_r & \text{if } U \geq U_r \end{cases} \tag{2.14}$$

using the same notations as in the aerodynamic section, where the rated power was $\mathcal{P}_r = 5$ MW and the optimal rated wind speed $U_r = 12$ m/s. In particular below rated, the TSR should be optimal, such as $\omega_{ref}(U) = TSR^* \frac{U}{R}$. Above rated, the values of the reference signal verifying the control objective were found from an analysis of the mean aerodynamic power diagrams, for values of U from 12 to 25 m/s.

Table 2.1 presents the optimized reference signal values and the corresponding wind speeds. The distinction is made from below rated, rated speed, and above rated for clarity. Noticeably only two significant digits were considered as precise enough below rated, whereas thress digits were needed above rated, due to steeper curves in this part of the power diagram. The resulting optimized mapping (U, ω_{ref}) was implemented in SIMO for the 5 MW VAWT, and upscaled for a 10 MW VAWT following the rules of the next section.

Category	U [m.s^{-1}]	ω_{ref} [rad.s^{-1}]
Below rated wind speed	5	0.32
	6	0.39
	7	0.45
	8	0.51
	9	0.58
	10	0.64
	11	0.71
Rated wind speed	12	0.656
Above rated wind speed	13	0.554
	14	0.541
	15	0.542
	16	0.548
	17	0.554
	18	0.558
	19	0.557
	20	0.554
	21	0.549
	22	0.544
	23	0.538
	24	0.531
	25	0.526

Table 2.1: Control system reference mapping (wind speed, rotational speed)

2.4 Upscaling from 5 to 10 MW

Upscaling techniques are usually based on geometric and aerodynamic similarity, which means that the TSR is kept constant while the dimensions of the rotor are increased [28]. In particular, theoretical upscaling laws can be applied to weight and power as follows: $M \sim \kappa^3$ and $\mathcal{P} \sim \kappa^2$, with κ the geometrical scaling factor ($L \sim \kappa$).

Consequently, in order to double the aerodynamic power from 5 to 10 MW, the geometric scaling factor has to be chosen as $\kappa = \sqrt{2}$. Similarly, some dimensional analysis can be done for the rotational inertia, the aerodynamic torque, or the tuning gains K_P and K_I. As summarized in Table 2.2, each physical variable variable has a specific unit, which is a combinations of meters, kilograms, and seconds. Meters scale according to κ, kilograms according to κ^3, and seconds according to κ. Indeed, the wind speed U is not changed while upscaling the wind turbine, and the TSR ($\lambda = \frac{R\omega}{U}$) is kept constant, which means that $\omega \sim \kappa^{-1}$. Therefore the various scaling factors can also be deduced, and are summarized in Table 2.2.

For the rotor, the main dimensions such as the chord, radius, height were upscaled according to $L \sim \kappa$, and the mass and inertias were also upscaled. For the control system, the reference rotor speed was scaled according to $\omega_{ref} \sim \kappa^{-1}$, and the K_P and K_I coefficients were also upscaled and slightly modified for enhanced stability. Finally, a spar was designed and optimized to support the upscaled 10 MW rotor, as described in the next section.

Design	Parameter	Unit	Scaling factor
Geometry	Length	m	κ
	Mass	kg	κ^3
	Inertia	kg.m^2	κ^5
Aerodynamics	TSR	-	1
	Wind Speed	m.s^{-1}	1
	Rotor Speed	rad.s^{-1}	κ^{-1}
	Torque	kg.m^2.s^{-2}	κ^3
	Power	kg.m^2.s^{-3}	κ^2
Control	K_P	kg.m^2.s^{-1}	κ^4
	K_I	kg.m^2.s^{-2}	κ^3
	ω_{ref}	rad.s^{-1}	κ^{-1}

Table 2.2: Upscaling considerations for a VAWT

2.5 Spar Design & Optimization

This section presents the spar design theory, along with the hypothesis made and the formulas used for a given spar design. Then the optimization method is detailed, leading to the choice of spar designs for the 5 & 10 MW FVAWTs.

2.5.1 Spar Design

Spar Modelling

A simplified spar model was used for the design of a FVAWT, as proposed by [5]. Figure 2.7 depicts the five different parts of the spar, from the bottom to the top. The generator is placed at the bottom of the spar, and the ballast section is positioned above the generator. A top column with a smaller diameter is supposed to minimize the hydrodynamic excitation loads generated by the waves, and a tapper section makes the transition to the base column.

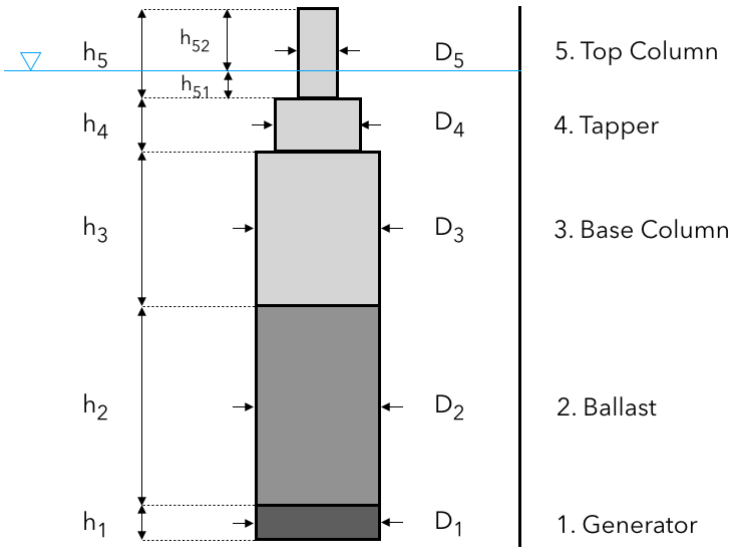

Figure 2.7: VAWT simplified spar design, as proposed by [5]

Hypothesis

The spar design theory was implemented using several simplified hypothesis. For instance, the degrees of freedom (DOFs) were assumed to be uncoupled for the dynamic analysis. Pitch and heave eigenfrequencies were computed from buoyancy forces only, while surge and yaw motions were assumed to be regulated by the mooring lines. As described in Fig. 2.7, the spar geometry was described as a pile of slender bodies. Morison's equation was used to compute the quadratic damping coefficients of the slender bodies. The generator parameters of the 5 MW spar were taken from the 5 MW DeepWind concept [5] (M_{gen},M_{blade},h_1,D_1). The top column height h_5 and tapper height h_4 values were taken from the 5MW NREL model [18]. Moreover, D_5 was used as an adjustment variable for the heave eigenfrequency,

while it was assumed for simplicity:

$$\begin{cases} D_3 = D_2 \\ D_4 = \frac{D_3+D_5}{2} \end{cases} \tag{2.15}$$

Under these assumptions, the spar parameters can be determined for a given couple (draft spar, mean diameter), noted (d,D_2). The following equations have been implemented in MATLAB, for optimization purposes.

Hydrostatic Balance

The hydrostatic balance needs to be verified for the FVAWT to be statically stable. First, slender bodies possess cylindrical properties and are easily implemented in SIMA:

$$a_i = \frac{\pi}{4} D_i^2 \tag{2.16}$$

$$V_i = h_i a_i \tag{2.17}$$

The 2D added mass can be found as:

$$A_i = \rho_w \pi a_i \tag{2.18}$$

while the 2D quadratic damping is obtained from Morison's equation:

$$C_{x,i} = \frac{1}{2} \rho_w 0.7 d_i \tag{2.19}$$

The displace volume of water is obtained by summation:

$$V_{dis} = V_1 + V_2 + V_3 + V_4 + V_{5,1} \tag{2.20}$$

$$M_{dis} = \rho_w V_{dis} \tag{2.21}$$

The mass of steel of the floating structure is approximated as:

$$M_{steel} = 0.13 M_{dis} \tag{2.22}$$

while the mass of the shast is approximated as:

$$M_{shaft} = \rho_{blade}(H + h_{5,2} + d - h_1); \tag{2.23}$$

with ρ_{blade} the linear density of the blade (about 1 ton per meter):

$$\rho_{blade} = \frac{M_{blade}}{L_{blade}} \tag{2.24}$$

$$M_{tot} = M_{dis} \tag{2.25}$$

From the hydrostatic balance, the required ballast mass is given as follows:

$$M_{bal} = M_{dis} - M_{rot} - M_{shaft} - M_{gene} - M_{steel} \tag{2.26}$$

The ballast fraction BF and (h_2,h_3) can be further deduced:

$$BF = \frac{M_{bal}}{\rho_c V_{dis}} \tag{2.27}$$

$$h_2 = BF\frac{V_{dis}}{a_2} \tag{2.28}$$

$$h_3 = d - h_1 - h_2 - h_4 - h_{5,1} \tag{2.29}$$

Dynamic Analysis

The heave hydrostatic stiffness of a spar is simply given as:

$$C_{33} = \rho_w g a_5 \tag{2.30}$$

The heave added mass can be found approximating the main column as sphere:

$$A_{33} = \rho_w \frac{\pi}{12} d_2^2 \tag{2.31}$$

The heave eigenperiod can be computed from the following formula:

$$T_{33} = 2\pi\sqrt{\frac{M_{tot} + A_{33}}{C_{33}}} \tag{2.32}$$

The pitch hydrostatic stiffness of a spar is given by [29]:

$$C_{55} = \rho_w g V_{dis}(\frac{I}{V_{dis}} + Z_B - Z_G) \tag{2.33}$$

Approximating the pitch added mass using strip theory:

$$A_{55} = \rho_w a_2(\frac{d^3}{12} + d(Z_B - Z_G)^2) \tag{2.34}$$

We finally get:

$$T_{55} = 2\pi\sqrt{\frac{I_{55,tot,0} + A_{55}}{C_{55}}} \tag{2.35}$$

with the rotational inertias summed as follows:

$$I_{55,tot,0} = I_{55,rot,0} + I_{55,steel,0} + I_{55,shaft,0} + I_{55,gen,0} + I_{55,bal,0} \tag{2.36}$$

For the rotor, the inertia along the water line is computed using the parallel axis theorem:

$$I_{yy,0} = I_{yy,CG} + M_{rot} Z_{rot}^2 \tag{2.37}$$

and the rotor center of gravity can be found as:

$$Z_{rot} = h_{5,2} + \frac{H}{2} \tag{2.38}$$

2.5.2 Spar Optimization

Optimization Constraints

Two spar buoys were designed to support the 5 & 10 MW VAWTs, accounting for hydrodynamic stability, maximum pitch angle (10°) and frequency placement. A MATLAB algorithm was implemented to test a set of 5 condition for many values of (d,D_2) (draft and main diameter). The spar optimization objective is *to minimize the draft with respect to the following constraints:*

1. *Hydrostatic stability:* $M_{total} = M_{displaced}$
2. *Hydrodynamic stability:* $C_{55} > 0$
3. *Maximum pitch angle:* $\eta_{55} < 10°$
4. *Mathieu instability:* $\omega_{33} \neq \omega_{55}$
5. *Excitation frequencies:* $\omega_{ii} \neq \left\{\omega_{wave}, \omega_{2P}, \omega_{4P}\right\}$

Optimization Algorithm

A MATLAB algorithm was implemented to test the set of conditions {C1,C2,C3,C4,C5}. For each input value of the diameter, many values of draft were tested, and the smallest was stored, giving an optimal point (d^*,D_2^*). All resulting optimal points were plotted in Fig. 2.8, which represents the optimized diameter, mass and cost as functions of the draft. Various materials were tested for the ballast: concrete, water, and steel. Concrete was selected as an advantageous option, as it gave a relatively low cost for the spar, along with small drafts and diameters. The cost of materials was calculated using data from [10]: 0.1 \$/kg for concrete and 0.7 \$/kg for steel.

Fig. 2.9 presents the stability diagrams for the 5 MW spar, which shows which areas of the (d,D_2) plane are unstable for the conditions C2, C3, C4. The C3 condition appear to be stronger than the C2 condition, as having a maximum pitch angle is a more strict condition than verifying the hydrodynamic stability. However C1 and C5 are not plotted because they were systematically verified for the studied designs. In particular, the orange diameter curve of Fig. 1.8 corresponds to the lower border of the stability domain depicted in Fig. 2.9. Similarly, Fig. 2.10 presents the stability diagrams for the 10 MW spar, compared with reference values from the literature. Among all the possible solutions, a 50 m (90 m) draft was selected for the 5 MW (10 MW) spar, preferring small drafts over small diameters. Overall by lowering the generator and increasing the spar diameter, the 5 MW draft was minimized to 50m, smaller than the 5MW VAWT DeepWind [5] and the 6MW HAWT Hywind [1].

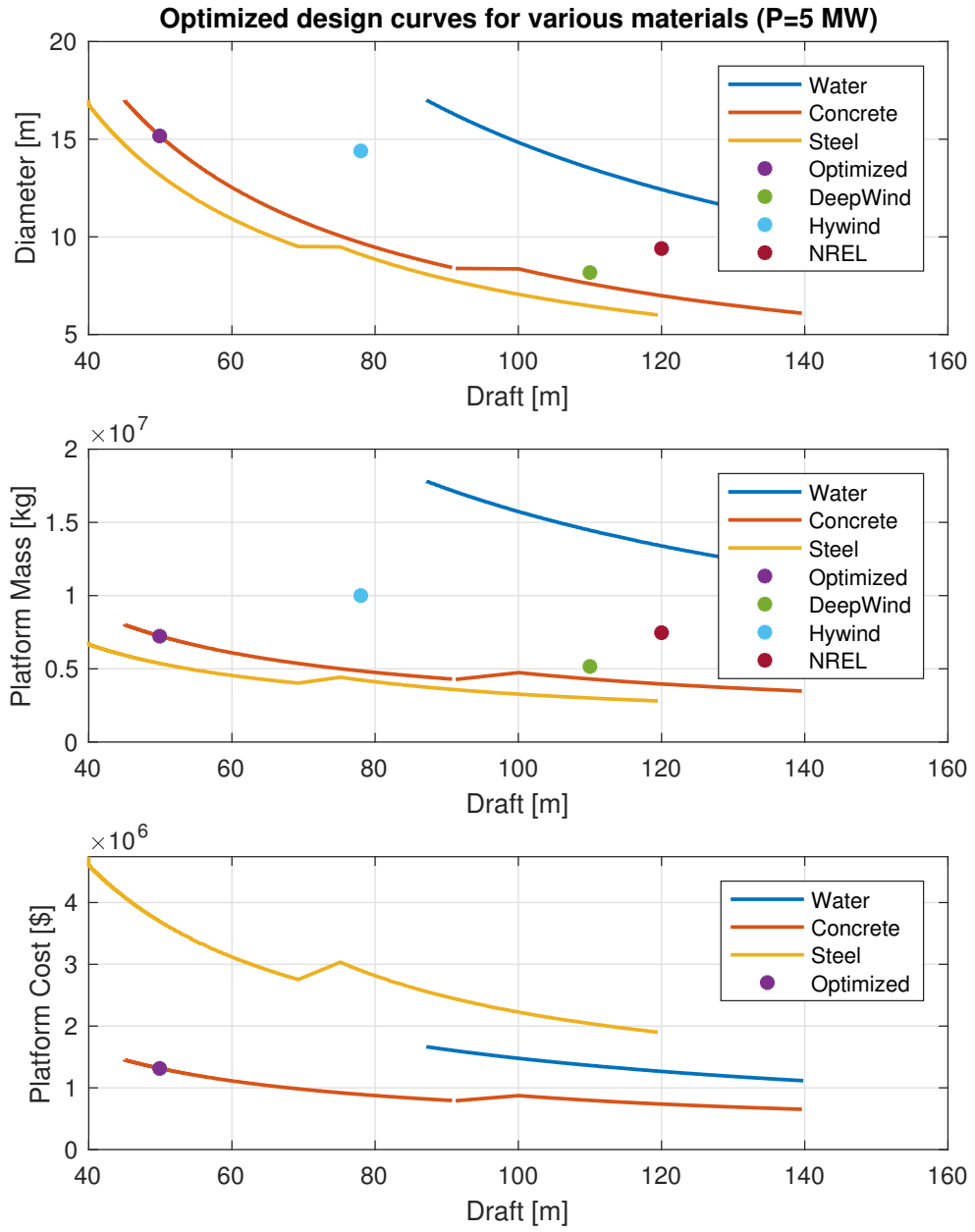

Figure 2.8: Optimized diameter, mass, and cost as functions of draft for various materials, compared with literature values (5 MW FVAWT)

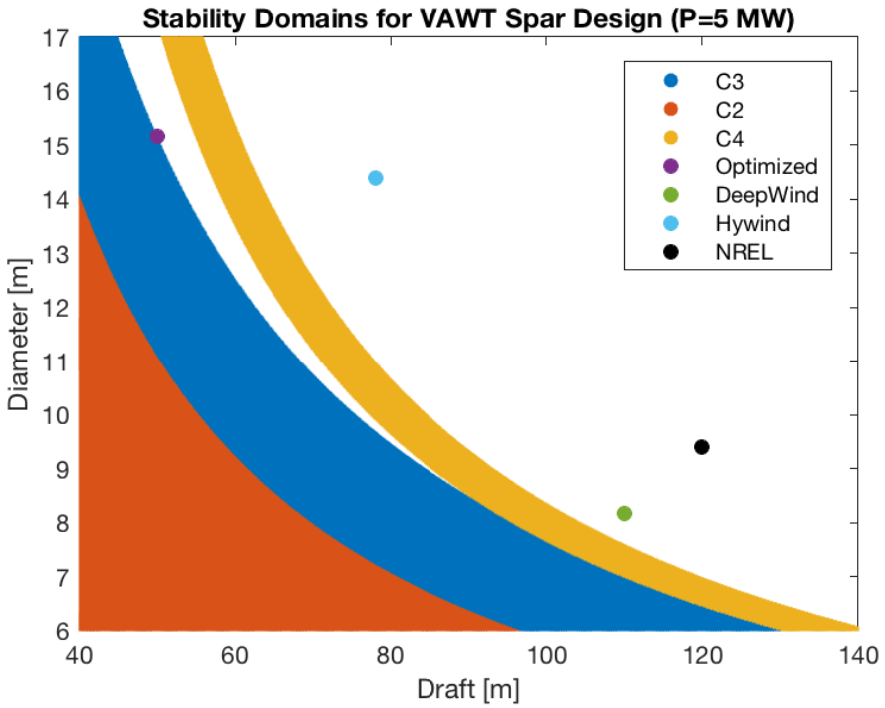

Figure 2.9: Stability domains in the (draft, diamter) plane for the 5 MW FVAWT

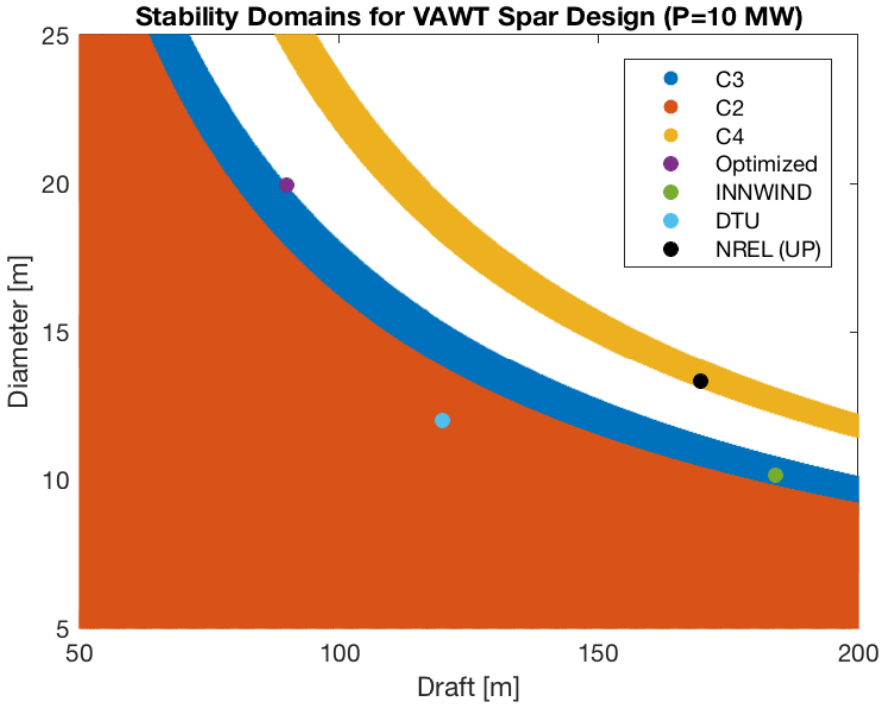

Figure 2.10: Stability domains in the (draft, diamter) plane for the 10 MW FVAWT

2.6 Design Summary

Following the control system optimization, the floating system optimization, and the upscaling from 5 to 10 MW, the resulting design parameters of the 5 & 10 MW FVAWTs are summarized in this section, as a reference for further SIMA implementation.

Figure 2.11 compares the 5 & 10 MW FVAWT designs with the 6 MW FHAWT Hywind [1], currently operating in Scotland. In particular, it can be observed that the 5MW FVAWT concept has a smaller draft (50 m instead of 80 m) and a smaller height above water (140 m instead of 178 m) than the Hywind concept. However, the 10 MW FVAWT has a larger draft (90 m against 80 m) and a larger height above water (200 m againt 178 m) than the Hywind concept.

Table 2.3 presents the main parameters of the 5 & 10 MW VAWTs, with focus on rotor geometry, rotor structure, aerodynamics and control system. In particular, the 5 MW blade parameters were found in [4] (length, inertia, mass), and upscaled according to their respective upscaling factor. The reader is reported to the nomenclature for the list of symbols. It can be noted that the Ki, Kp entry values entered in SIMO are multiplied by 1000, and that all parameters in Table 2.3 are given in S.I. units.

Table 2.4 presents the main parameters of the 5 & 10 MW FVAWTs, with focus on spar geometry, spar structure, stiffness, damping, and characteristic periods. The geometry of each slender body is detailed, and can be used to compute their respective 2D added mass and quadratic damping. It can be noted that there is no obvious scaling rule between the 5 & 10 MW spar parameters, as two different spars were designed and optimized for each model. For instance, lengths do not scale with a $\sqrt{2}$ ratio, and the mean water line heights were kept the same, as waves are attenuated with the same characteristic depth in any case. It can also be noted that the shaft is incorporated inside the spar in this thesis, unlike for the DeepWind concept where the whole spar was spinning, generating viscous losses and Magnus effect.

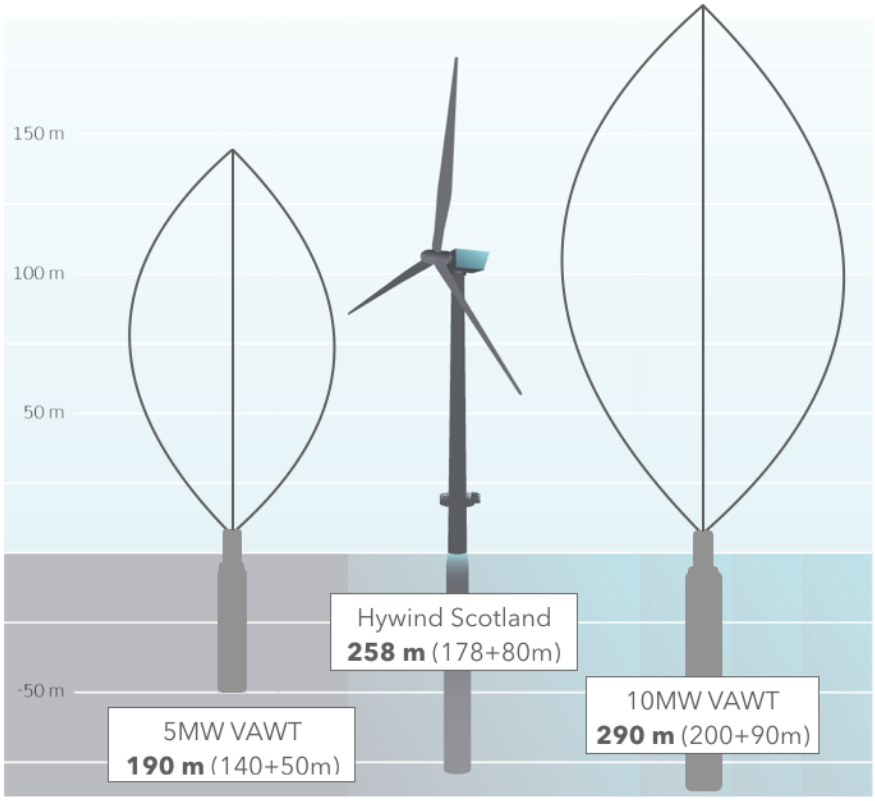

Figure 2.11: Final designs of the 5 & 10 MW FVAWTs, compared with Hywind [1]

Design	Parameter	Unit	5 MW VAWT	10 MW VAWT
Geometry	R	m	63.74	90.14
	H	m	129.56	183.23
	c	m	7.45	10.54
	L_{blade}	m	188.68	266.83
	N_{blade}	-	2	2
Structure	M_{blade}	kg	$1.54\ 10^5$	$4.36\ 10^5$
	M_{rotor}	kg	$3.08\ 10^5$	$8.71\ 10^5$
	$I_{xx,CG}$	kg.m^2	$5.25\ 10^8$	$2.97\ 10^9$
	$I_{yy,CG}$	kg.m^2	$1.11\ 10^9$	$6.28\ 10^9$
	$I_{zz,CG}$	kg.m^2	$5.89\ 10^8$	$3.33\ 10^9$
Aerodynamics	TSR^*	-	4.1	4.1
	C_P^*	-	0.455	0.455
	U_r	m.s^{-1}	12	12
	ω_r	rad.s^{-1}	0.656	0.464
Control	K_P	kg.m^2.s^{-1}	$2\ 10^8$	$8\ 10^8$
	K_I	kg.m^2.s^{-2}	$2\ 10^7$	$4\ 10^7$
	Q_{notch}	-	0.05	0.05

Table 2.3: Main parameters of the 5 & 10 MW VAWT optimized rotors

Design	Parameter	Unit	5 MW FVAWT	10 MW FVAWT
Geometry	d	m	50	90
	D_1	m	10.50	14.85
	D_2	m	15.17	19.95
	D_3	m	15.17	19.95
	D_4	m	10.41	13.69
	D_5	m	5.65	7.43
	h_1	m	1.40	1.98
	h_2	m	14.18	28.15
	h_3	m	22.42	47.87
	h_4	m	8	8
	$h_{5,1}$	m	4	4
	$h_{5,2}$	m	10	10
	Z_G	m	-33.5	-62.7
	Z_B	m	-28.2	-48.3
Structure	M_{steel}	kg	$1.00\ 10^6$	$3.39\ 10^6$
	M_{shaft}	kg	$1.54\ 10^5$	$4.59\ 10^5$
	M_{bal}	kg	$6.15\ 10^6$	$2.11\ 10^7$
	M_{gen}	kg	$9.00\ 10^4$	$2.54\ 10^5$
	$I_{steel,0}$	kg.m^2	$1.01\ 10^9$	$1.02\ 10^{10}$
	$I_{shaft,0}$	kg.m^2	$7.69\ 10^8$	$4.29\ 10^9$
	$I_{bal,0}$	kg.m^2	$1.06\ 10^{10}$	$1.15\ 10^{11}$
	$I_{gen,0}$	kg.m^2	$2.19\ 10^8$	$2.02\ 10^9$
Stiffness	C_{11}	N.m^{-1}	$6.06\ 10^4$	$1.05\ 10^5$
	C_{33}	N.m^{-1}	$2.52\ 10^5$	$4.36\ 10^5$
	C_{55}	N.m.rad^{-1}	$4.00\ 10^8$	$3.69\ 10^9$
	C_{66}	N.m.rad^{-1}	$1.40\ 10^7$	$4.07\ 10^7$
Damping	B_{66}	kg.m^2	$5.7\ 10^8$	$3.2\ 10^9$
	B_{33}	kg.m^{-1}	$7.0\ 10^4$	$1.4\ 10^5$
Periods	T_{11}	s	100.19	140.13
	T_{33}	s	34.89	48.72
	T_{55}	s	41.69	42.98
	T_{66}	s	24.49	34.87
	T_w	s	25	25
	T_{2P}	s	19.6	27.77
	T_{4P}	s	9.8	13.88

Table 2.4: Main parameters of the 5 & 10 MW FVAWT optimized spars

2.7 SIMO Implementation

This section presents the results from the SIMO implementation of the two models. In particular, the VAWTs were implemented as rigid bodies, neglecting elastic deformations of the blades and other components. The wave forces were modelled using Morison's equation, the aerodynamics part used DMS theory, and the mooring lines were modelled as linear stiffnesses.

SIMO solves the equations of motion for the two bodies, i.e. the rotor and its support platform. The various loads are taken into account, such as aerodynamic forces and torques, hydrodynamic forces, structural forces, control torque. The spar body was modeled using five slender rigid bodies, and their various properties were specified, such as added mass, damping, and distributed mass. The generator and ballast masses were included in the slender bodies, while the steel and shaft masses were modelled as structural masses, along with the various rotational inertias. Moreover, C_{33} and C_{55} were not given to SIMO, as it can compute the linear buoyancy variation of the slender bodies.

The spar hydrodynamic forces were modeled using Morison's equation, an empirical formula that gives the force per unit of length on a cylinder:

$$f_M = \rho\pi\frac{D^2}{4}\dot{u} + \rho C_A\pi\frac{D^2}{4}(\dot{u}-\dot{v}) + \frac{1}{2}\rho C_D D(\dot{u}-\dot{v})|\dot{u}-\dot{v}| \tag{2.39}$$

This formula, is valid for long waves $\lambda > 5D$ with D the diameter of the cylinder, and does not account for wave diffraction, unlike potential theory. However, it accounts for viscous drag (third term), added mass (second term) and Froude Krylov wave excitation force (first term). The quadratic coefficients are entered in SIMO for each slender body, using the formula $D_{q,2} = \frac{1}{2}\rho C_D D$ with $C_D = 0.7$.

The mooring lines were modelled in SIMO as linear stiffnesses in surge and yaw. The corresponding stiffness coefficients were computed using a frequency placement approach, in order to avoid resonance with the loads oscillating at the wave period and at the 2P and 4P periods. Moreover, the maximum mean thrust and vertical torque values were used to evaluate the maximal displacements, which should not exceed theoretically 15 m in surge and 90^o in yaw.

An engineering approach was used to design the damping values contained in Table 2.4 (B_{33} in heave and B_{66} in yaw). As shown in Fig. 2.12, a water brakes system was used as a yaw damper, as suggested by [4]. Specifically, three flat plates were positioned at a distance R_d from the longitudinal axis of the spar, leading to a quadratic damping in yaw:

$$B_{66} = \frac{3}{2}\rho_w A_d C_{D,d} R^3 \tag{2.40}$$

where $C_{D,d} = 1.28$ for a flate plate. For the 5 MW yaw damper, the value $R_d = 20$ m was taken, and a square with sides of 6 m gave an area of 36 m^2. For the 10 MW yaw damper, the damping values were scaled using dimensional upscaling. Using a similar method for the

heave damping, we obtain:

$$B_{33} = \frac{3}{2}\rho_w A_d C_{D,d} \tag{2.41}$$

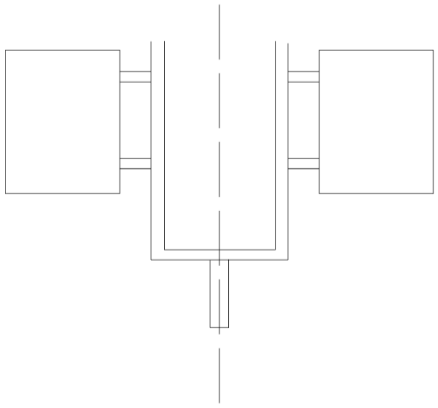

Figure 2.12: Water brakes system from [4]

Chapter 3: Results

This chapter present the various results from the SIMO analysis of the 5 & 10 MW FVAWTs. The first section presents the land-based results, essentially derived from constant wind tests. The second and third sections present the floating results, which include a preliminary dynamic analysis (*decay tests, regular wave tests*) and some power production results in various environmental conditions (*constand wind tests, wind and wave tests*). All results were post-treated using MATLAB: the mean and standard deviations of the key variables were plotted, and some spectral analysis were conducted too.

3.1 Land-Based VAWTs Analysis: 5 & 10 MW

3.1.1 Time Series: Constant Rated Wind Speed

Fig. 3.1 (a) & (b) present the 5 & 10 MW time series of the power signals, torques, rotor speed and rotor speed, under rated speed conditions (constant wind speed of 12 m/s). In both cases, similar observations can be made, in particular concerning the convergence of the electrical signals after a transient phase.

Between 0 and 40s, the reference rotational speed increases from 0 to its steady state value. In particular, the generator power and the electrical torque are negative, which means that the grid has to deliver some energy to start the rotation of the rotor. Then the generator power bewomes positive, as the wind aerodynamic torque grow stronger (plotted in blue). After this start-up phase, the filtering system is activated after 60s, and the electrical torque oscillations decrease. This is also the case for the generator power, which is equal to the rotor speed times the generator torque. Additionally, we observe the convergence of the electrical torque and power towards the rated aerodynamic torque and power respectively. Convergence of the rotor speed error towards zero, is also verified, and the rotor speed signal seems to converge towards the reference speed value.

While the electrical power and torque seem to converge, the aerodynamic power and torque signals (in blue) show some strong oscillations from 0 to a maximal value. The same observations can be made concerning the 10 MW results, with the exception that the oscillations of the aerodynamic torque seem to have a slightly longer period in the upscaled case.

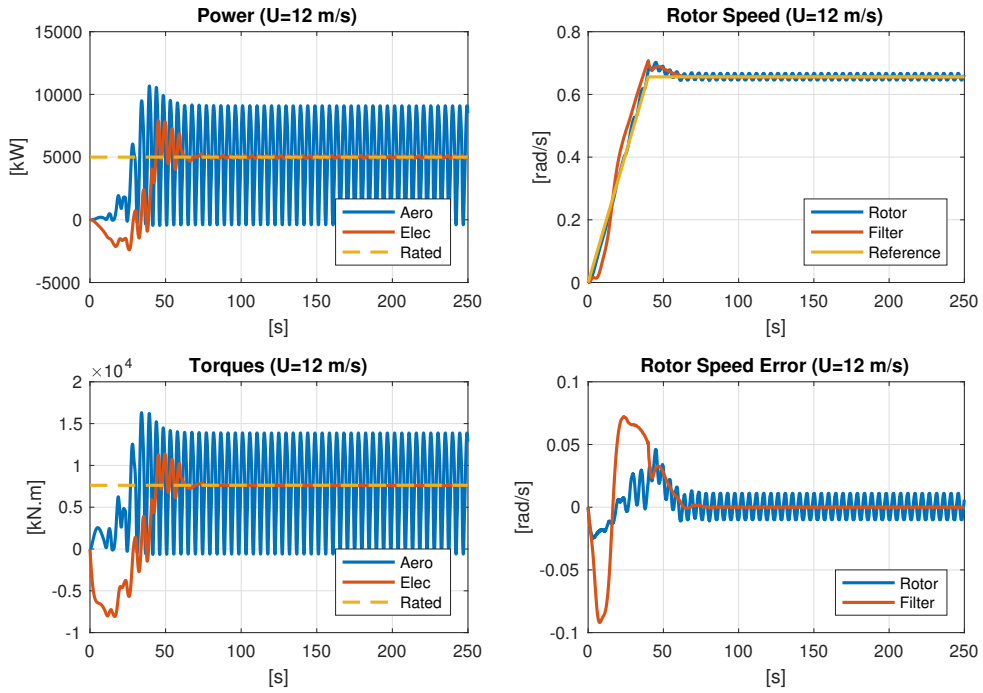

(a)

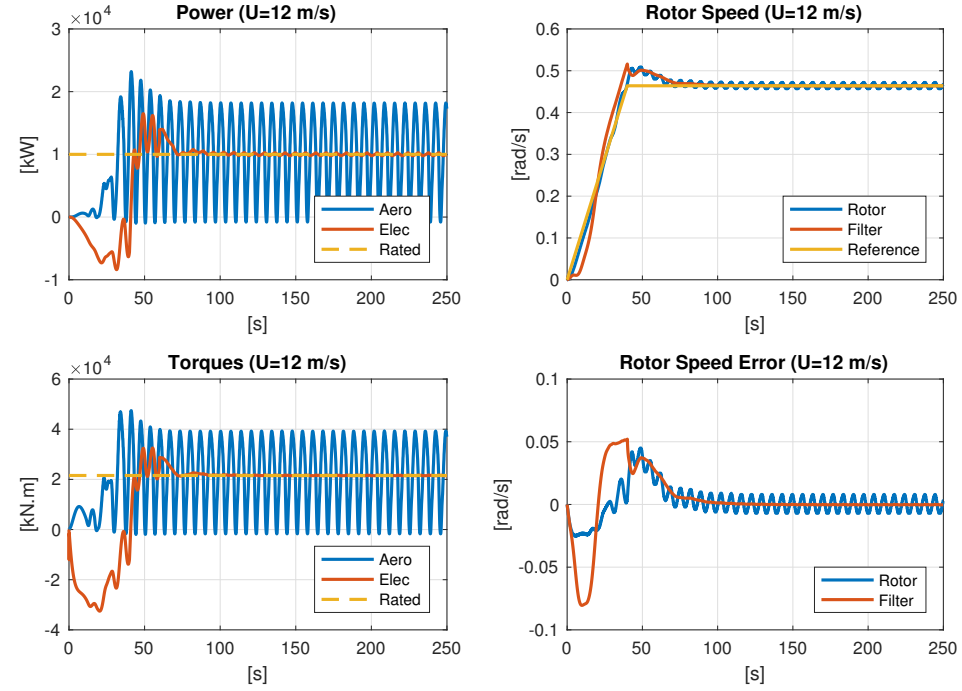

(b)

Figure 3.1: Time series of the (a) 5 MW VAWT & (b) 10 MW VAWT, at constant rated speed

3.1.2 Power Curves: Constant Wind

Fig. 3.2 depicts the mean values and standard deviations of various variables of the 5 & 10 MW land-based VAWTs, under constant wind conditions.

Below rated (i.e. for wind speeds smaller than 12 m/s), the mean generator power increases, while the TSR and the power coefficient are kept constant for the 5 & 10 MW cases (in blue and orange). Moreover, the TSR and power coefficient seem to have the same values as the optimal values identified in the aerodynamic method part ($C_P^* = 0.455$ for $TSR^* = 4.1$).

Above rated (i.e. for wind speeds greater than 12 m/s), the mean generator power is kept constant, while the power coefficient and the TSR decrease. It can also be noted that the mean rotor speed takes higher values in the 10 MW case, and that it has the same variations with the wind speed as the 5 MW case.

When comparing the constant wind curves with the 5 MW literature reference data [7], the present results show a smaller STD (standard deviation) of the generator power and a higher power coefficient, especially below rated (ancient value: 14 m/s). Furthermore, the 5 MW SIMO results show a higher mean rotor speed than the reference data.

Finally, the mean aerodynamic torque and thrust increase below rated, reach a local maximum at the rated speed (12 m/s), then decrease a bit and increase again (both for 5 & 10 MW). However the literature torque and thrust curves are only increasing with the wind speed.

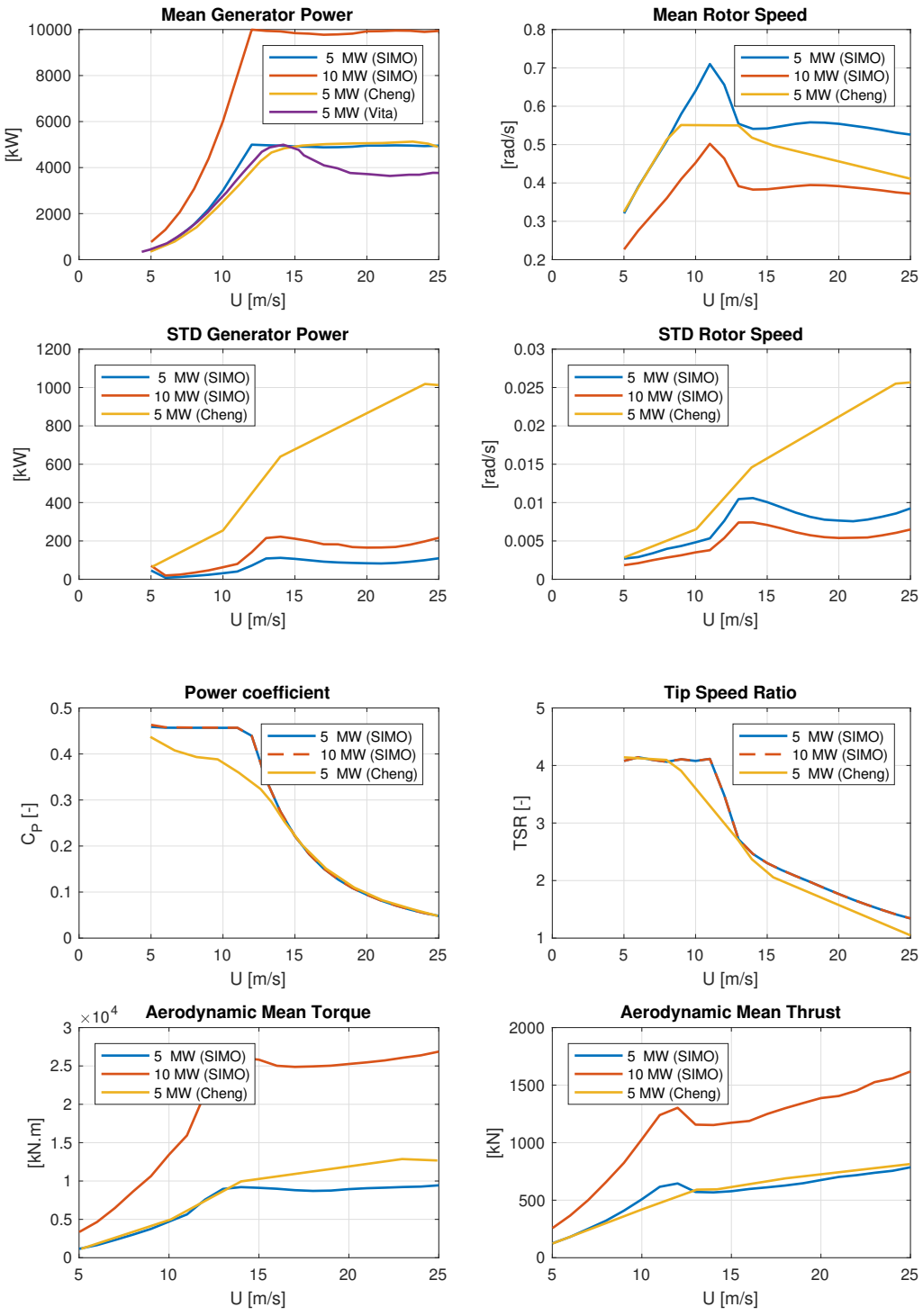

Figure 3.2: Constant wind results of the 5 & 10 MW VAWT compared with [7],[4]

3.1.3 Spectral Analysis: Constant Wind

Fig. 3.3 presents the spectral analysis of the land-based 5 MW VAWT key variables (*aerodynamic torque M_z, aerodynamic thrust F_x, rotor speed ω, filtered rotor speed ω_f, electrical torque T, generator power $\mathcal{P}_e$*) under the constant wind speed 25 m/s. The various spectral power densities are plotted against the rotational frequency in rad/s.

For the aerodynamic torque, two main peaks can be identified at 1.1 rad/s and 2.1 rad/s, corresponding to the 2P and 4P frequencies. The 25 m/s case was selected as it shows many harmonics, as third peak at 3.1 rad/s can be seen, corresponding to the 6P frequency (an even smaller peak can be observed more to the right, probably the 8P frequency). However, only the 2P frequency peak can be clearly identified on the aerodynamic thrust spectrum.

Additionally, the filtered rotor speed spectrum shows less intensity in its peaks compared with the rotor speed spectrum (three orders of magnitudes smaller on the y-axis). It appears that the 2P and 4P peaks have almost disappeared after filtering. As a remark, the spectrum of the generator rotational speed is not presented here, as it is simply equal to the gearbox ratio times the rotor speed.

The spectral content of the electrical torque signal looks very similar to the one of the filtered rotor speed, with peaks at the same frequencies and with similar shapes. The generator power spectrum also has the same spectral content, with peaks corresponging to 2P, 4P, 6P and 8P frequencies. However, the 2P and 4P peaks are much more visible for the generator power spectrum than for the electrical torque spectrum.

Similarly, Fig. 3.4 presents the spectral analysis of the land-based 10 MW VAWT key variables under the constant wind speed 25 m/s. The resulting spectras seem to be the same as for the 5 MW case, except that all peaks have been slightly shifted to the left and show an increased intensity in the 10 MW case.

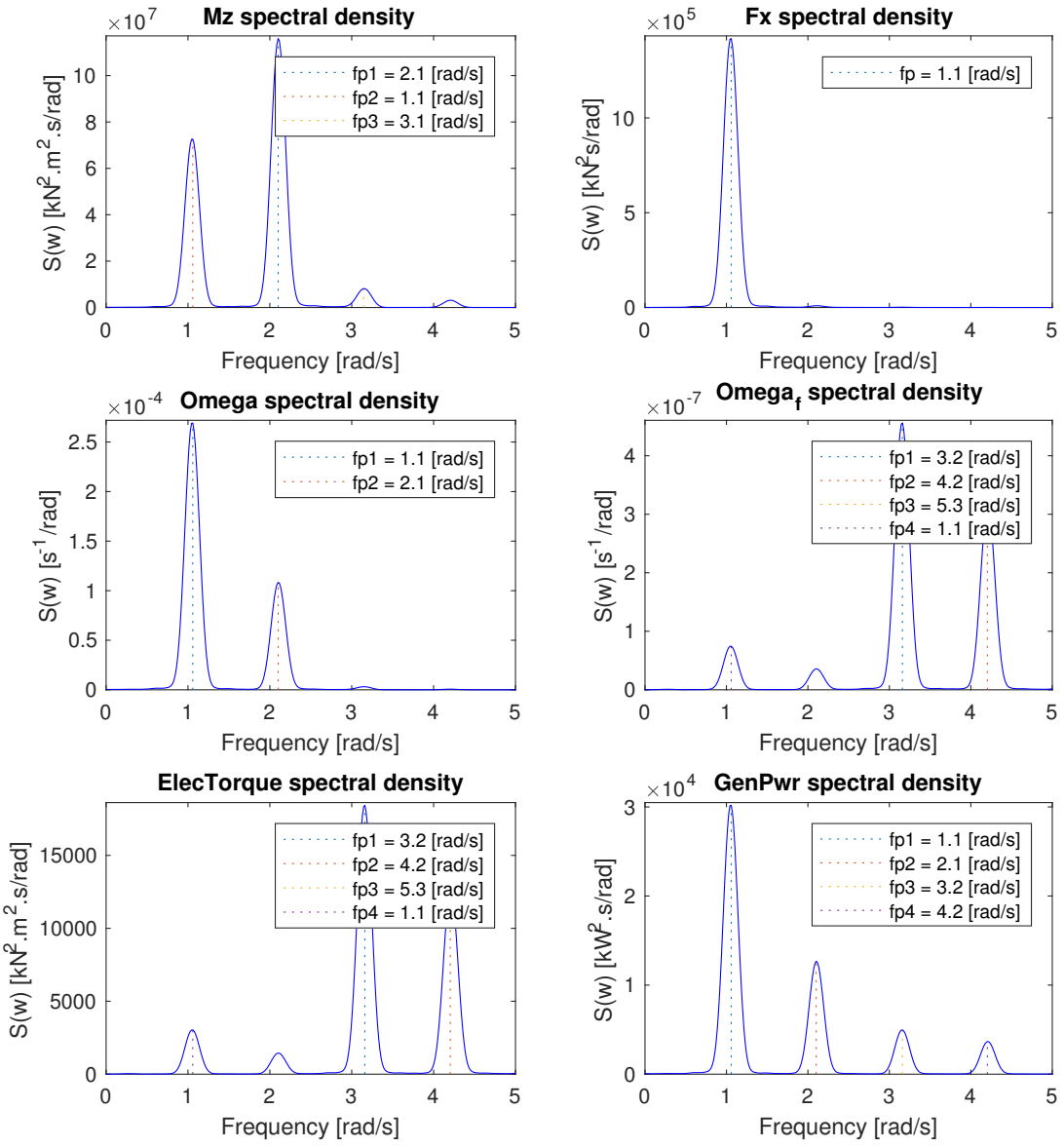

Figure 3.3: Spectral analysis of the land-based 5 MW VAWT for $U = 25$ m.s^{-1}

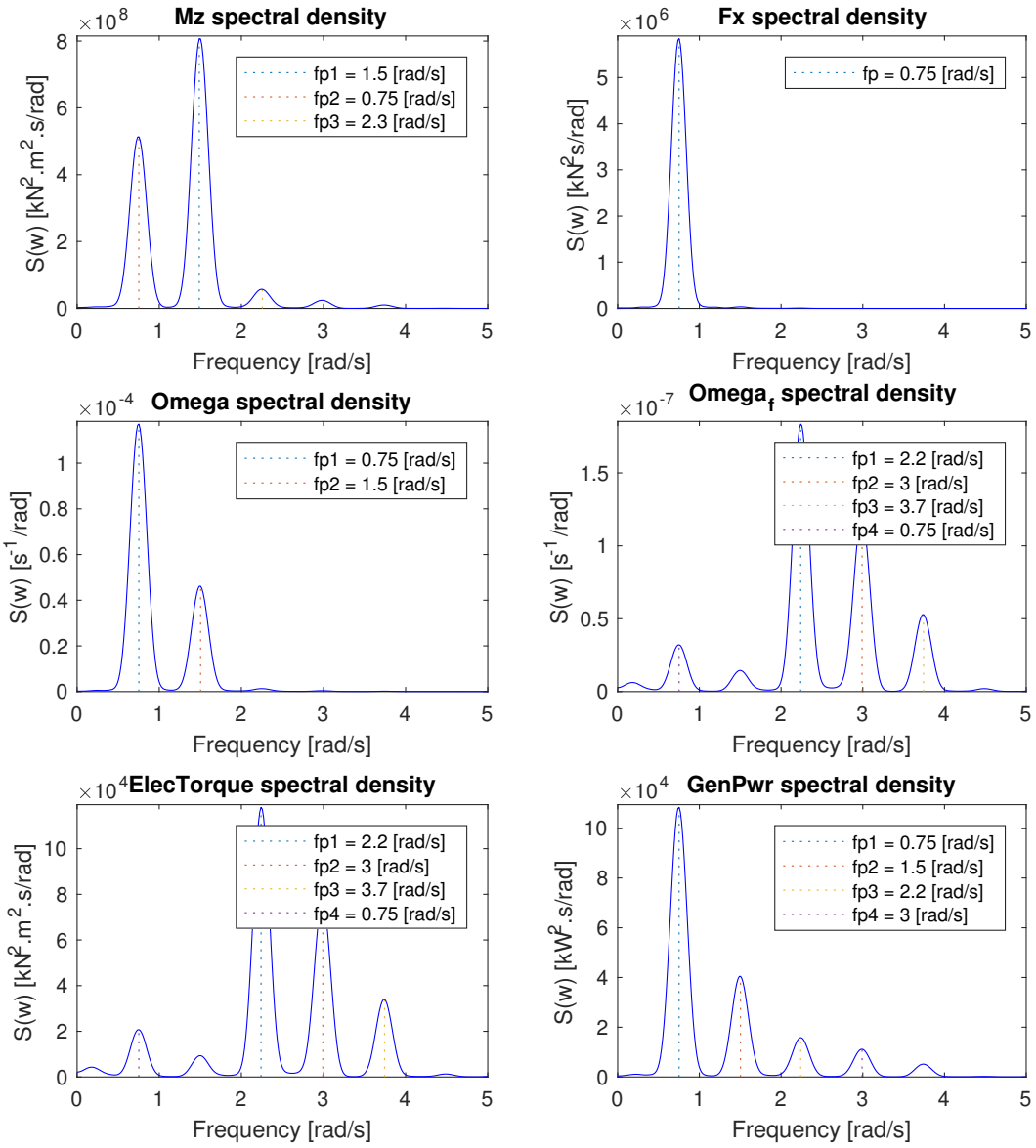

Figure 3.4: Spectral analysis of the land-based 10 MW VAWT for $U = 25$ m.s^{-1}

3.2 FVAWT Analysis: 5 MW

3.2.1 Structural Response

Decay Tests

Fig. 3.5 presents the time series of the decay tests of the 5 MW FVAWT, i.e. of the 5 MW VAWT mounted on its optimized spar. Four degrees of freedom (DOFs) were studied: surge, heave, pitch and yaw. For each DOF, an imposed load (force for surge and heave, torque for pitch and yaw) was applied to impose a static displacement (1 m in surge and heave, 10 degrees in pitch and yaw). In each case, the load was applied as a ramp between 50 s and 100 s, as a constant between 100 s and 200 s, and then relaxed after 200 s. The magnitude of each load was evaluated using the stiffness coefficient values from the design part, in order to obtain approximately the desired static displacements for the decay tests.

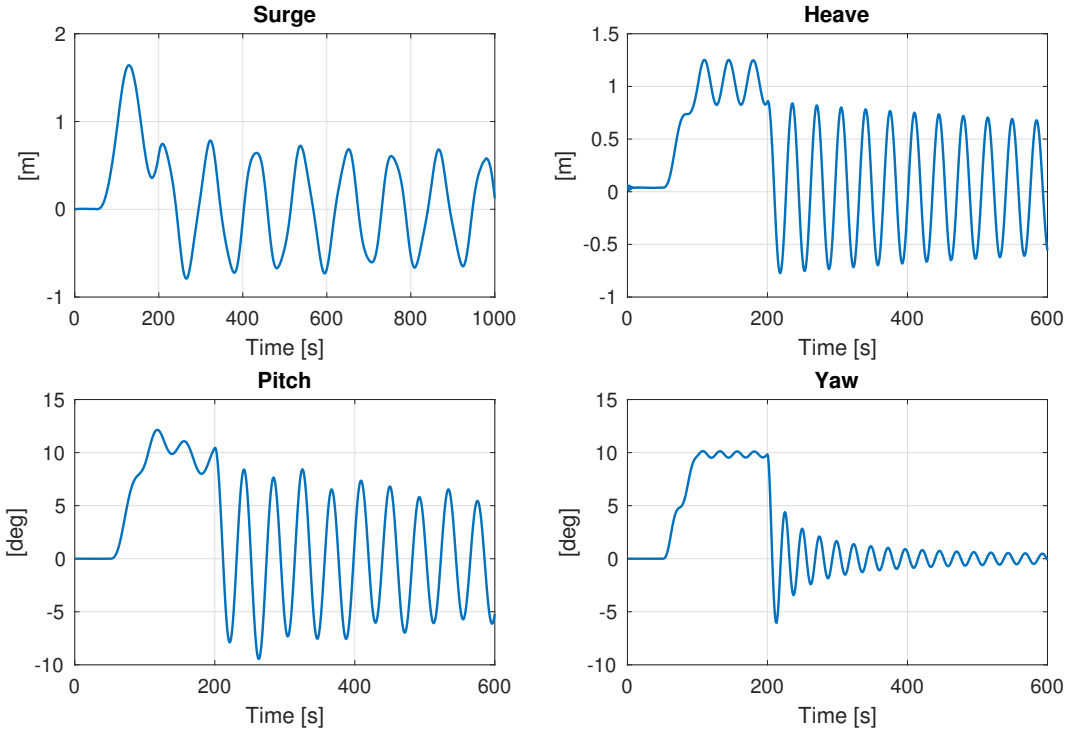

Figure 3.5: Time series of the decay tests of the 5 MW FVAWT

For each DOF, the decay period was evaluated by counting the time interval separating several maximal peaks, and dividing by the number of periods counted. Table 3.1 summarizes the resulting periods T and corresponding frequencies, computed as $\omega = \frac{2\pi}{T}$. Moreover, the relative errors of the eigenperiods were computed, taking as reference values the design periods from Table 2.4. As a result all errors were smaller than 1%, except for surge where a 9% error was found.

DOF	Surge	Heave	Pitch	Yaw
T [s]	109.7	34.9	41.6	24.5
ω [rad.s^{-1}]	0.057	0.18	0.15	0.26
ϵ [%]	9	0.04	0.2	0.03

Table 3.1: Periods, frequencies and errors from the 5 MW FVAWT decay tests

Irregular Wave Tests

Some wave only tests were conducted in SIMO for various sea states, detailed later in Table 3.2. Each test was run during 1800 seconds (half an hour) with no wind, in order to analyze the statistical response of the 5 MW FVAWT in irregular waves. Fig. 3.6 presents the spectral analysis of the various DOFs of the FVAWT under the following environmental conditions: $U = 0$ m/s, $H_s = 5.75$ m, $T_p = 10.75$ m (i.e. $\omega_p = 0.58$ rad/s). The studied DOFs are surge, heave, pitch, yaw, and the hub position coordinates in the horizontal plane (X_G,Y_G). For each spectrum, the spectral densities were plotted against the frequency and the main peak frequencies were identified using the WAFO numerical tool in MATLAB.

The peak frequencies observed in the spectra from Fig. 3.6 can be compared with the decay tests eigenfrequencies from Table 1.1 and the wave peak frequency of the sea state ($\omega_p = 0.58$ rad/s). Overall the spectral peak frequencies match well with these reference values and are detailed as follows. For the surge spectrum, three peak frequencies are observed, matching respectively with the surge, pitch and wave frequencies. In the heave spectrum, two peak frequencies are observed, corresponding to the wave and heave frequencies. For the pitch spectrum two peak frequencies are observed, corresponding to the pitch and wave frequencies. For the yaw spectrum, one peak frequency is observed corresponding to the yaw frequency. For the hum coordinates spectra, the pitch, wave and surge frequencies can be observed in the X_G spectrum, while only the pitch frequency can be observed in the Y_G spectrum.

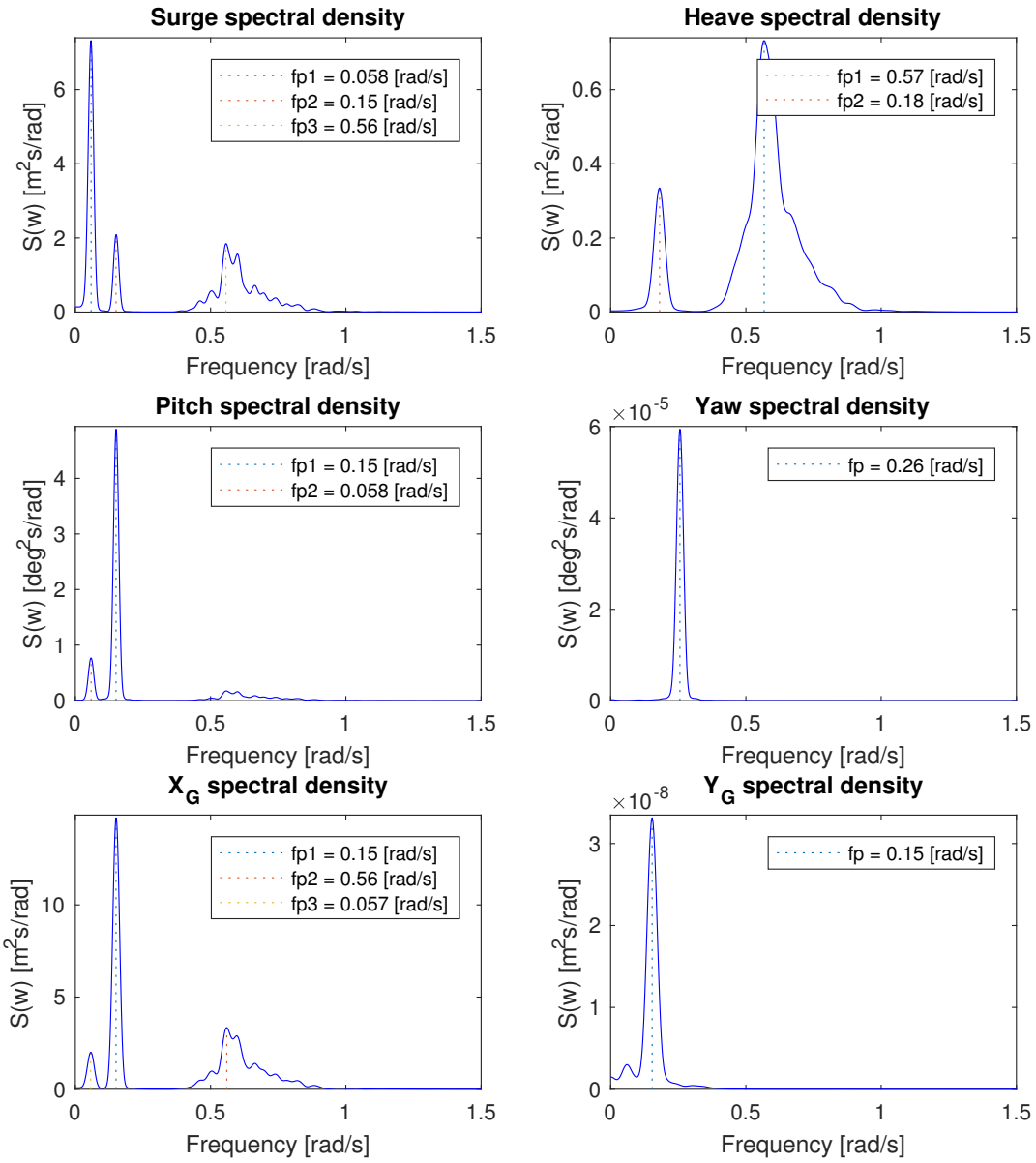

Figure 3.6: Spectral analysis of the DOFs of the 5 MW FVAWT for the wave only tests

3.2.2 Power Production

This subsection presents the electrical and aerodynamic results of the 5 MW FVAWT in power production conditions, i.e. under constant wind and wind & waves.

Time Series: Constant Rated Wind Speed

Fig. 3.7 shows the time series of the power, torques and rotor speed of the 5 MW FVAWT at constant rated wind speed (12 m/s). Similar observations can be made as for Fig. 3.1 (a), in particular convergence is observed for the electrical variables towards their respective rated or reference values.

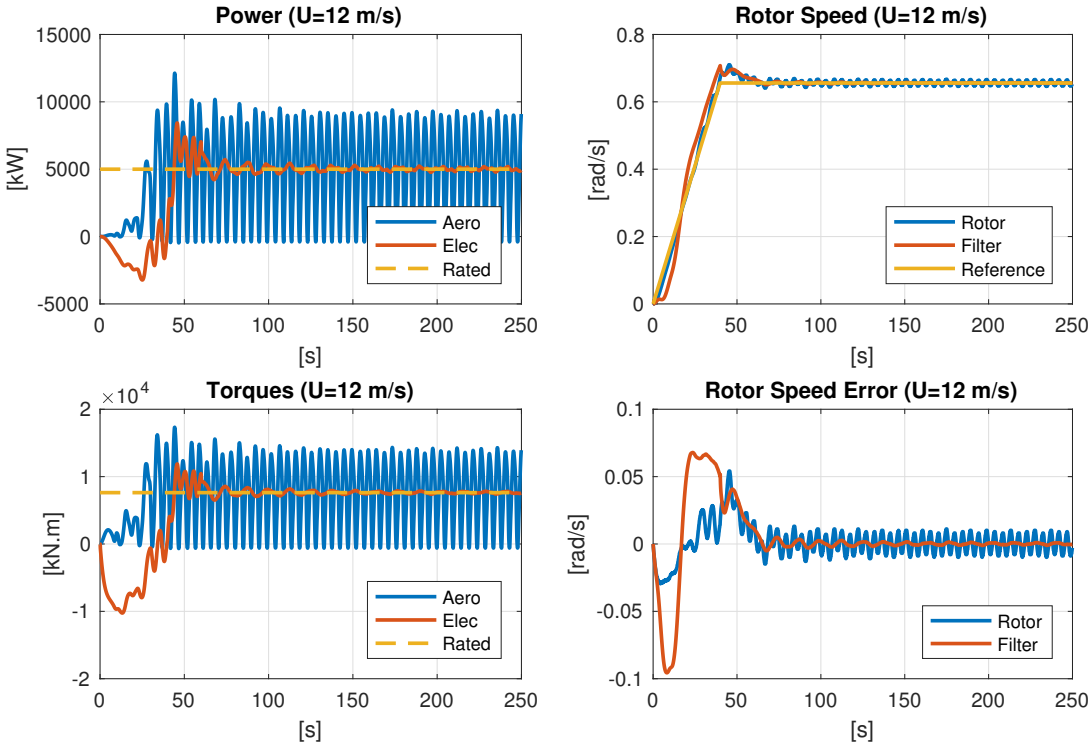

Figure 3.7: Time series of the 5 MW FVAWT at constant rated speed

Power Curves: Wind Only and Wind & Waves

In order to perform constant wind and wind & wave tests, some values had to be selected for the wind speed U, the significant wave height H_s and the wave peak period T_p. In order to model some realistic conditions, some correlated environmental sets were defined using data from joint distributions of wind and wave in the north sea [30]. Table 3.2 summarizes the correlated environmental data sets. Linear interpolation was used between two points of the (U,H_s,T_p) 3D space, corresponding to 5 and 25 m/s. These two points were selected inside the contour surface of the joint distribution (contour defined for a 100 year return period).

U [m/s]	5	6	7	8	9	10	11	12	13	14	15
H_s [m]	5	5.25	5.5	5.75	6	6.25	6.5	6.75	7	7.25	7.5
T_p [s]	10	10.25	10.5	10.75	11	11.25	11.5	11.75	12	12.25	12.5
U [m/s]	16	17	18	19	20	21	22	23	24	25	
H_s [m]	7.75	8	8.25	8.5	8.75	9	9.25	9.5	9.75	10	
T_p [s]	12.75	13	13.25	13.5	13.75	14	14.25	14.5	14.75	15	

Table 3.2: Environmental correlated data set (U,H_s,T_p)

Fig. 1.8 and Fig. 1.9 present the mean and standard deviation (STV) values of the main variables of the FVAWT in power production condition, comparing the floating wind only and floating wind & wave results with the land-based results. The mean values of all variables seem to be the same in wind only, wind & waves, and land-based conditions (except for the Y aerodyanmic torque in wind & wave conditions).

However the STD of the certain variables (generator power, generator torque, filtered rotor speed, rotor speed) seems to take higher values for the wind & wave case than for the wind only case. Otherwise the STD values in land-based and floating wind only conditions seem very similar, although the rotational speed STD seems a bit smaller for the floating wind only case.

Moreover, the mean value of the generator power seems higher for the SIMO results than for the reference results [7], especially close to the new rated wind speed (12 m/s). The generator power STD appears to be smaller for the floating wind only case than for the reference results, although the generator power STD is higher in the wind & wave case than for the published results under rated wind speed.

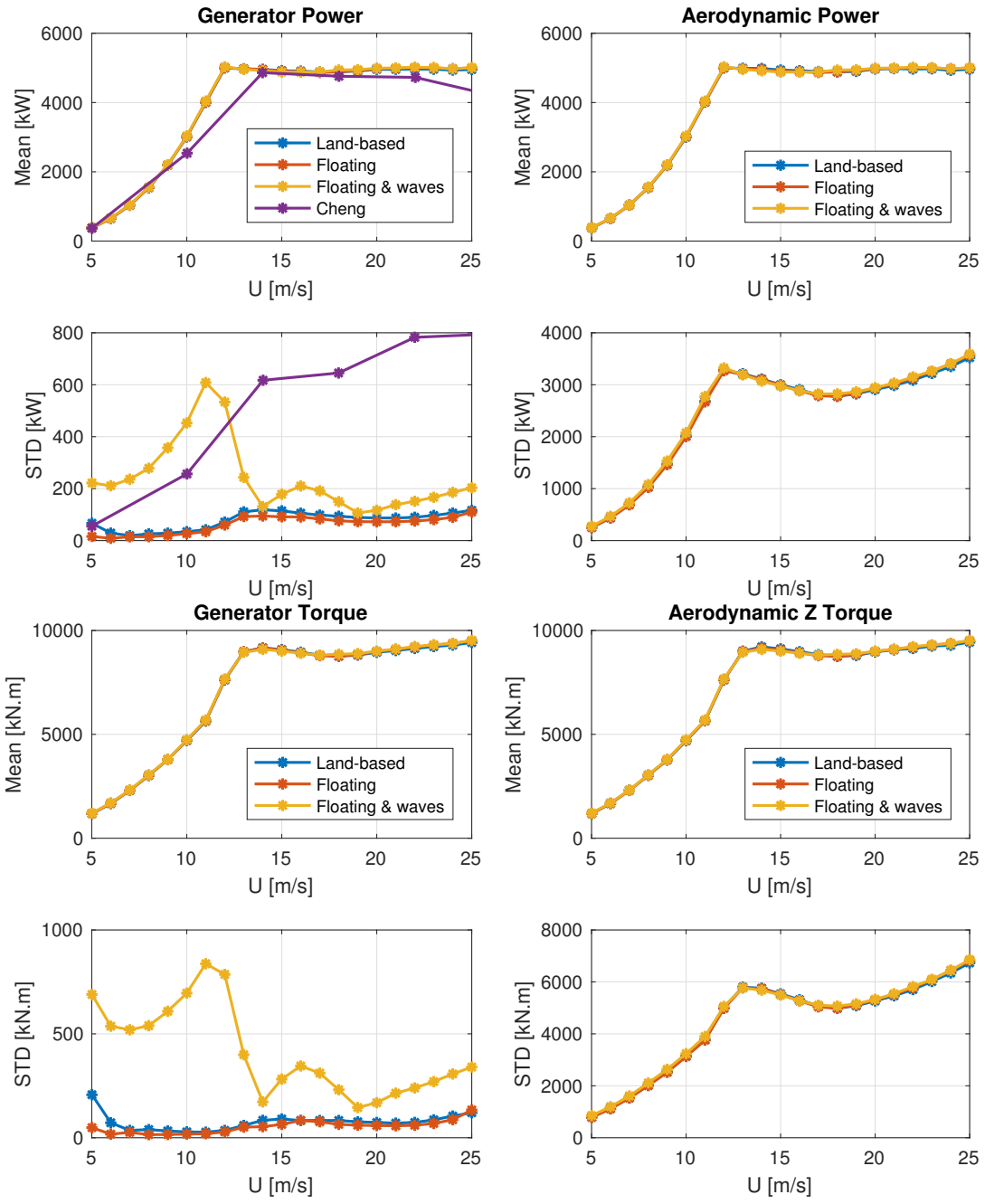

Figure 3.8: Mean and standard deviation of the 5 MW FVAWT dynamic variables (generator power, generator torque, aerodynamic power, aerodynamic Z-axis torque), under constant wind and wind & waves conditions (comparison with land-based results and [7])

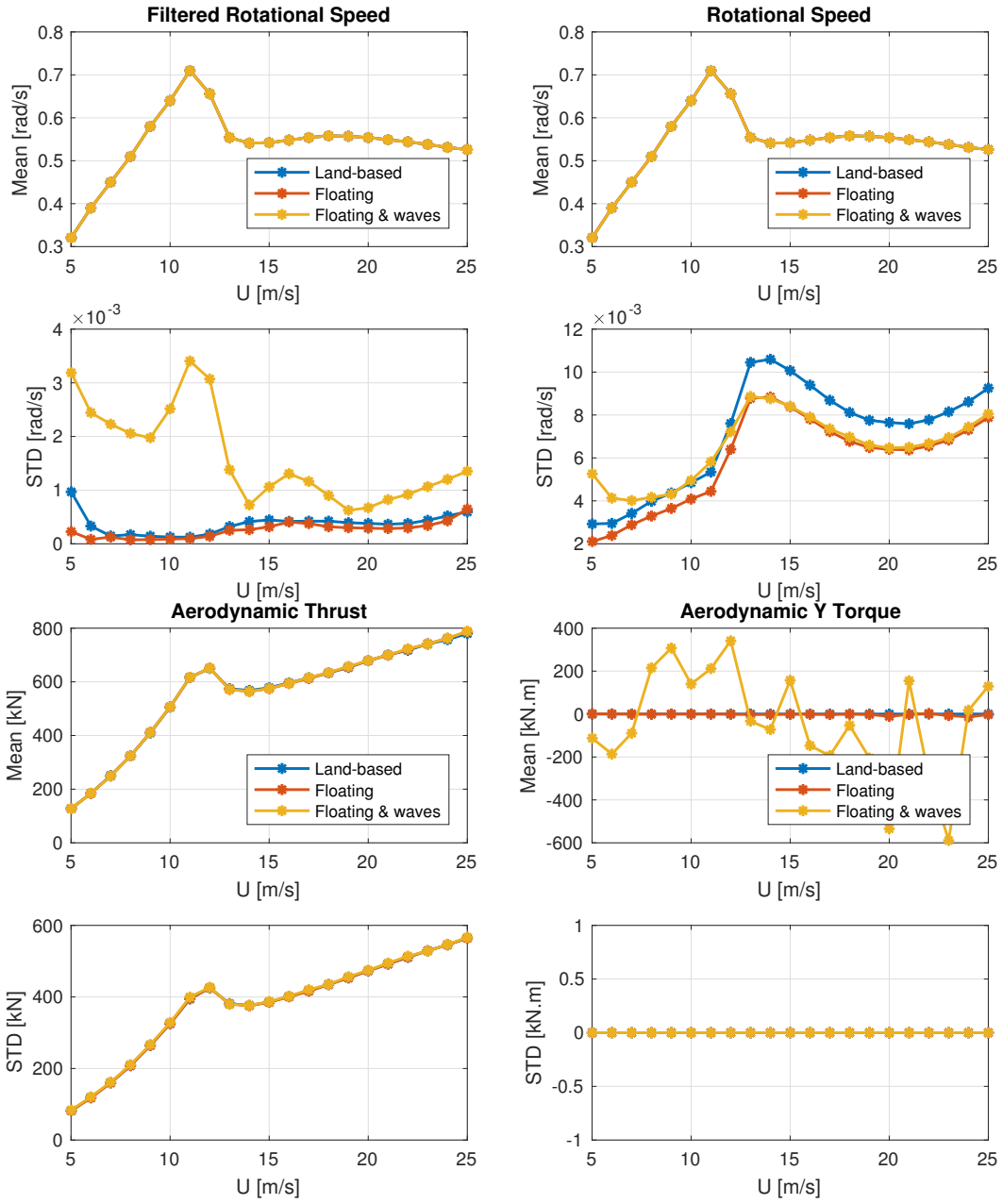

Figure 3.9: Mean and standard deviation of the 5 MW FVAWT dynamic variables (filtered rotational speed, rotational speer, aerodynamic thrust, aerodyanmics Y-axis torque), under constant wind and wind & waves conditions (land-based results are also included for comparison purposes)

Spectral Analysis: Wind Only and Wind & Waves

Fig. 3.10 depicts the spectral analysis results of the floating wind only and the floating wind & wave cases, compared with the land-based case. While the constant wind speed $U = 25$ m/s was applied in all cases, the corresponding correlated condition set from Table 3.2 was applied for the wind & wave case.

Overall the spectral density signals are very much alike in all three cases for the aerodynamic torque M_z, the aerodynamic thrust F_x, and for the rotor speed ω. Indeed, the spectral peaks are observed at the same frequencies, and with intensities that are almost the same in the three compared cases for M_z, F_x and ω.

However, a new peak appears in the floating cases for the filtered rotor speed ω_f, the electrical torque T, and the generator power $\mathcal{P}_e$. This new peak appears at a low frequency, smaller than 0.3 rad/s. The intensity of this peak is higher in the wind & wave case than in the wind-only case. The same peak is barely visible on the left of the rotor speed spectrum, only for the the wind & wave case.

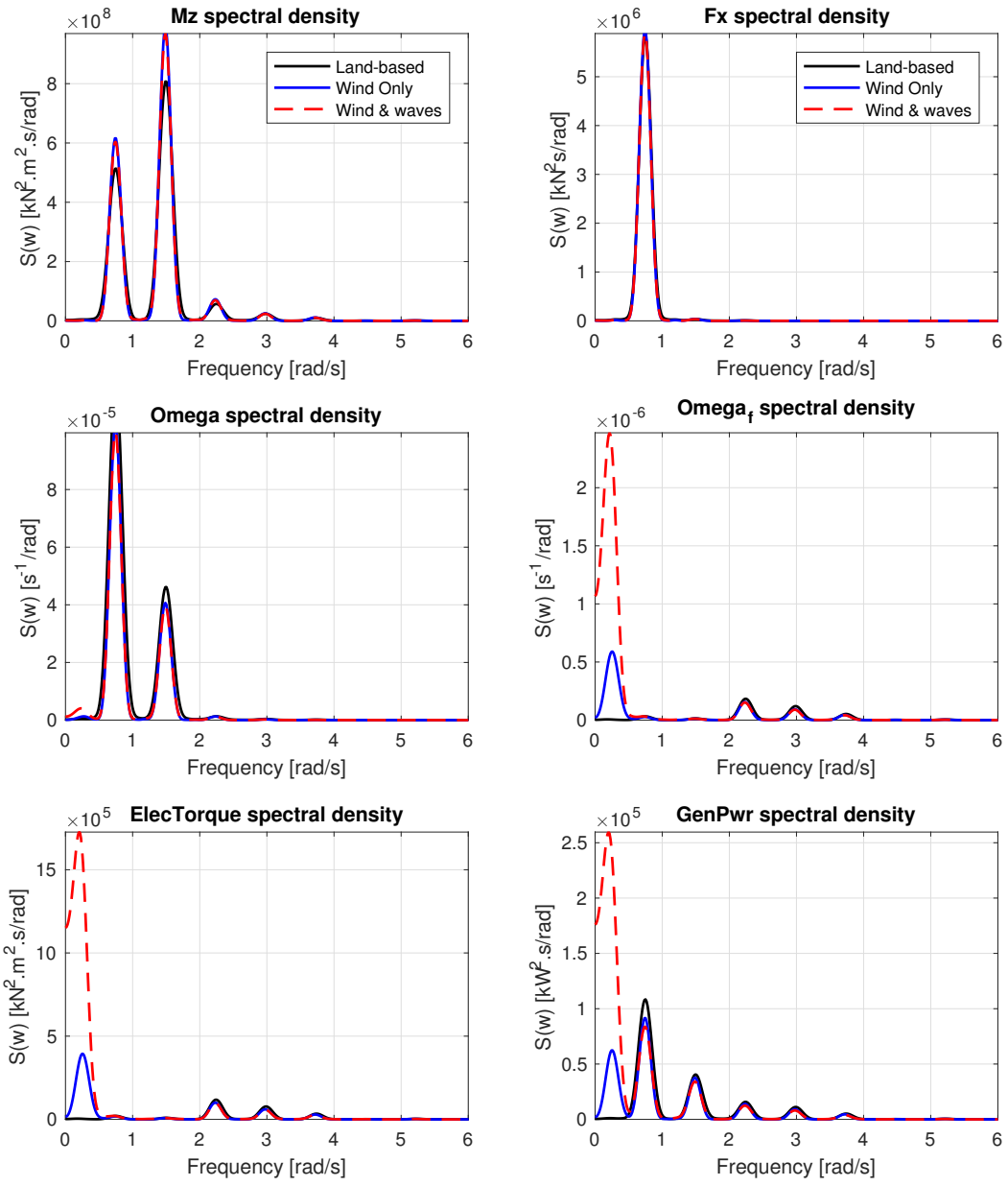

Figure 3.10: Spectral analysis of the 5 MW FVAWT production variables under constant wind and wind & waves ($U = 25$ m.s^{-1}, also compared with land-based spectra)

3.2.3 DOFs Analysis

Mean DOF Motions

Fig. 3.11 and Fig. 3.12 present the mean values and the standard deviations of the various DOFs of the 5 MW FVAWT, for three cases: wind only, wind & waves, waves only. The hub plane coordinates X_G and Y_G are plotted in Fig. 3.11, while surge, heave, pitch and yaw are plotted in Fig. 3.12.

The mean values in surge, heave, X_G and Y_G are quite low as they are all smaller than 0.15 m. However, the corresponding STDs can reach 2 m in surge, more than 1 m in heave, almost 3 m for X_G and less than 2 m for Y_G. These trends are observed in all three studied environmental conditions, although the wind & waves case seems to give slightly higher mean and STD values than the other cases.

The mean pitch angle is smaller than 0.02 degrees in all cases, and the corresponding STD is smaller than 0.8 degrees, which is very small. Moreover, the mean yaw angle is increasing with the wind speed and smaller than 40 degrees in all cases (it is even zero in the waves only case). The STD in yaw is smaller than 2 degrees for the wind only and waves only cases, while it is smaller than 8 degrees for the wind & waves case.

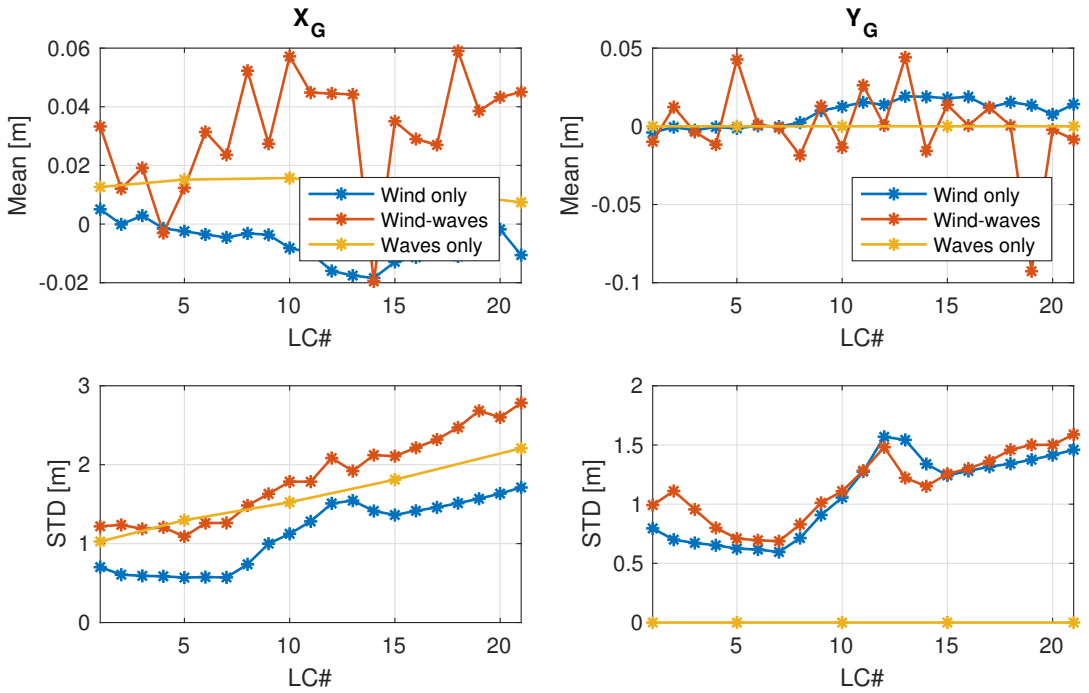

Figure 3.11: Mean values and standard deviations of the plane coordinates of the 5 MW FVAWT hub

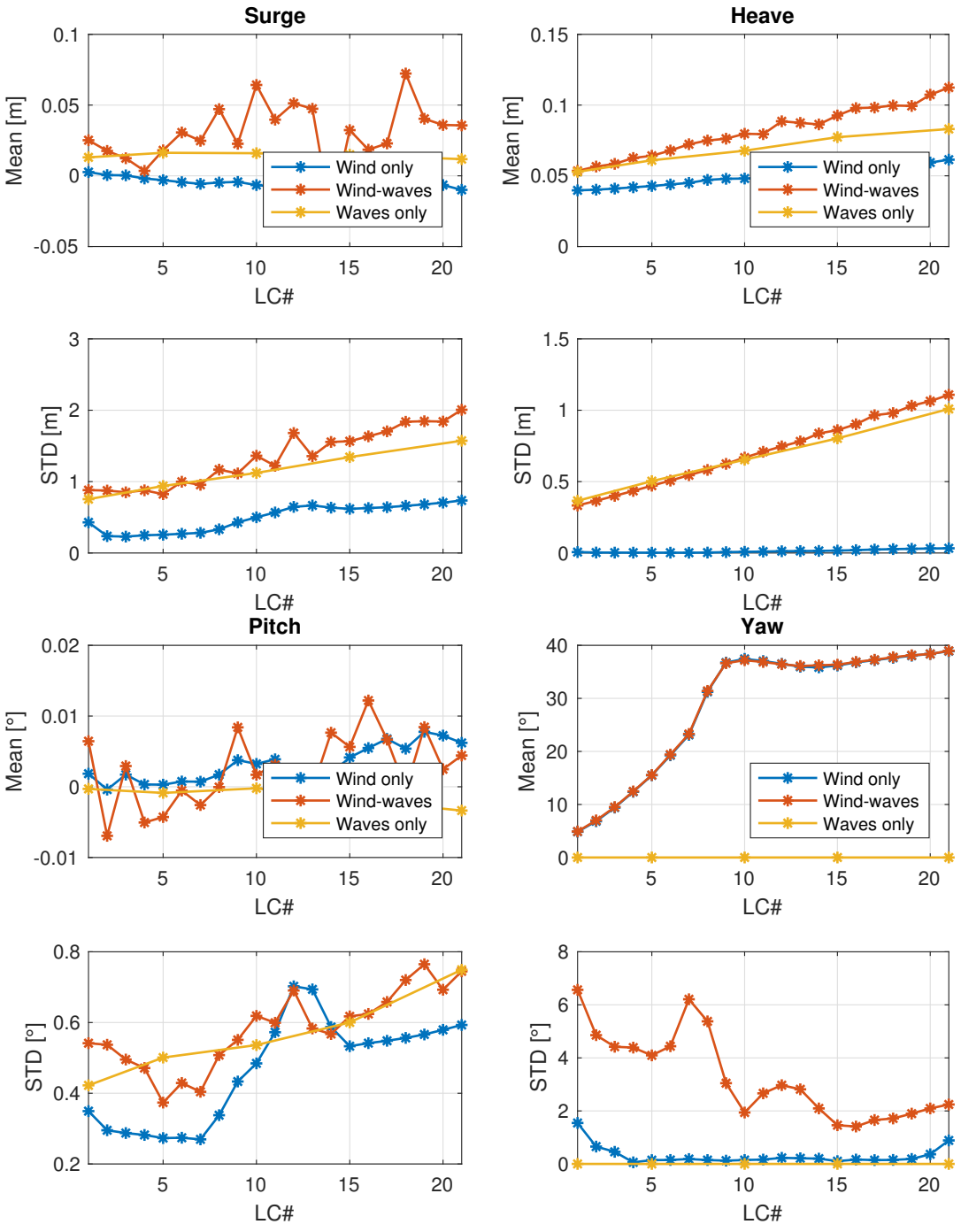

Figure 3.12: Mean values and standard deviations of the 5 MW FVAWT DOFs (surge, heave, pitch, yaw)

Spectral Analysis: DOF Motions

Fig. 3.13 presents the spectral analysis of the various DOFs under constant wind and wind & waves conditions, for the constant wind speed $U = 8$ m/s and its corresponding correlated environmental set (Table 3.2). These results are plotted with the waves only case spectra, previously presented in Fig. 3.6.

A few comment can be made about the wind only case to begin with. The pitch eigenfrequency (0.15 rad/s) seems to have disappeared from all blue spectra. However, a new peak is appearing at a frequency close to 0.5 rad/s for the surge, pitch, X_G and Y_G spectra. This new peak frequency is not observed in heave and yaw though, where the eigenfrequency peaks are still present (respectively 0.18 rad/s and 0.26 rad/s from Table 3.1).

Some mixed observations can be made concerning the wind & wave case, combining certain properties of the wind only case and the waves only case. For instance, the wind & waves spectra seem to possess all the peaks from the waves only spectra in surge, pitch and X_G. Additionally, a new peak is observed at a frequency a bit higher than 0.3 rad/s, in surge, pitch, X_G and Y_G, which reminds of the new peak observed in the wind only spectra, except that this new peak frequency is smaller in the wind & wave case.

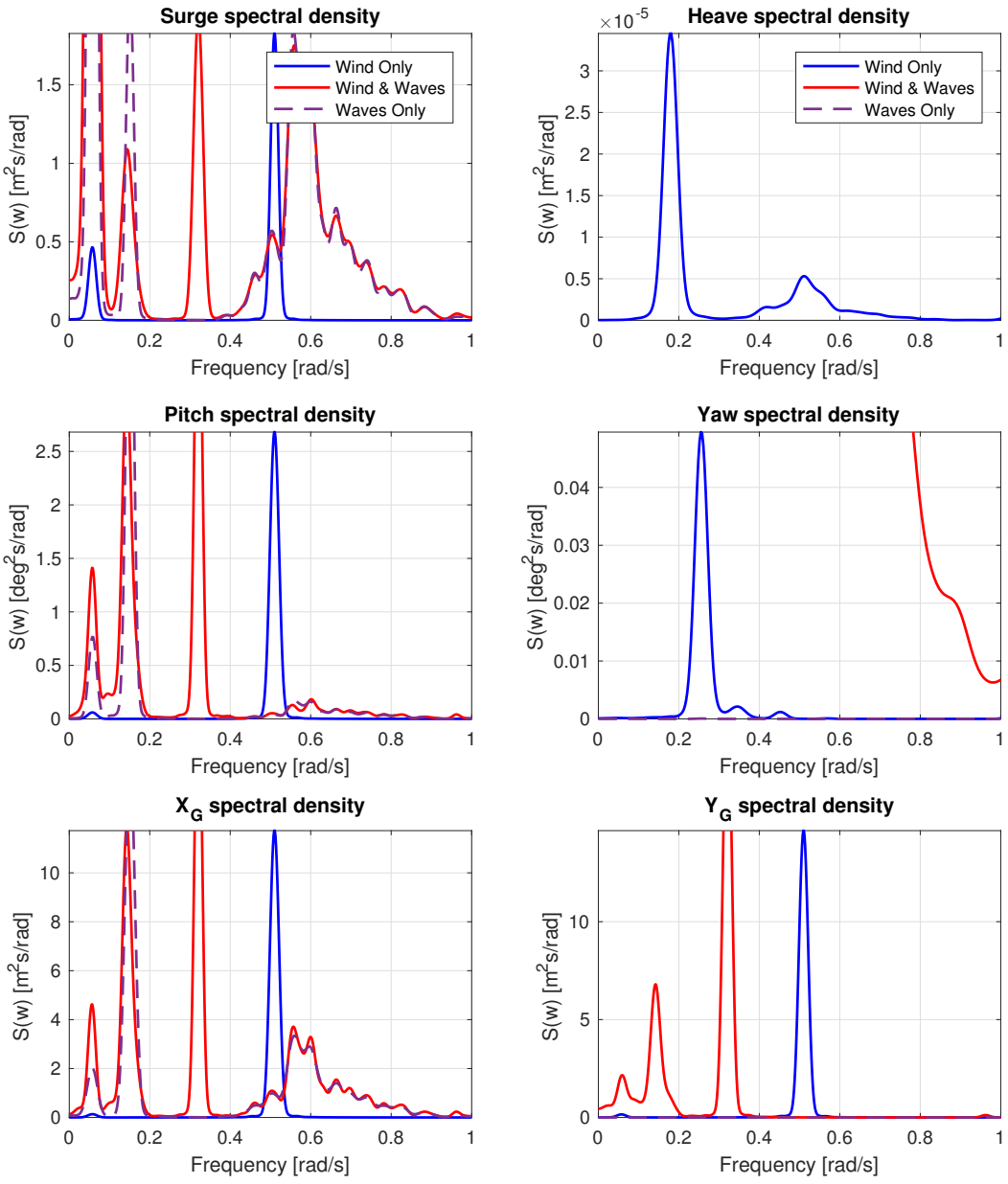

Figure 3.13: Spectral analysis of the 5 MW FVAWT DOFs for $U = 8$ m.s^{-1} under constant wind, wind & waves, and waves only

Hub Plane Trajectories

Fig. 3.14 shows the rotor hub plane trajectories for three conditions: wind only, wind & waves, and waves only (as in Fig. 3.13). In the wind only case, a circular trajectory can be neatly observed, with a diameter of approximately 2 meters. However, this trajectory pattern is lost when irregular waves are added to the constant wind, and the resulting trajectory is barely contained in the 4 by 4 square centered in the origin of the coordinate system. Finally in the waves only case, which are generated in the X direction, the hub seems to oscillate on the X axis from -3 m to almost 4 m, and does not seem to move in the Y direction.

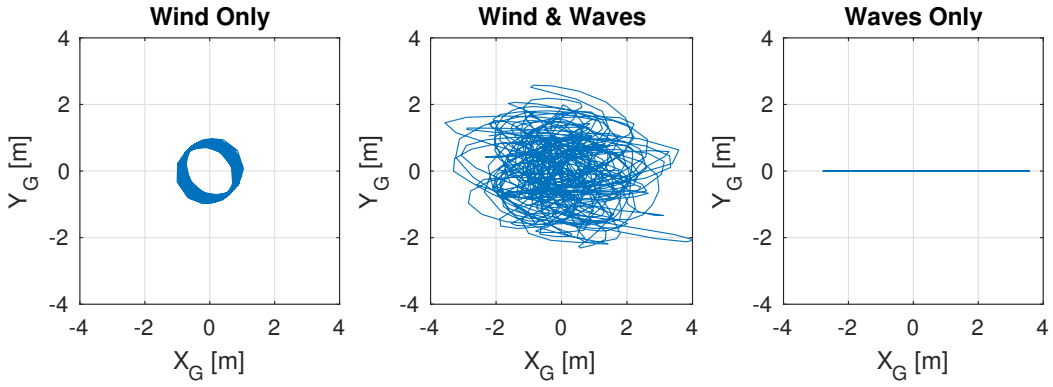

Figure 3.14: Hub trajectory in the (X,Y) plane for the 5 MW FVAWT ($U = 8$ m.s^{-1})

3.3 FVAWT Analysis: 10 MW

This section presents the structural response and the power production results of the 10 MW FVAWT. The DOF analysis is available in the appendix, as the results are overall very similar to the 5 MW case.

3.3.1 Structural Response

Decay Tests

Fig. 1.15 presents the time series of the 10 MW FVAWT decay tests. The same methodology as for the 5 MW FVAWT was used to determine the eigenfrequencies and the corresponding errors in surge, heave, pitch and yaw. Table 3.3 summarizes the DOF eigenfrequencies and eigenperiods from the decay tests. All errors relative to the theoretical period values are smaller than 1%, except for surge which has a 11% error.

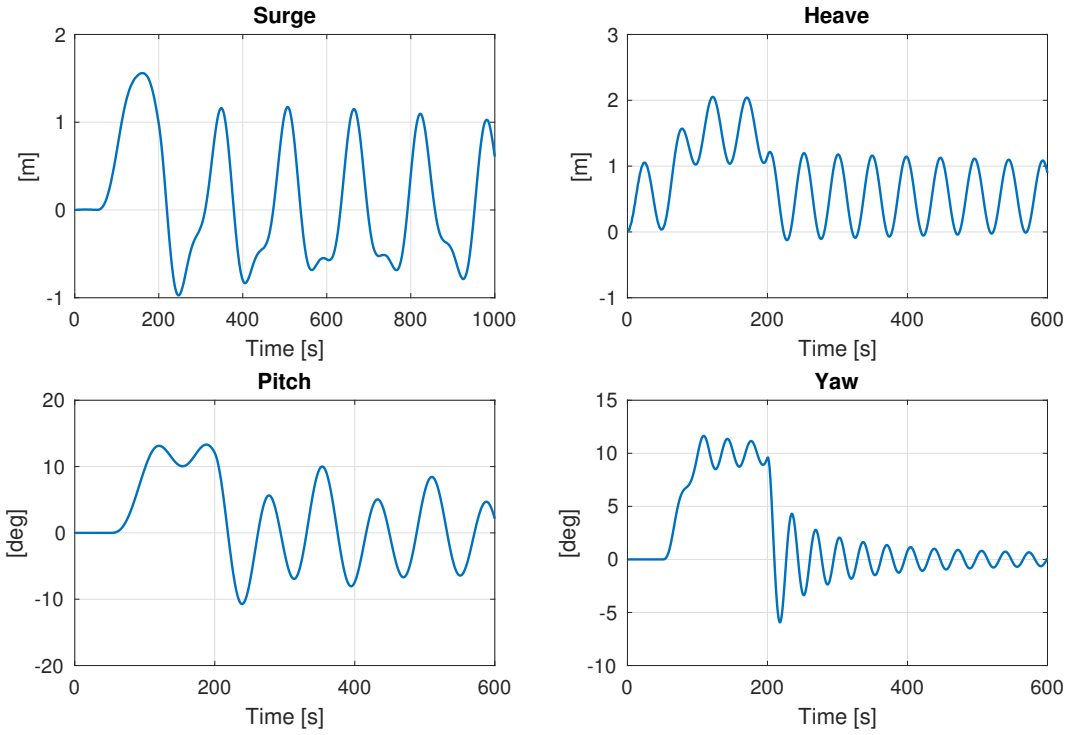

Figure 3.15: Time series of the decay tests of the 10 MW FVAWT

DOF	Surge	Heave	Pitch	Yaw
T [s]	158	48.7	77.8	33.9
ω [rad.s^{-1}]	0.04	0.13	0.08	0.19
ϵ [%]	11	0.04	0.5	0.4

Table 3.3: Periods, frequencies and errors from the 10 MW FVAWT decay tests

Waves Only Tests

Fig. 3.16 presents the DOF spectra of the 10 MW FVAWT in irregular waves condition: U = 0 m/s, H_s = 5.75 m, T_p = 10.75 m (i.e. ω_p = 0.58 rad/s). The various spectra can be compared with the decay tests results, as done for the 5 MW results.

The wave peak frequency of 0.58 rad/s is visible on the spectra in surge, heave, and X_G. Using the values from Table 3.3, the surge eigenfrequency of 0.04 rad/s correspond to the lowest peak in the surge spectrum, while the 0.08 rad/s pitch eigenfrequency is identified in the surge, pitch, X_G and Y_G spectra. The 0.19 rad/s yaw eigenfrequency is present in the yaw spectrum, and the 0.13 rad/s heave eigenfrequency is present in the heave spectrum.

As a remark, this preliminary dynamic analysis of the 10 MW FVAWT does not point out any specific issue. In particular, the structural frequencies are not overlapping with the wave excitation frequency. The global stability of the floating structure remains to be checked in wind conditions, when the VAWT is operational.

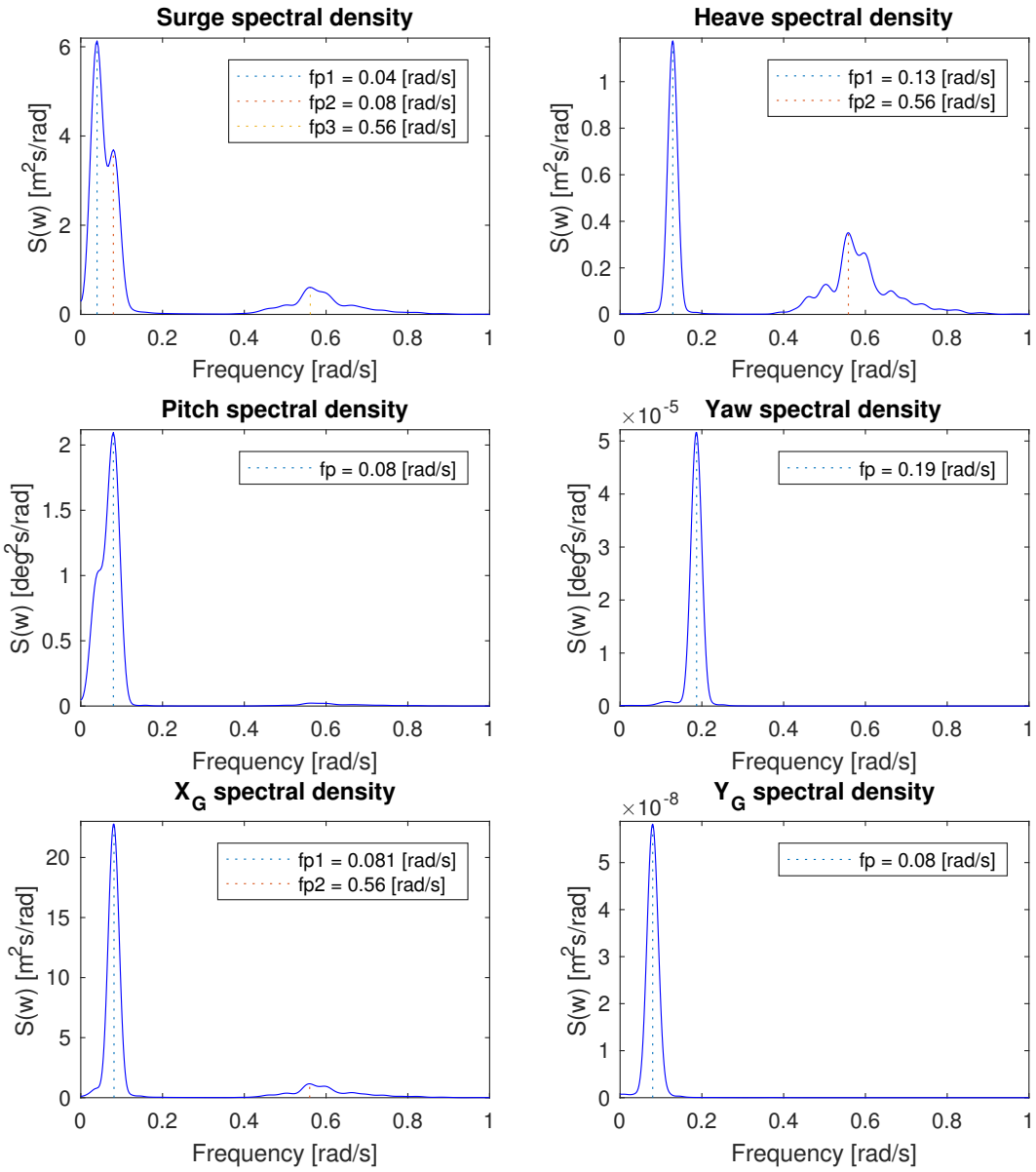

Figure 3.16: Spectral analysis of the DOFs of the 10 MW FVAWT for the wave only tests

3.3.2 Power Production

Time Series: Constant Rated Wind Speed

Fig. 3.17 presents the time series of the 10 MW FVAWT under constant rated wind speed (12 m/s). The generator power converges to its rated value (10 MW) after 100s, although it still shows some small oscillations. The filtered rotor speed error converges to 0 also after 100s, although the rotor speed error presents some small oscillations. The aerodynamic power and torque start from 0 and oscillate more and more as the rotor speed increases, until the transient phase is over and the oscillations of the same physical variables become periodical.

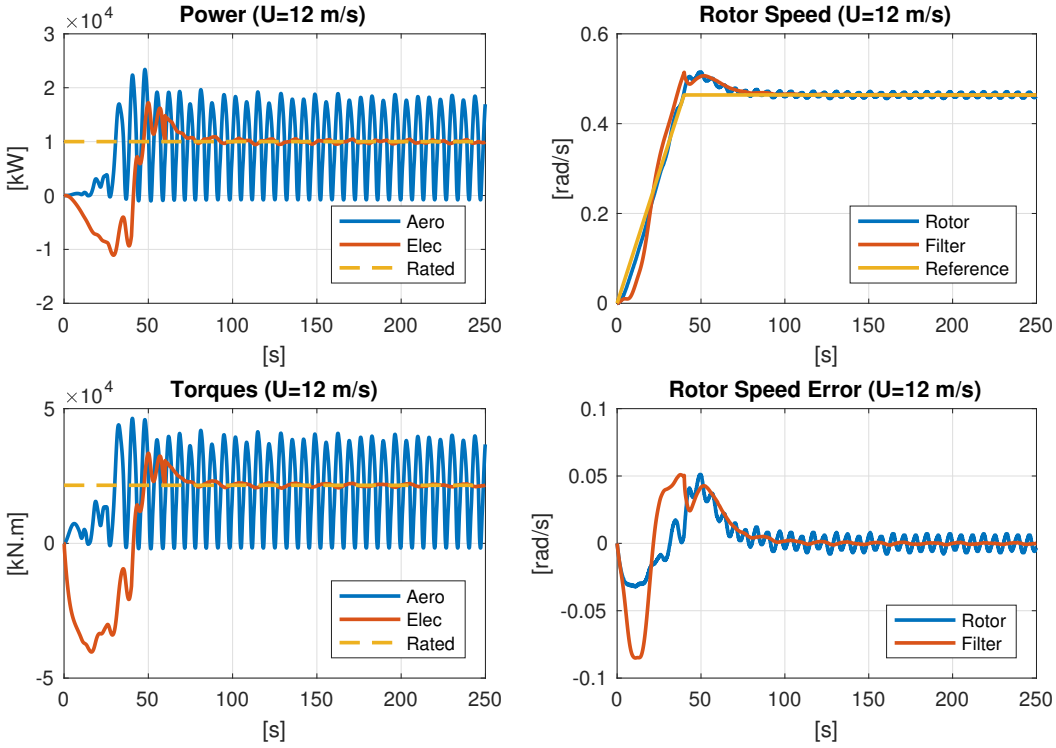

Figure 3.17: Time series of the 10 MW FVAWT at constant rated speed

Power Curves: Wind Only and Wind & Waves

Fig. 3.18 and Fig. 3.19 present the mean and STD values of the key variables (*generator power, aerodynamic power, generator torque, aerodynamic Z torque, filtered rotational speed, rotational speed, aerodynamic thrust, aerodynamic Y torque*) of the 10 MW FVAWT under constant wind and wind & waves conditions, compared with the land-based 10 MW VAWT results.

The mean generator and aerodynamic powers follow exactly the same pattern, as they increase below rated wind speed and are kept constant at 10 MW above rated wind speed. Moreover, the generator mean power is larger than the reference power curve [6] under rated, and the generator power STDs seem way smaller than the reference values as well. Moreover, no obvious comment can be made on the effect of the various environmental conditions based on the generator power results and the aerodynamic power results.

However the standard deviation of the generator torque seems to be higher for the wind & waves case than for the wind only case, which is itself smaller than for the land-based case. The mean and STD values of the various cases are similar for the aerodynamic Z torque.

In Fig. 3.19, the mean filtered rotor speed and the mean rotor speed appear to take same values, while the STD of the rotor speed takes larger values than for the filtered rotor speed (approximately 8 10^{-3} rad/s against 1.5 10^{-3} rad/s, comparing the y-axis). The mean and STD values of the aerodynamic thrust seem to be the same in all three environmental conditions. The mean aerodynamic Y torque takes smaller values than the mean aerodynamic Z torque (approximately 2 10^{3} kN.m against 3 10^{4} kN.m, comparing the y-axis scales).

Additionally, the spectral analysis of the 10 MW FVAWT is available in the appendix, and the same trends were observed as for the 5 MW FVAWT.

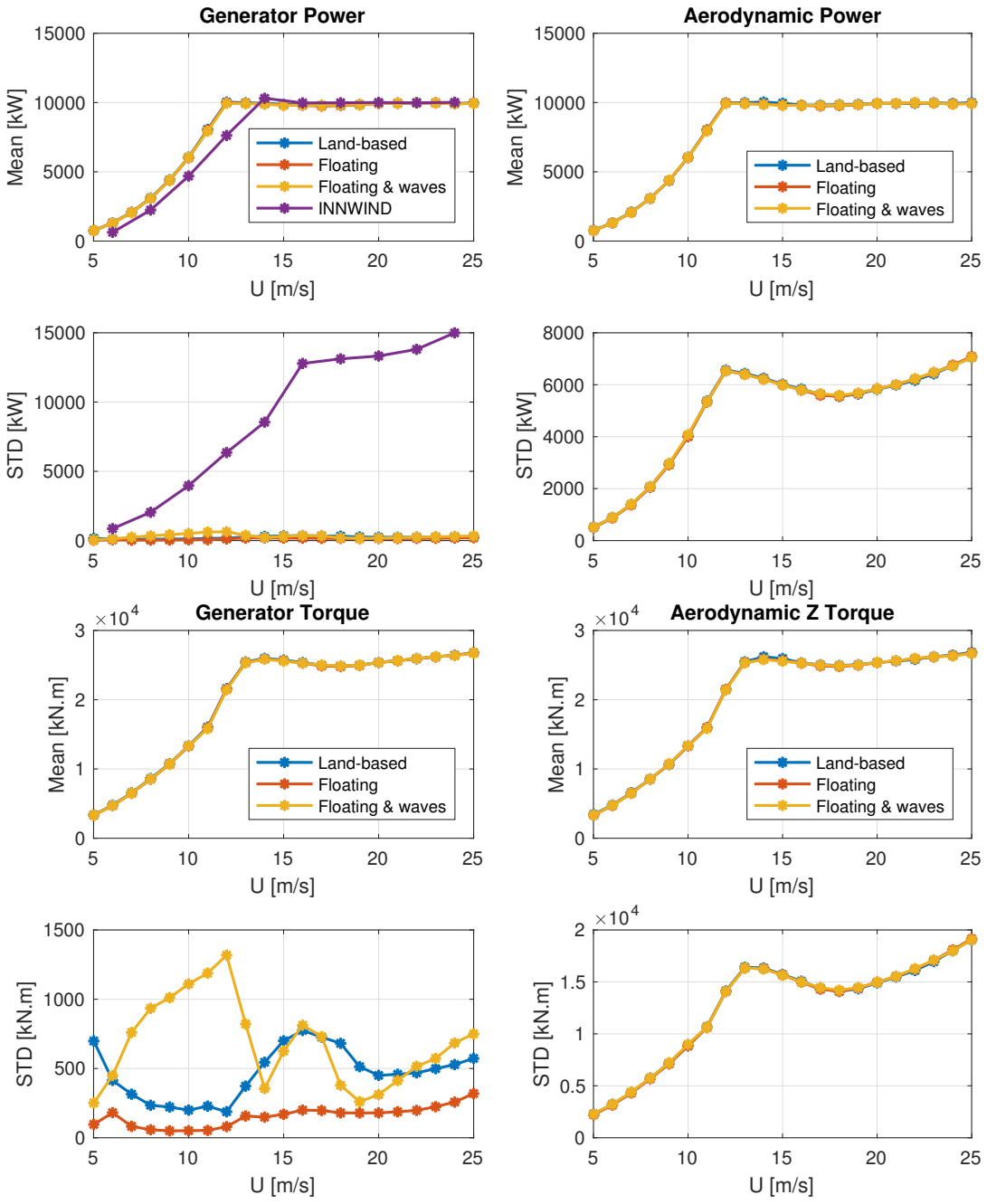

Figure 3.18: Mean and standard deviation of the 10 MW FVAWT dynamic variables (generator power, generator torque, aerodynamic power, aerodynamic Z-axis torque), under constant wind and wind & waves conditions (comparison with land-based results and [6])

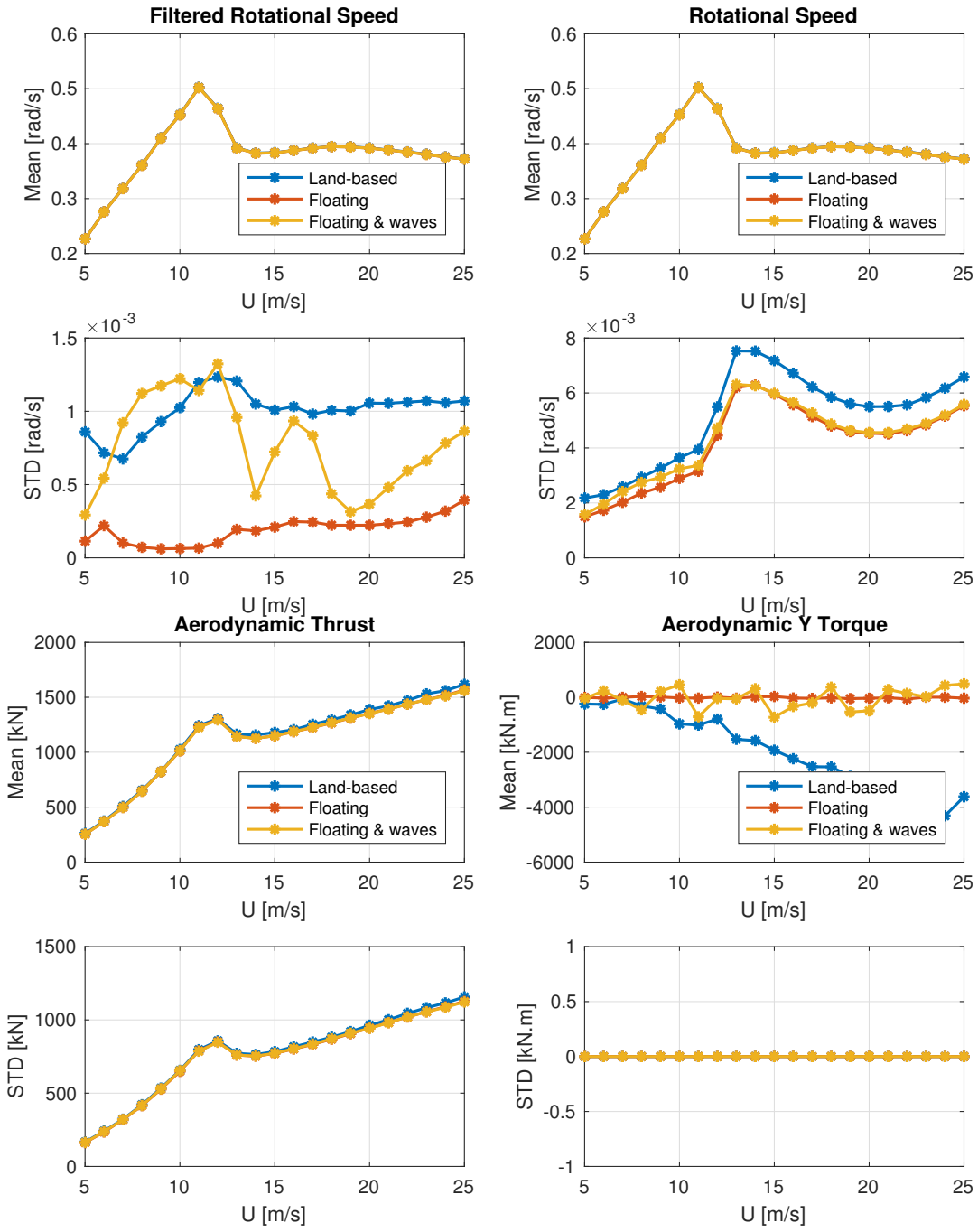

Figure 3.19: Mean and standard deviation of the 10 MW FVAWT dynamic variables (filtered rotational speed, rotational speer, aerodynamic thrust, aerodyanmics Y-axis torque), under constant wind and wind & waves conditions (land-based results are also included for comparison purposes)

Chapter 4: Discussion

This chapter interprets the results presented in the previous chapter, in the light of the literature review and the methods chapter. The performances of the optimized solutions implemented are evaluated (*control, spar design, upscaling*). Some limitations of the results are also pointed out, while some design improvements of the existing models are suggested.

4.1 Control Strategy Efficiency

4.1.1 Performances at Rated Speed

As a general comment, the new version of SIMO seems to work effectively, for both the land-based and the floating 5 & 10 MW VAWTs. Indeed, when comparing the time series of the aerodynamic and generator powers and torques at the rated wind speeds before (Fig. 1.12) and after debugging of SIMO (Fig. 3.1 (a) & (b), Fig. 3.7 & Fig. 3.17), the control system of the new version of the software shows convergence of the electrical signals towards their rated values, as expected from the literature review ([19], [22]).

Table 4.1 presents the mean and STD values of the generator power at the new rated wind speed (12 m/s), for the 5 & 10 MW FVAWTs from the present SIMO investigation and from the literature review for comparison purposes ([7], [6]). The mean generator power is increased with the optimized control strategy by 35% for the 5 MW case, and by 32% for the 10 MW case. This should consequently increase the annual power outputs of the 5 & 10 MW FVAWTs. Moreover, the ratio STD on mean power was kept under 2% for both the 5 & 10 MW cases, which is a drastic decrease compare with 11.8% for the 5 MW reference model and 83.4 % for the 10 MW reference model.

As a result, the electrical power outputs of the FVAWTs should be more stable with the optimized control strategy, as they showed smaller fluctuations around their mean values at a given wind speed (see Fig. 3.8 and Fig. 3.18). Overall the optimized control system delivers a more efficient and a more stable electrical power output, compared with the reference results.

Category	5 MW FVAWT	10 MW FVAWT
Reference Mean Power	3.7 MW	7.6 MW
Optimized Mean Power	5 MW	10 MW
Mean Power Increase	35 %	32 %
Reference Ratio STD/Mean Power	11.8 %	83.4 %
Optimized Ratio STD/Mean Power	1.4 %	1.7 %

Table 4.1: Comparison of the power output with [7], [6] for the 5 & 10 MW FVAWTs, under constant rated wind speed condition ($U_r = 12$ m/s)

4.1.2 Influence of the Control Approach

The mean power increases observed in Table 4.1 at the new rated speed for the optimized FVAWTs can be explained by the control system modifications. Indeed a different reference rotor speed mapping was used in SIMO than for the 5 MW reference case [7], as seen in Fig. 3.2 where the mean rotor speed is significantly changed at the new rated wind speed (reflecting the reference values from Table 2.1 for the 5 MW case), leading to more optimal TSR and power coefficients at 12 m/s. Moreover, the optimized mean power curves are similar for the land-based and floating 5 MW cases (Fig. 3.2 and Fig. 3.8), and take the same values as the optimal aerodynamic power curve (Fig. 2.4, *stand-alone DMS study*) below rated wind speed, as expected.

The differences of generator power STDs observed in Table 4.1 between the SIMO results and the published results can be commented based on the different control approaches used. For the 5 MW Wang & Cheng results [7], a look-up table (U,ω_{ref}) was used along with a PID controller, and the filtered rotational speed was obtained using a 2P notch filter and a low pass filter. However for the 10 MW INNWIND project [6], a look-up table (U,$\mathcal{P}_e$) was preferred, using the generator power instead of the rotor speed. The control system implemented was a PI controller using the electrical power error $\Delta\mathcal{P}_e = \mathcal{P}_e - \mathcal{P}_r$ instead of the rotor speed error $\Delta\omega$. Some difficulties were encountered with filtering of the electrical power signal, which probably explains a very high ratio STD on mean power (83.4 %).

Based on the present results (Table 4.1), using a 2P notch filter and a 4P notch filter seems to be an efficient solution to keep the generator power STD low. It can be verified in Fig. 3.3 that the spectral contents of the filtered rotor speed ω_f and the electrical torque T are very poor in 2P and 4P frequencies. These observations are correlated, as the electrical power is computed from the filtered rotor speed error using a PI control law, and as the reference rotor speed is constant under constant wind conditions. As the generator power is defined as $\mathcal{P}_e = T\omega$, the generator power STD is quite low as well. Indeed the generator torque mean oscillations are canceled out by filtering of the rotor speed. Moreover, the 2P and 4P oscillations of the rotor speed signal are caused by the Z aerodynamic torque, which is shown in the spectral analysis (Fig. 3.3) and is also suggested by the stand-alone aerodynamic results (Fig. 2.6).

However, Fig. 3.8 shows a higher generator power STD for the 5 MW FVAWT case under wind & wave conditions, which was not reported in Table 1.1 (as only constant wind results where compared). This might be due to a yaw coupling effect, as Fig. 3.10 reports a new peak frequency on the generator power and filtered rotor speed spectra. More tests could be made to investigate this effect, and another notch filter could be added to the control system in order to filter out this frequency component. Additionally, it is not guarantied that the present control system would have the same performances under turbulent wind conditions than under constant wind conditions. In order to anticipate the effect of the wind fluctuations on the mean aerodynamic torque, the control system could be ugraded using a new mapping (U, ω_{ref}, T_ref), adding a reference electrical torque $T_{ref} = -\bar{Q}$, evaluated from the stand-alone mean aerodynamic results. The control law could consequently be updated using the following formula:

$$T = T_{ref} - K_P \Delta\omega - K_I \int_0^t \Delta\omega dt \tag{4.1}$$

4.2 Spar Design and Upscaling

4.2.1 Spar Design Review

Table 4.2 summarizes the geometry parameters (*draft, diameter, thickness*) of (i) the optimized FVAWTs implemented in SIMO and (ii) the reference models DeepWind [5] and INNWIND [6]. In particular the drafts were decreased from 110 m to 50 m for the 5 MW FVAWT, and from 184 m from 90 m for the 10 MW, while the main diameters were almost doubled. This gives the opportunity to install a 5 MW FVAWT in intermediate water depths, and a 10 MW FVAWT in wider sea areas than for the INNWIND design. Indeed, the draft of any floating structure is limited by the depth of its installation location, as the bottom of the sea should not be touched by the floating structure, which is a physical constraint to be taken into account in offshore floating design. Moreover, the 50 m draft dimension can be considered as a lower limit for spar optimization, as it approximately corresponds to the maximal depth where a bottom-fixed wind turbine can be installed [9].

Additionally, different approaches were used to choose the spar dimensions in the literature and in this thesis. In the INNWIND project [6], the 10 MW spar was designed based on the 5 MW DeepWind concept, mainly by increasing the draft while the main diameter was hardly increased in comparison. The 5 MW DeepWind [5] optimized spar dimensions were obtained after an optimization algorithm was run over many design variables (>10), with respect to a set of constraints. In particular the lower CG property of VAWTs was exploited by placing the generator at the bottom of the spar, using it as a ballast stabilizing element. The spar optimization method chosen in this study was inspired by the DeepWind optimization approach, except that only two variables were used for optimization (draft and main diameter). Some other simplifications were made, which limits the precision of the results. However it can be seen in Fig. 2.8 that the platform mass increases as the draft decreases and the corresponding optimal diameter increases, which also increases the platform cost. Consequently, there is a trade-off to be found between draft minimization and cost minimization.

Furthermore, some other design solutions could be selected from the stability domains (Fig. 2.9 and Fig. 2.10).

A few comments can be made regarding the hypothesis made for the spar design. For instance it can be checked if the rule-of-thumb formula $M_{steel} = 0.13 M_{dis}$ that was used is realistic or not. Approximating the spar as an empty steel cylinder, its equivalent thickness can be approximated as:

$$\delta = \frac{M_s}{\rho_s d \pi D} \tag{4.2}$$

This formula gives 4 cm for the 5MW spar, and 7 cm for the 10 MW spar, which are both close to the 5 MW DeepWind value (5 cm) and the 10 MW INNWIND Value (7.5 cm), as summarized in Table 4.2. Therefore the steel mass rule of thumb used to design the spar is acceptable. Moreover, the generator could be placed more close to the sea level for easier access for 0&M, but this would probably require more ballast.

Category	Power	5 MW	10 MW
Optimized Models	Concept	5MW FVAWT	10 MW FVAWT
	Draft [m]	50	90
	Diameter [m]	15.7	20
	Thickness [cm]	4	7
Reference Models	Concept	DeepWind	INNWIND
	Draft [m]	110	184
	Diameter [m]	8.2	10.1
	Thickness [cm]	5	7.5

Table 4.2: Comparison of the geometry parameters for the optimized 5 & 10 MW FVAWTs and the reference models [5], [6]

4.2.2 Upscaling from 5 to 10 MW

Upscaling from 5 to 10 MW of a spar-floating VAWT was conducted in this study. Overall no significant issue was observed in the 10 MW results, or at least not in comparison with the 5 MW results. In particular, the stability issues from the INNWIND project [6] observed when upscaling the DeepWind concept from 5 to 10 MW were not encountered in this study. The draft was decreased from 184 m to 90 m, while the ratio STD on mean electrical power was decreased from 83.4 % to 1.7 %. In regard of these figures, the upscaled control system and the 10 MW optimized spar showed satisfying results. From a technical point of view, FVAWTs seem like a viable option for upcaling and deep water deployment.

Similarly as in the INNWIND project [6], geometrical upscaling was used to increase the rotor dimensions, doubling the mean rated power. Moreover dimensional upscaling was used to upscale the control system from SIMO, whereas in the INNWIND project a different control system was designed (leading to an unstable generator power output). In the INNWIND project a combination of Froude scaling and trial-and-error approach was implemented to

design a 10 MW spar, elongating the spar and adjusting the ballast. In this study, a spar design and optimization algorithm was implemented for the 5 & 10 MW FVAWTs with respect of a set of stability conditions, as suggested by [5] for the 5 MW DeepWind optimization. Both the draft and the main diameter of the spar were used as optimization variables, and attention was given to eigenfrequency placement in order to avoid overlapping with excitation frequencies (*2P, 4P, wave*). Overall the SIMO implementation of both 5 & 10 MW FVAWTs helped verify that the optimization methods gave effective results.

As a remark, if geometrical upscaling had been used to upscale the optimized spar from 5 to 10 MW, the resulting spar would not have been stable from a hydrodynamic point of view. Indeed, by scaling the 5 MW optimized spar by $\sqrt{2}$, the scaled draft would be 70.7 m and the scaled diameter would be 22.2 m. According to Fig. 2.10, which depicts the stability domain of the 10 MW FVAWT, the conditions C2 and C3 would not be verified, which means that the upscaled FVAWT would not be dynamically stable.

Moreover the optimized 10 MW spar dimensions are still considerably large, even if the draft has been drastically reduced compared with INNWIND. Consequently, it could be interesting to investigate other floating options, and compare the global construction costs. For instance, semi-submersibles or TLPs could be used as platforms to support the 10 MW VAWT used in this study, and the mass of steel necessary to ensure hydrodynamic stability could be compared for the different spar types.

4.3 Spar Stability & Gyroscopic Effect

4.3.1 Spar Stability

Overall dynamic stability was observed for the 5 & 10 MW FVAWTs through the various simulations that were conducted in SIMO. To begin with, some decay tests were run in surge, heave, pitch and yaw, and the FVAWTs responded with damped oscillations around their equilibrium position at frequencies very close to the designed eigenfrequencies, with error less than 1 % in heave, pitch and yaw. However the error in surge was 9% (11%) for the 5 MW (10 MW) case, which is probably due to a surge-pitch coupling. This can be verified as both surge spectra (Fig. 3.6 and Fig. 3.16) showed a peak at the pitch eigenfrequency.

The FVAWTs were also tested in harsch environmental conditions, as correlated sea states and constant wind conditions were implemented, with wave heights up to 10 m and wind speeds up to 25 m/s. While the spectral analysis of the regular wave tests showed frequency peaks at the natural frequencies of the floating structures, some new peaks were identified in wind only and wind & waves conditions (interpretation in the next section). The mean and STD values in surge, heave and pitch were remarkably low, with some pitch angle STD values smaller than 1 degree and some mean pitch angle values smaller than 0.01 degree. These values seem very small and probably deserve some more investigation, in particular regarding the pitch angle extreme values instead of STD. Furthermore it appears that the mean pitch angle of a FVAWT is much smaller than for a FHAWT, probably because of the

vertical rotational motion inertia. Consequently, the design requirements of this study could probably be alleviated concerning the maximal pitch angle.

The stability of the FVAWT yaw motion is important for the stability of the power production. Indeed, electrical power is generated thanks to the hub rotation around its Z axis, and the platform yaw motion must be minimized. This was verified thanks to the yaw damping system, which worked efficiently as the yaw STD was kept below 2 degrees for the wind only tests (see Fig. 3.12, 5 MW FVAWT). However the yaw STD reached 7 degrees for the wind & wave tests, also increasing the generator power STD in that case (see Fig. 3.8, 5 MW FVAWT). The yaw damping system enables the generator power to be almost as stable in the wind-only case as in the land-based case, although the control system was initially designed for a land-based VAWT. Moreover the yaw mean value reached 40 degrees in the 5 MW case and showed the same variations with the wind speed as the mean Z aerodynamic torque, which is understandable as a linear yaw stiffness was implemented in SIMO.

4.3.2 Gyroscopic Effect

Some circular plane trajectories of the 5 MW FVAWT hub were observed under constant wind conditions (see Fig. 3.14). This pattern is quite singular and very clearly identified for the wind only case, however it is not visible for the wind & wave and wave only trajectories. Moreover, the period of this circular motion can be identified using the spectral analysis. Indeed, an unknown peak was observed in Fig. 3.13 for the wind only and wind & wave cases, which probably corresponds to this circular frequency. Moreover, the new peak frequency is modified by the presence of waves, and disappears without wind, which means that it depends on the rotation of the rotor.

Similar observations were reported by some Japanese researchers working on FVAWTs, and identified as *gyroscopic effect* [17]. In particular, this effect is known to increase the stability of the FVAWT, which allows to design smaller platforms. As shown in Fig. 4.1, the axis of a rotating FVAWT was also found to follow a circular trajectory in the published results. This phenomenon is simlilar to the prcession of a rotating body studied in mechanics [31]. As the body is spinning, it generates an angular momentum that can be hardly deflected by a perturbation torque, as inertial effects help stabilizing the body. This could explain why the pitch mean and STD values reported in the SIMO investigations were surprisingly small compared with FHAWT values.

Taking advantage of the stabilizing gyroscopic effect for FVAWTs, it should be possible to design smaller spars for the 5 & 10 MW VAWTs studied in this thesis. Indeed, the maximum pitch angle requirement that was implemented in MATLAB was based on the maximum aerodynamic thrust and the linear stiffness values only. In future research, the rotor rotational speed could also be taken into account to estimate the maximum pitch angle, including the gyroscopic effect in the spar design theory. The spar stability domains could therefore occupy larger areas of the (spar, diameter) plane (previously represented in Fig. 2.9).

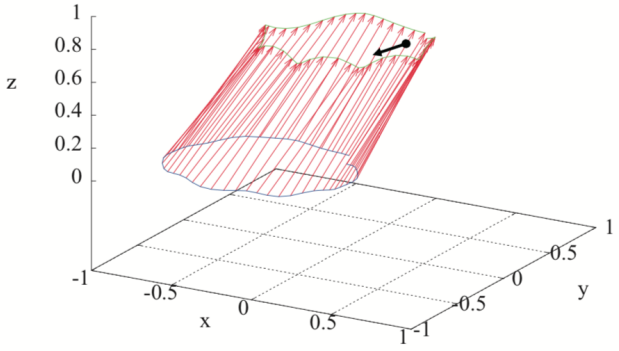

Figure 4.1: Axis trajectory of a 3 MW FVAWT (wind & wave conditions, $U = 15$ m/s) [17]

Chapter 5: Conclusions and recommendations

In this thesis, a few potential advantages of VAWT compared with HAWT were investigated, namely for upscaling and deep water, using an engineering approach. Two floating prototypes were designed and tested based on the 5 MW DeepWind concept, a 5 MW FVAWT and a 10 MW upscaled version. The main challenges encountered were (i) the VAWT module code debugging in SIMO and (ii) the upscaling issues reported in the literature. Indeed, while upscaling of HAWT has been studied thouroughly, the few published results concerning upscaling of VAWT reported significant issues, in particular showing very large spars and unstable control systems [6]. The following sections present the main steps of the present work (design, analysis, outcomes, contributions), and suggestions for future research (limitations, recommendations).

5.1 FVAWT Design

In order to design an efficient and stable 10 MW FVAWT, the 5 MW land-based VAWT first had to be studied in SIMO, before being upscaled and mounted on a spar. As some incoherent preliminary results were observed, the SIMO VAWT source code was investigated and a debugged version of SIMO was written. An aerodynamic study was then conducted on the land-based 5MW VAWT. In particular, the power diagrams were obtained by running stand-alone tests, and the optimal TSR and power coefficients were identified. The control system was then optimized to operate with optimal aerodynamic conditions under rated wind speed. To that end, the rated wind speed was lowered from 14 to 12 m/s, and the reference rotor speed mapping was optimized below rated wind speed. Furthermore the PI controller was tuned at rated speed, and a 4P notch filter was added to the control system, in order to avoid an amplification of the 4P periodical rotor speed component by the PI controller.

Once the 5 MW VAWT was optimized, a spar platform was designed to support it with respect to stability constraints, forming a 5 MW FVAWT. An optimization algorithm was implemented in MATLAB, leading to the identification of stability domains in the draft-diameter plane. A design solution was chosen with a rather small draft (50m for the 5MW VAWT, compared with 110m for DeepWind [5]), which was made possible by placing the generator at the bottom of the spar and by increasing the spar diameter. Finally, a 10 MW FVAWT was designed in three steps: (i) geometrical upscaling of the 5 MW FVAWT

to double its swept surface, leading to a 10 MW VAWT (ii) dimensional upscaling of the optimized 5 MW control system, including the PI gains and (iii) design of a new spar to support the 10 MW VAWT, using the same MATLAB algorithm as for the 5 MW VAWT.

5.2 FVAWT Analysis

The next step was to analyze the designed 5 & 10 MW FVAWTs models, by testing them in operational conditions. For that purpose, some time-domain simulations were ran with SIMA under various environmental conditions. First, the 5 & 10 MW land-based VAWTs were tested under constant wind, and the control system worked well for wind speeds within the wind speed boundaries of the study (from 5 to 25 m/s). Indeed by comparing the 5 MW results with [7], a higher mean power was obtained under rated speed, along with a smaller standard deviation of the generator power. Secondly, the 5 & 10 MW FVAWTs were implemented in SIMA, and the designed spars were modeled as slender rigid bodies. A preliminary dynamic analysis was conducted using decay tests and irregular wave tests, leading to the identification of the rigid body motion eigenperiods, matching precisely with the design values. Additionally, some constant wind tests and wind - wave tests were run, using a correlated environmental condition set. For the 10 MW case, the standard deviation of the generator power was ten times smaller than the published results [6]. Furthermore for both 5 & 10 MW cases, the time-domain and spectral analysis of the DOF motions showed overall dynamic stability. The yaw oscillations due to the 2P varying aerodynamic loads were efficiently damped by a reasonably low quadratic yaw damping coefficient. Moreover, the presence of a gyroscopic effect was identified in wind conditions by plotting the hub plane trajectories. Spectral analysis showed that the presence of waves modifies the gyroscopic frequency, without overlapping with surge and pitch eigenfrequencies.

5.3 Main Outcomes

To summarize, several original solutions were implemented in this master thesis, using SIMO and MATLAB for the design and optimization part, and SIMA for the numerical integrated analysis. This lead to some encouraging results for research on VAWTs, detailed as follows:

1. *SIMO debugging:* some mistakes were found in the SIMO source code and corrected, and a new version of the SIMO VAWT module was compiled for present and future use. The updated version of SIMO seemed to work well compared with published results, both from the aerodynamic and control points of view. Moreover, a 4P notch filter was added into the control part of the code, which helped reduce the standard deviation of the power output for the 5 MW land-based and floating VAWTs.

2. *Power output optimization:* a more efficient and stable power output was obtained, thanks to an optimized control strategy. Indeed, the rated speed was decreased from 14 to 12 m/s, which increased the mean generator power by 35% (32%) for the 5 MW (10 MW) FVAWT at the new rated speed (compared with [7],[6]). As a result, the annual production should also increase with the new control strategy. Moreover, the

standard deviations of the generator power and the generator torque were significantly decreased, ensuring a more stable power output under constant wind, and possibly less wear of the mechanical parts.

3. *Spar design and optimization:* small and stable spars were designed to support the 5 & 10 MW VAWTs. A simplified spar optimization algorithm was implemented with MATLAB, resulting in a draft decrease from 110m to 50m and a diameter increase from 8.2m to 15.7m for the 5MW DeepWind [5]. Similarly, the spar draft was decreased from 184m for INNWIND [6] to 90m for the 10 MW FVAWT, and the corresponding diameter was increased from 10.1m to 20m. This validates the advantage of VAWTs compared to HAWTs when it comes to spar design, as smaller drafts give access to a wider choice of installations areas, including intermediate water depths. Moreover, a stabilizing gyroscopic effect was observed, which is also an advantage for FVAWTs.

4. *Upscaling from 5 to 10 MW:* a 10 MW FVAWT was designed and tested successfully, showing that VAWTs have a high potential for upscaling. The issues encountered by [6] were solved by (i) studying and optimizing the 5 MW DeepWind VAWT, (ii) upscaling the rotor and the control system using dimensional analysis, (iii) designing a new spar for the 10 MW VAWT. The resulting 10 MW FVAWT showed good power output and dynamic stability, like the 5 MW FVAWT model. As VAWTs simply have one control input, the control system upscaling is quite straightforward, and it should not be a problem to upscale to 20 MW using the same approach.

5.4 Limitations

The presented results were obtained under certain assumptions and conditions, which limits the impact of this study. Not only was the scope of the study quite narrow, but also several simplifications were made along the way, which could be discussed and improved in the future. For instance, not all types of VAWTs and floaters were studied, as only a Darrieus rotor was used mounted on a spar buoy. Moreover, only two blades were used for the whole study, and the influence of the number of blades on the various outputs was not studied. The focus was on the upscaling to 10 MW, but the methods used should also work for higher rated powers. The PI control law was assumed to be accounted for exactly by the generator torque, neglecting possible imperfections of the electrical system. All bodies were assumed to be rigid, neglecting internal stresses and possible mechanical failures. Furthermore, the physical models used were the DMS theory for the aerodynamics, Morison's equation for the spar-wave hydrodynamic interaction, and linear stiffnesses for the mooring lines. These models are reasonably simple, but do not represent all the physical effects that may perturb the FVAWTs in real conditions. Additionally, the environmental test conditions implemented in the SIMA analysis were also limited, as only constant wind tests and one-direction wave spectras were used. Altough these tests gave encouraging results, further research could be conducted using less idealized environmental conditions.

5.5 Recommendations for Future Work

Some suggestions for further work are presented here, as possible solutions to the work limitations. Further research on VAWTs could be based on this thesis, in three main directions: (i) more detailed analysis of the current models, (ii) extension of the investigation in the design area, or (iii) refinements of the physical models used in the analysis.

Analysis of Existing Models

- *Annual power output*: the annual power production of the 5 & 10 MW VAWTs could be computed by using mean wind speed statistical distributions. Shutdowns should also be introduced for wind speeds above 25 m/s.

- *Turbulent wind*: the robustness of the control system could be tested under turbulent wind conditions, by comparing the standard deviation of the power output with constant wind results. Some more extreme environmental conditions could also be included.

- *Number of blades*: by increasing the number of blades to three in SIMA, one could probably find some advantages ([24]), such as smaller aerodynamic torque oscillations, and easier start-up phase.

Extension of the Present Investigation

- *Laboratory tests*: In order to validate the numerical investigations of this thesis, some laboratory tests could be carried out. For instance, hybrid-testing of reduced scale models could help identify the main dynamic differences between HAWTs and VAWTs found in this study, such as gyroscopic effect.

- *Upscaling and downscaling*: the possibility of upscaling a FVAWT from 10 MW to 20 MW could be studied using the same methods as in this thesis, although structural strength and available generators might be challenges. Furthermore, downscaling is a topic that is based on the same dimensionless conservation principles as upscaling, and which can be relevant for some laboratory tests.

- *Spar design and optimization*: the VAWT spar optimization algorithm developed in this thesis could be upgraded by including the gyroscopic effect, which could lead to some more optimal spar designs. Moreover, a similar spar optimization method could be adapted for HAWTs, in particular for upscaling purposes.

- *Control system*: some other control and filtering strategies could be tested and compared in various environmental conditions. For instance, non-linear control theory could be used and a new mapping could be implemented (mean wind speed, mean desired torque).

- *Floating platform*: VAWTs could be installed on other floaters than spars, such as semi-submersibles or tension-leg-platforms ([22]). Further studies could compare stability

and upscaling challenges for a selected choice of floaters, or even for a bottom-fixed VAWT.

- *Offshore operations*: a study of feasibility could be led for the installation of a 5 or 10 MW FVAWT, and to illustrate and anticipate the industry challenges in the operations and maintenance area (crane lifting, assembly, blade transport, repairs).

Modeling Refinements

- *Structural analysis*: the VAWT blades, tower and mooring lines could be modeled as flexible elements in SIMO-RIFLEX, for long-term fatigue damage analysis purposes. In particular, if fatigue damage happens to be a significant issue for FVAWTs ([7]), various design strategies could be implemented and compared in order to investigate and minimize this effect (control system, floater design, number of blades).

- *Aerodynamics*: another VAWT aerodynamic theory called the actuator cylinder (AC) method [23] could be implemented in SIMO for comparison with the DMS. On a more advanced level, turbulent effects and wake interactions could be studied too, as they may be relevant for VAWTs in farm configuration. In particular, it could be investigated if VAWTs are more efficient than HAWTs when installed in wind farms ([24]).

- *Hydrodynamics*: some more advanced hydrodynamics studies could be carried out, accounting for potential theory, diffraction, nonlinear wave-structure interactions, and nonlinear buoyancy. Such investigations could validate the dynamic stability of the designed structures, or on the contrary impose some new conditions for the spar design.

Bibliography

[1] Equinor, Hywind *https://www.equinor.com/en/what-we-do/hywind-where-the-wind-takes-us.html*, 2018

[2] I. Pineda *Offshore Wind in Europe: Key trends and statistics 2017*. Wind Europe, 2018

[3] J. Paquette, M. Barone *Innovative offshore vertical-axis wind turbine rotor project*. EWEA 2012, The European Wind Energy Association, Copenhagen, Denmark, 2012.

[4] L. Vita *Offshore Vertical Axis Wind Turbine with Floating and Rotating Foundation*. Doctoral Theses at DTU, 2011

[5] P.A. Berthelsen, L. Vita, I. Fylling, U. Paulsen *Conceptual Design of a Floating Support and Mooring System for a Vertical Axis Wind Turbine*. Proceedings of the ASME 2012 International Conference on Ocean, Offshore and Arctic Engineering, 2012

[6] J. Azcona and all *Design Solutions for 10MW Floating Offshore Wind Turbines*. INNWIND Report, 2017

[7] Z. Cheng, K. Wang, Z. Gao, T. Moan *A comparative study on dynamic responses of spar-type floating horizontal and vertical axis wind turbines*. Wind Energy, 2017

[8] A. Colmenar-Santos, J. Perera-Perez, D. Borge-Diez, C. dePalacio-Rodriguez *Offshore wind energy: A review of the current status, challenges and future development in Spain*. Renewable and Sustainable Energy Reviews, 2016

[9] D. Kallehave, B. Byrne, C. LeBlanc Thilsted, K. Mikkelsen *Optimization of monopiles for o shore wind turbines*. Philosophical Transactions of the Royal Society A, 2015

[10] E. Bachynski *Design and dynamic analysis of tension leg platform wind turbines*. Doctoral Theses at NTNU, 2014

[11] B. Koppenol, Z. Cheng, Z. Gao, C. Ferreira, T. Moan *A comparison of two fully coupled codes for integrated dynamic analysis of floating vertical axis wind turbines*. 14th Deep Sea Offshore Wind R&D Conference, EERA DeepWind 2017

[12] Fowler, Bull, Goupee *A Comparison of Platform Options for Deep-water Floating Offshore Vertical Axis Wind Turbines: An Initial Study*. Sandia Report, SAND2014-16800, 2014

[13] Equinor, Empire Wind *https://www.equinor.com/en/what-we-do/empirewind.html*, 2018

[14] Z. Cheng, H. Madsen, W. Chai, Z. Gao, T. Moan *A comparison of extreme structural responses and fatigue damage of semi-submersible type floating horizontal and vertical axis wind turbines*. Renewable Energy, 2017

[15] H. Sutherland, D. Berg, T. Ashwill *A Retrospective of VAWT Technology*. Sandia Report, 2012

[16] Z. Cheng, H. Madsen, Z. Gao, T. Moan *A fully coupled method for numerical modeling and dynamic analysis of floating vertical axis wind turbines*. Renewable Energy, 2017

[17] H. Akimoto, K. Tanaka, Y. Hara *Gyroscopic effects on the dynamics of floating axis wind turbine*. Grand Renewable Energy 2014

[18] J. Jonkman *Definition of the Floating System for Phase IV of OC3* NREL Technical Report, 2010

[19] H. Svendsen, K. Merz, A. Endegnanew *Control of floating vertical axis wind turbine.* EWEA Annual Event (Scientific Track), Copenhagen, Denmark, 2012

[20] W. Xue *Design, numerical modelling and analysis of a spar floater supporting the DTU 10MW wind turbine* Master Thesis at NTNU, 2016

[21] M.T. Islam *Design, numerical modelling and analysis of a semi-submersible floater supporting the DTU 10MW wind turbine* Master Thesis at NTNU, 2016

[22] K. Wang *Modelling and dynamic analysis of a semi-submersible floating vertical axis wind turbine*. Doctoral Theses at NTNU, 2015

[23] Z. Cheng *Integrated Dynamic Analysis of Floating Vertical Axis Wind Turbines*. Doctoral Theses at NTNU, 2016

[24] Z. Cheng, H. Madsen, Z. Gao, T. Moan *Effect of the number of blades on the dynamics of floating straight- bladed vertical axis wind turbines*. Renewable Energy, 2016

[25] *Design limits and solutions for very large wind turbines* . UpWind Report, 2011

[26] K. Merz *A Blade Element Momentum Method for Dynamic Analysis of Vertical Axis Wind Turbines - Rev B* NTNU Report, 2011

[27] H. Beri, Y. Yao *Double Multiple Stream Tube Model and Numerical Analysis of Vertical Axis Wind Turbine*. Energy and Power Engineering, 2011

[28] G. Sieros, P. Chaviaropoulos, J.D. Sørensen, B. H. Bulder and P. Jamieson *Upscaling wind turbines: theoretical and practical aspects and their impact on the cost of energy.* Wind Energy, 2012

[29] O.M. Faltinsen *Sea Loads on Ships and Offshore Structures*. Cambridge, 1990

[30] K. Johannessen, T.S. Meling and S. Haver *Joint distribution for wind and waves in the Northern North Sea*. International Journal of Offshore and Polar Engineering, 2002

[31] P. Teodorescu *Mechanical Systems, Classical Models.* Springer, 2002

Appendices

Appendix A: Complementary Results of the 10 MW FVAWT

Some extra results of the 10 MW FVAWT are presented in this appendix, which look very similar to the 5 MW FVAWT results presented in the Chapter 3.

The spectral analysis of the power producion variables is presented in Fig. A.1. The mean values and standard deviations of the various degrees of freedom are presented in Fig. A.2 and Fig. A.3. Finally, the hub trajectories are presented in Fig. A.4, and the spectral analysis of the degrees of freedoms is presented in Fig. A.5.

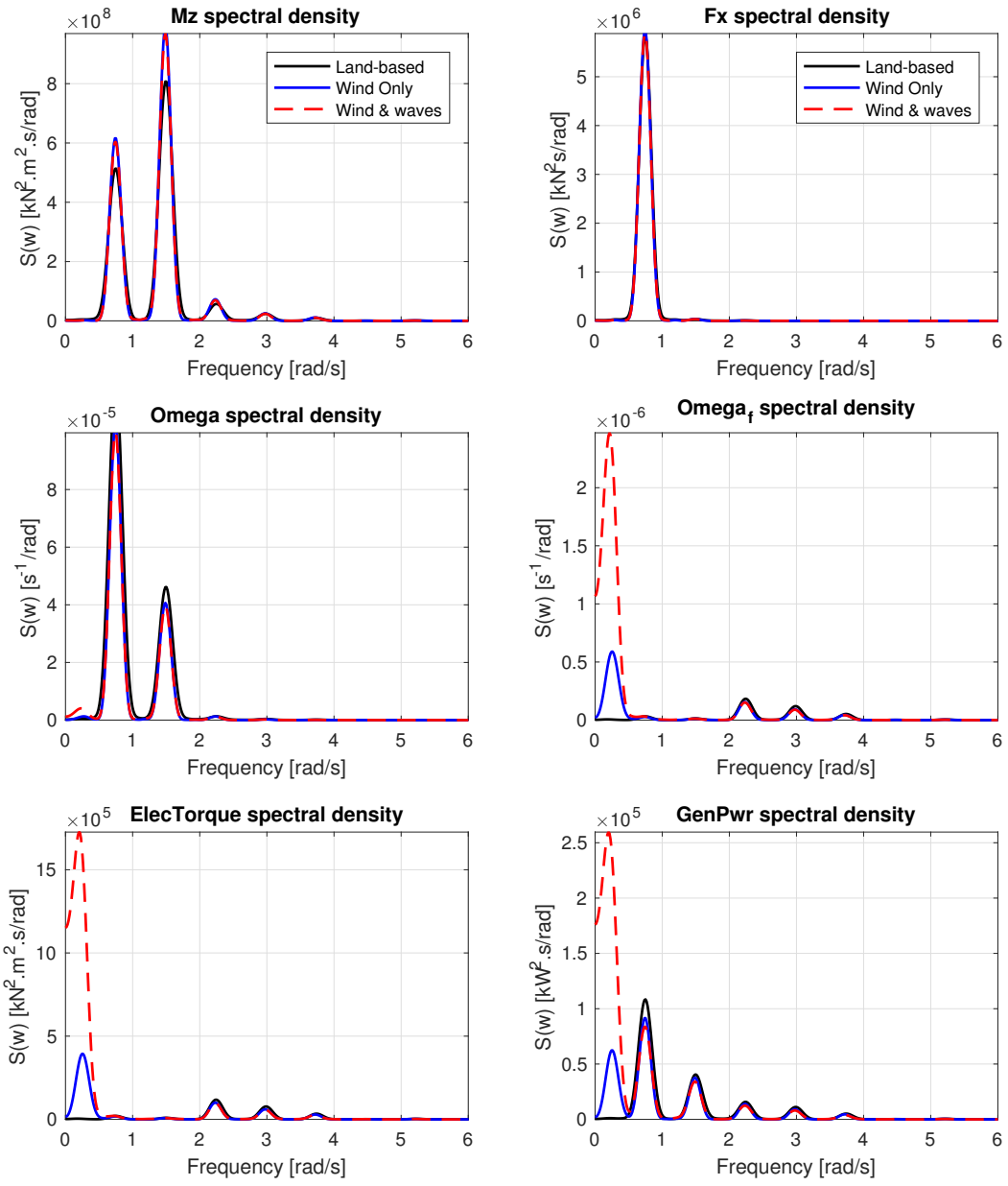

Figure A.1: Spectral analysis of the 10 MW FVAWT production variables under constant wind and wind & waves ($U = 25$ m.s^{-1}, also compared with land-based spectra)

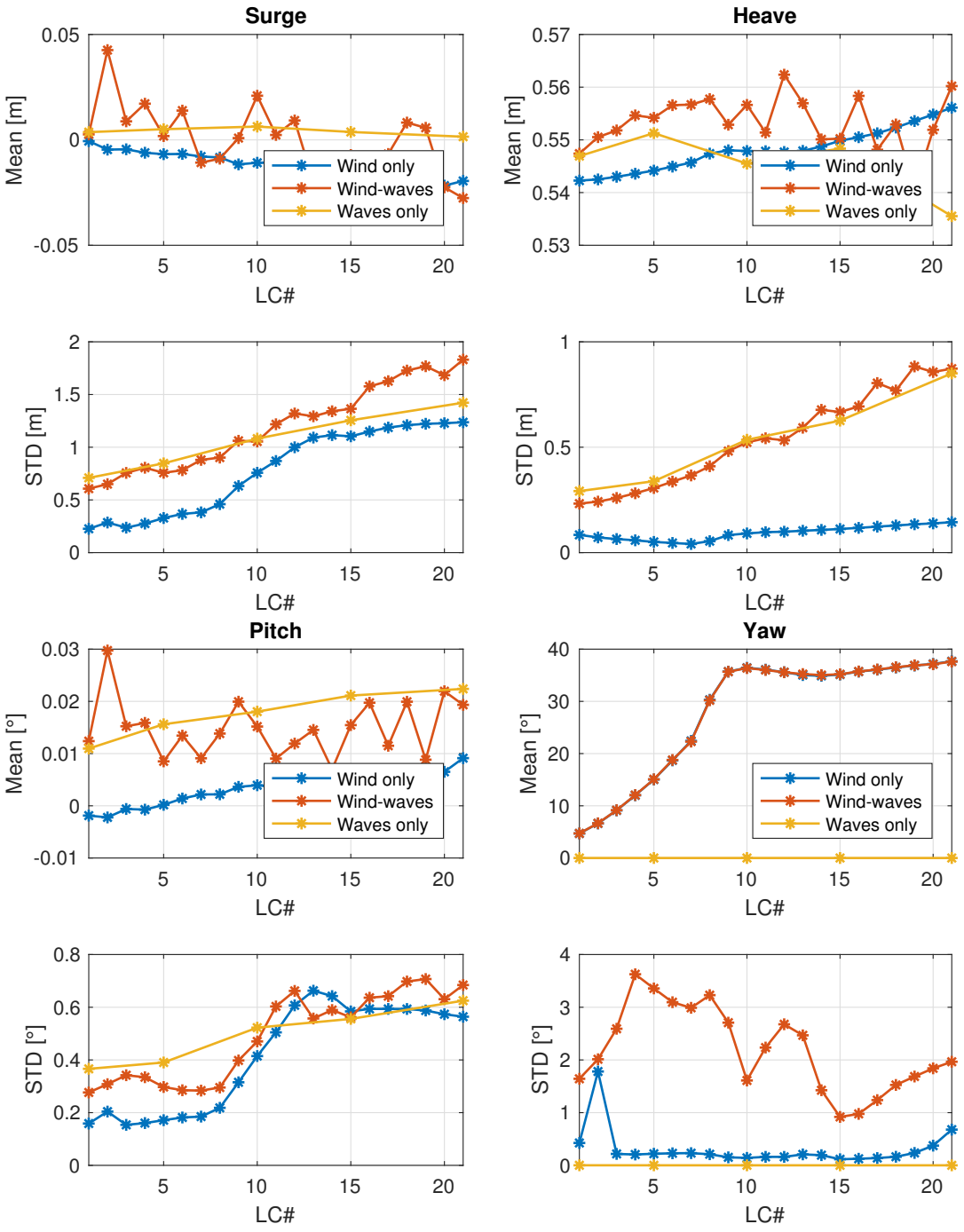

Figure A.2: Mean values and standard deviations of the 10 MW FVAWT DOFs (surge, heave, pitch, yaw)

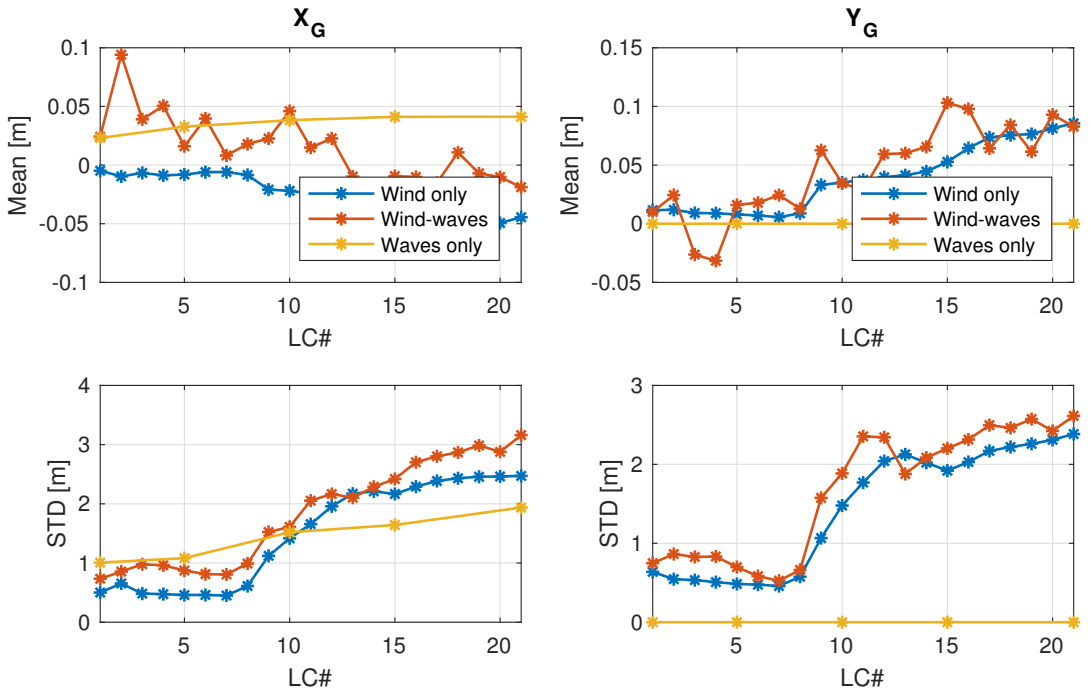

Figure A.3: Mean values and standard deviations of the plane coordinates (X_G, Y_G) of the rotor center of gravity, for the 10 MW FVAWT rotor

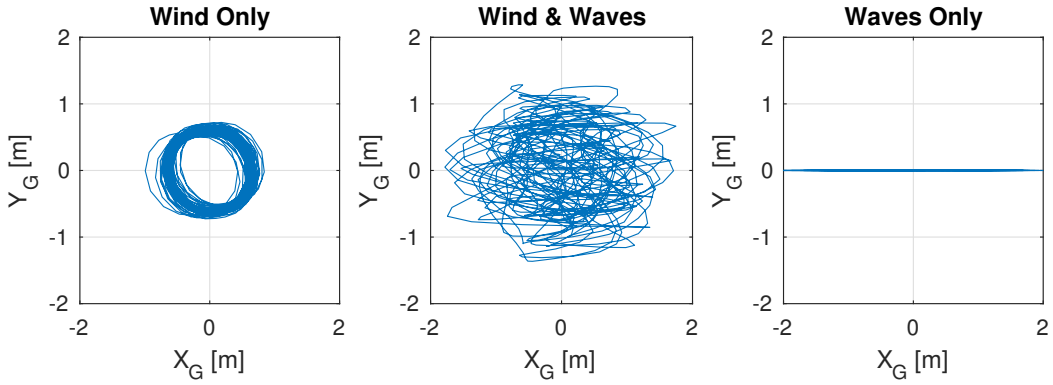

Figure A.4: Hub trajectory in the (X,Y) plane for the 10 MW FVAWT ($U = 8$ m.s^{-1})

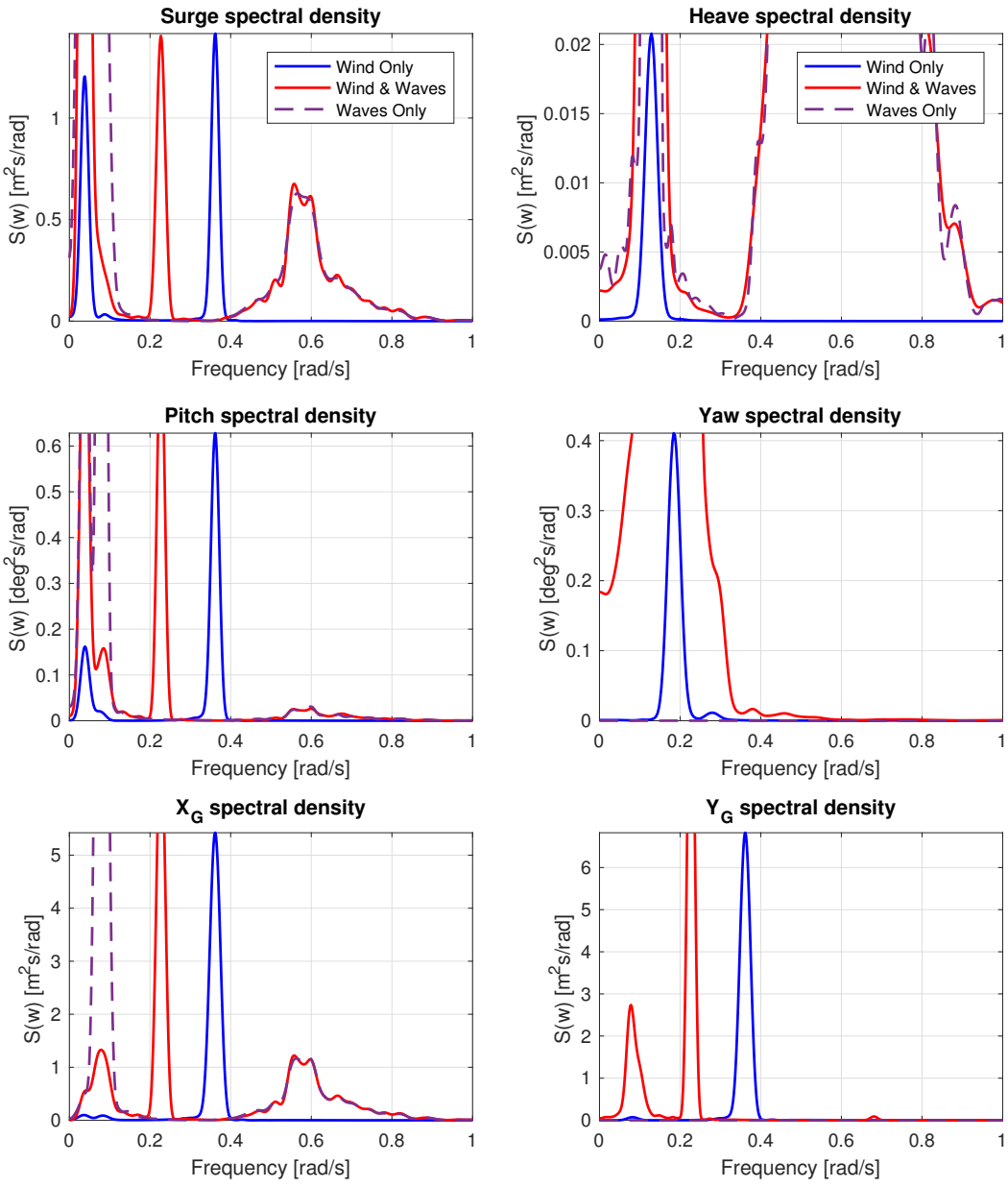

Figure A.5: Spectral analysis of the 10 MW FVAWT DOFs for $U = 8$ m.s^{-1} under constant wind, wind & waves, and waves only